UNIVERSITY OF CALIFORNIA
RIVERSIDE

Advances in Atmospheric Trace Gas Monitoring Systems: Quantification of Methane Sources by Solar Column Observations in the San Joaquin Valley of California and Characterization of a Portable Air Toxics Sensor

A Dissertation submitted in partial satisfaction
of the requirements for the degree of

Doctor of Philosophy

in

Environmental Sciences

by

Isis Frausto-Vicencio

December 2022

Dissertation Committee:
Dr. Francesca Hopkins, Chairperson
Dr. Roya Bahreini
Dr. William Porter

The Dissertation of Isis Frausto-Vicencio is approved:

_____

_____

_____

Committee Chairperson

University of California, Riverside

AKNOWLEDGEMENTS

I would like to first thank my advisor, Francesca Hopkins, for her support and guidance over the past ten years. It has been a fun experience discussing research ideas, simplifying complex projects, and writing papers together. Thank you for believing in my abilities as a scientist and helping me find the confidence in my skills. I would also like to thank the rest of my oral qualifying exam and dissertation committee Roya Bahreini, William Porter and Ying-Hsuan Lin, for their support and advice.

The entire Hopkins group has been supportive, from helping me collect measurements to exploring new places together. My lab mates Valerie Carranza and Talha Rafiq for making the experience of starting graduate school more enjoyable and for joining me in this wild ride from NASA internships and to now becoming doctors. My lab mate Michael for being so encouraging and supportive in data collection for projects. Sajjan Heerah for helping me co-lead five field campaigns and learn all about solar spectroscopy. Alison Marklein for always providing advice from writing to pursuing careers. My undergraduate mentees Alondra Moreno and Michelle Carr who became essential part of carrying out analysis of projects and helping me become a better mentor

I would like to thank all those involved in supporting the technical aspects of this work including Manvendra Dubey, Marc Fischer, Seongeun Jeong, and Ying-Kuang Hsu. The EM27/SUN measurement campaigns in the SJV were a group effort and could have not been done without the help of Sajjan Heerah, Michael Rodriguez, Michelle Carr, Cindy Yanez, Alondra Moreno, Dulce Frausto, Nicole Jacobs, Harrison, Parker, Yifan Ding, and Ranga Thiruvenkatachari. The EM27/SUN m-[peasurements during the wildfire season

were collected during the COVID-19 shutdown and could not have happened without my family's generous support. I would like to acknowledge Alondra Moreno and Neha Khushalani for helping me characterize the GC-PID instrument. I would like to thank my funding sources for this work include the National Science Foundation Graduate Research Fellowship Program (NSF-GRFP), University Office of the President (UCOP) Lab Fees Grant, California Air Resources Board (CARB) Contract Number 17MLD040.

The third chapter of this dissertation, in full, is a reprint of the material as it appears in "Ground solar absorption observations of total column CO, CO_2, CH_4, and aerosol optical depth from California's Sequoia Lightning Complex Fire: Emission factors and modified combustion efficiency at regional scales" published within Sensors in 2020 which was authored by Isis Frausto-Vicencio, Sajjan Heerah, Aaron Meyer, Harrison Parker, Manvendra Dubey, and Francesca M. Hopkins. The co-author listed in this publication directed and supervised the research which forms the basis for this dissertation.

The fourth chapter of this dissertation, in full, is a reprint of the material as it appears in "Characterizing the Performance of a Compact BTEX GC-PID for Near-Real Time Analysis and Field Deployment" published within Sensors in 2020 which was authored by Isis Frausto-Vicencio, Alondra Moreno, Hugh Goldsmith, Ying-Kuang Hsu, and Francesca M. Hopkins. The co-author listed in this publication directed and supervised the research which forms the basis for this dissertation.

Many mentors also helped me along the way from community college all the way to now: Charles Rush, Robert Urtecho, Duane Goodwin, Kristal Verhulst, Clare Wong, Preeti Rao, Dilhara Ranasinghe, and Mariel Friberg. Thank you for believing in me and for

all your support over the years. I would also like to thank Juno for making the writing phase a lot easier, whose constant warmth and companionship I can never repay. And finally, a special thanks to Y.Y. for supporting me in this journey.

I would not have made it here without the support of my parents Irma Vicencio and Alberto Frausto, my sisters Scarlett and Dulce, and my brothers Luis and Alexx. You have all sacrificed a lot so I could get here. A mis papas, gracias por regalarme la vida y siempre apoyarme en todo. Los quiero mucho.

To my parents Irma Vicencio and Alberto Frausto,
And my siblings, Luis, Scarlett, Dulce, and Alexx,
For your love and support

ABSTRACT OF THE DISSERTATION

Advances in Atmospheric Trace Gas Monitoring Systems:
Quantification of Methane Sources by Solar Column Observations in the San Joaquin Valley of California and Characterization of a Portable Air Toxics Sensor

by

Isis Frausto-Vicencio

Doctor of Philosophy, Graduate Program in Environmental Sciences
University of California, Riverside, December 2022
Dr. Francesca Hopkins, Chairperson

Anthropogenic trace gases such as greenhouse gases and air toxics emitted to the atmosphere contribute to radiative forcing, degradation of air quality, and negative impacts on human health. Quantification and characterization of these important trace gases are required to mitigate the global climate crisis and improve the air quality. My dissertation focuses on constraining methane (CH_4) emissions from California's San Joaquin Valley (SJV) dairy farms and characterizing wildfire emissions using ground-based solar spectroscopy observations. Additionally, I characterize a portable gas chromatograph coupled to a photoionization detector (GC-PID) for measuring concentrations of air toxics at ambient levels.

In the first study, I studied the seasonality of CH_4 emissions from dairy farms across four seasons from Spring 2019 to Winter 2020 in the SJV to investigate whether emissions varied across time and to discern the environmental factors driving temporal differences. Measurements collected during different seasons provided insight into the meteorological and management factors that drive the time-varying patterns observed during the year. This

research showed that seasonal variability exists within dairy farm emissions and mitigation should focus in the summer.

Wildfires are increasing in the Western United States making it critical to understand the impacts of greenhouse gases and air pollutants emitted to the atmosphere. I used a ground-based remote sensing technique to measure the amount of greenhouse gases and aerosol present in the atmosphere. I isolated a large smoke plume from the Sequoia Lightning Fire Complex (SQF) and calculated variables to understand the fuel properties. This revealed that a significant amount of CH_4 was emitted from the 2020 wildfire season.

In the third study, I characterized the performance of a compact GC-PID and optimize the configuration to detect ambient levels of benzene, toluene, ethylbenzene, and xylene isomers (BTEX). With an analysis time of less than 15 minutes, the compact GC-PID is ideal for field deployment of background and polluted atmospheres for near-real time measurements of BTEX. The results highlight the application of the compact and easily deployable GC-PID for community monitoring and screening of BTEX.

Table of Contents

List of Figures

Appendices

List of Tables

Appendices

Chapter 1: Introduction

1.1 Greenhouse gases and methane

Greenhouse gases alter the Earth's climate by absorbing and emitting infrared radiation in the lower atmosphere. The increase of global greenhouse gas emissions since the preindustrial era (year 1750) has produced a radiative forcing of +3.32 Wm^{-2} with carbon dioxide (CO_2) being responsible for 65% of the radiative forcing from greenhouse gases (Forster et al., 2021). The remaining balance is from non-CO_2 greenhouse gases such as methane (CH_4; 16%), nitrous oxide (N_2O; 6%), and halocarbons (12%). These non-CO_2 greenhouse gases have more of a significant impact on the climate than CO_2 due to their high global warming potential (GWP) that enables the trapping of heat more effectively per unit mass.

Methane is a potent greenhouse gas and has a more powerful effect on the atmosphere than CO_2 due to its GWP of 86 over a 20-year time scale (IPCC, 2014). Its GWP has become a concern as global CH_4 levels have risen sharply since the pre-industrial era due to the imbalance between sources and sinks; levels have more than doubled increasing from 722 ppb to 1875 ppb (Dlugokencky et al., 2011). Methane's strong GWP combined with its relatively short atmospheric lifetime of 12 years makes it an ideal target for mitigating the global climate crisis and meeting greenhouse reduction targets proposed by national and global organizations (UNEP, 2022).

Global CH_4 continues to increase primarily due to intensification of agriculture activities, waste management and oil and natural gas (ONG) production (Jackson et al.,

2020; Saunois et al., 2020). In California, dairy farms, landfills, and ONG industries are the largest sources of CH_4 contributing 56%, 22%, and 19% to the CH_4 statewide emissions and have increased by 19, 19, and 11% between 2000 and 2019, respectively (CARB, 2019). Regionally, the San Joaquin Valley (SJV) contains a large portion of ONG and dairy sources and has the largest CH_4 emissions (0.94 ± 0.18 Tg/yr) in the state (Cui et al., 2019). The SJV is home to 90% of the state's cattle that emit significant amounts of CH_4 through the dairy cattle's enteric fermentation and farm's manure management (USDA, 2017).

1.2 Air toxics and BTEX

Air pollutants and air toxics are regulated by governmental agencies including the Environmental Protection Agency (EPA) and the California Air Resources Board (CARB) under the Clean Air Act. These organizations set standards for pollutant levels that are considered safe for the population to breathe. As rules and regulations have been implemented such as the requirement of a catalytic converter in vehicles, air quality has improved, however some pollutants like benzene, ethylbenzene, toluene, and xylenes (BTEX) are still of concern for residents living near freeways and ONG sources (Bretón et al., 2017; Houghton et al., 1999). Prolonged exposure to the toxic volatile organic compound (VOC) family of benzene, toluene, ethylbenzene, and xylene isomers (BTEX) is known to be carcinogenic to humans and may have adverse health effects on immune, metabolic, respiratory functioning as well as development (Bretón et al., 2017). This is particularly important for densely populated areas located within proximity to ONG and traffic sources. The Occupational Safety and Health Administration (OSHA) set a fixed standard of 1 ppm over an 8-hour averaging time for benzene. Ambient levels of BTEX

are often sub ppb levels but may be higher near traffic source and ONG activities (Weisel, 2010).

1.3 Motivation for Current Research

Under California's Global Warming Solutions Act of 2006 (Assembly Bill 32), the state mandated that greenhouse gases emissions were reduced to 1990 levels by 2020 and is currently committed to 40% reductions below 1990 levels by 2030 for all greenhouse gases (Senate Bill 32). In 2015, Assembly Bill 1496 required the state to locate and monitor CH4 hotspots. In 2016, Senate Bill 1383 specifically targeted the reduction of CH4 to 40% below 2013 levels by 2030 and called for the reduction of CH4 emissions from landfills, dairy livestock operations, and fugitive emissions from oil and gas to meet the reduction targets. Dairy farms, landfills, and ONG activities are the three largest contributors to the state's CH_4 budget, and as such, are critical to study for these regulations to be effective. Additionally, the understanding of how biogenic sources, such as wildfires, may contribute CH_4 to the total budget will become important as climate changes and wildfires become more intense and frequent in the future.

Many of the factors controlling greenhouse gas emissions are poorly quantified contributing to discrepancies between activity-based bottom-up inventories and top-down estimates derived from atmospheric observations. Several studies have determined that inventory-based CH_4 budget in the state are underestimated by up to a factor of 2 (Cui et al., 2017; Guha et al., 2015; Jeong et al., 2013, 2016; Wecht et al., 2014) Therefore, improved flux estimations at local scales are needed to resolve discrepancies between bottom-up and top-down approaches to ensure the success of CH_4 mitigation actions. While

progress has been made to constrain emissions of CH_4, there is a lack of atmospheric-based observations to independently verify emissions and understand the inter-annual variability from the major CH_4 sources. The California bottom-up emissions inventory for CH_4 uses emission factors based on annually averaged meteorological inputs. The neglect of seasonal and spatial differences can introduce uncertainties in the CH_4 emission factor that are used to calculate the emissions inventories.

Although dairies dominate the CH_4 source in the SJV, other emerging sources of CH_4 may be important. California's recent wildfire events are becoming more frequent and disastrous releasing large amounts of carbon in the form of CO_2, CO and CH_4 from biomass burning (Gutierrez et al., 2021; Navarro et al., 2016). The state currently reports wildfire CO_2 emissions separately from anthropogenic sources and does not report the amount of CH_4 generated from the burning of biomass (CARB, 2020). The accurate apportionment of CH_4 in mixed source regions like the SJV will become increasingly important as wildfires have been frequently igniting in the Sierra Nevada and contributing fire-derived CH4 to the local atmosphere. The SJV saw high smoke days during the summers of 2020 and 2021 adding to the already present greenhouse gas burden in the SJV (Cho et al., 2022). Apportioning CH_4 emissions to their source and determining an accurate emissions quantification per sector are ongoing challenges for meeting California's ambitious climate goals and combating the global climate crisis.

Recent studies have shown elevated BTEX levels in urban areas and near ONG sources, however analytical methods limit the characterization and understanding of spatial distributions of BTEX in communities. Identifying the fine-scale spatial patterns of BTEX

hotspots can improve the accuracy of human exposure estimates of the surrounding communities and inform mitigation policy. We optimize the design of a GC-PID to detect ambient levels of BTEX and test the performance in laboratory and field settings for future studies focus on characterizing ambient concentrations and associated uncertainties for impacted communities.

1.4 Overview of this Research

In this dissertation, two long-term field campaigns were conducted in the SJV of California to investigate CH_4 sources and emissions and one short term field campaign to investigate BTEX concentrations from roadways:

1) Seasonal study of CH_4 from dairy farms in the SJV took place at dairy farms north of Visalia, California (September 2018, March, June, and September 2019, and January 2020).
2) Remote sensing observations of CH_4, CO_2, CO, and aerosol optical depth (AOD) from the wildfires in the Sierra Nevada took place in Farmersville, California (September – October 2020).
3) Mobile observations of BTEX took place in Riverside, California (February 2020).

The structure of this thesis is as follows. In Chapter 2, I quantify CH_4 emissions from a 10x10 km^2 dairy cluster in the SJV using a network of ground-based remote sensing solar spectrometers to detect enhancements of CH_4. I measured over the course of 1 year

and explored how emissions change with seasons. I find that summer emissions are higher, followed by winter and the lowest emission were in spring and fall.

In Chapter 3, I explore the use of ground-based solar spectroscopy as a new technique for studying wildfire emissions. I isolated a large wildfire plume that originated in the Sierra Nevada and calculate emission factors and modified combustion efficiency, two variables that describe fuel properties and combustion phase of the fire. I derive the AOD during the first few weeks of the fire and compare to a nearby AERONET site. Additionally, I calculate the amount of CH_4 emitted from the wildfire using the state's CO_2 wildfire inventory and field-based emission ratios. The novel application of the solar spectrometer to quantify wildfire emission ratios at large scales follows predictive relationships that are consistent with in situ studies, offering promise for extensive monitoring from ground networks and satellite remote sensing.

In Chapter 4, I describe a portable GC-PID that I developed and optimized to measure and speciate for BTEX at ambient levels. I describe the performance of the instrument in laboratory and field settings including at different environmental conditions and in mobile campaign mode. I find that the GC-PID technique can speciate and detect BTEX at sub ppb levels showing great promise for screen for characterizing BTEX at a higher spatial resolution with possibility of establishing dense networks of VOC measurements.

In Chapter 5, I briefly summarize the results of the studies and field campaigns. I pose future research questions and directions for greenhouse gas research in California,

remote sensing observations of dairy farms and wildfires, and future measurements of BTEX sources with the portable GC-PID.

1.5 References

Bretón, J. G. C., Bretón, R. M. C., Ucan, F. V., Baeza, C. B., Fuentes, M. de la L. E., Lara, E. R., et al. (2017). Characterization and Sources of Aromatic Hydrocarbons (BTEX) in the Atmosphere of Two Urban Sites Located in Yucatan Peninsula in Mexico. *Atmosphere*, *8*(12), 107. https://doi.org/10.3390/atmos8060107

CARB. (2017). California's 2017 Climate Change Scoping Plan, 132.

CARB. (2019). Methane (CH4). Retrieved November 25, 2020, from https://ww3.arb.ca.gov/cc/inventory/background/ch4.htm

CARB. (2020). California Wildfire Emission Estimates. Retrieved May 30, 2021, from https://ww2.arb.ca.gov/wildfire-emissions

Cho, C., Kim, S.-W., Choi, W., & Kim, M.-H. (2022). Significant light absorption of brown carbon during the 2020 California wildfires. *Science of The Total Environment*, *813*, 152453. https://doi.org/10.1016/j.scitotenv.2021.152453

Cui, Y. Y., Brioude, J., Angevine, W. M., Peischl, J., McKeen, S. A., Kim, S.-W., et al. (2017). Top-down estimate of methane emissions in California using a mesoscale inverse modeling technique: The San Joaquin Valley: Methane Emission Estimates in SJV of CA. *Journal of Geophysical Research: Atmospheres*, *122*(6), 3686–3699. https://doi.org/10.1002/2016JD026398

Cui, Y. Y., Vijayan, A., Falk, M., Hsu, Y.-K., Yin, D., Chen, X. M., et al. (2019). A Multiplatform Inversion Estimation of Statewide and Regional Methane Emissions in California during 2014–2016. *Environmental Science & Technology*, *53*(16), 9636–9645. https://doi.org/10.1021/acs.est.9b01769

Dlugokencky, E. J., Nisbet, E. G., Fisher, R., & Lowry, D. (2011). Global atmospheric methane: budget, changes and dangers. *Philosophical Transactions of the Royal Society A: Mathematical, Physical and Engineering Sciences*, *369*(1943), 2058–2072. https://doi.org/10.1098/rsta.2010.0341

Forster, P., Storelvmo, T., Armour, K., Collins, W., Dufresne, J.-L., Frame, D., et al. (2021). The Earth's energy budget, climate feedbacks, and climate sensitivity. In V. Masson-Delmotte, P. Zhai, A. Pirani, S. L. Connors, C. Péan, S. Berger, et al. (Eds.), *Climate Change 2021: The Physical Science Basis. Contribution of Working Group I to the Sixth Assessment Report of the Intergovernmental Panel on Climate Change* (pp. 923–1054). Cambridge, United Kingdom and New York, NY, USA: Cambridge University Press. https://doi.org/10.1017/9781009157896.001

Guha, A., Gentner, D. R., Weber, R. J., Provencal, R., & Goldstein, A. H. (2015). Source apportionment of methane and nitrous oxide in California's San Joaquin Valley at CalNex 2010 via positive matrix factorization. *Atmospheric Chemistry and Physics*, *15*(20), 12043–12063. https://doi.org/10.5194/acp-15-12043-2015

Gutierrez, A. A., Hantson, S., Langenbrunner, B., Chen, B., Jin, Y., Goulden, M. L., & Randerson, J. T. (2021). Wildfire response to changing daily temperature extremes in California's Sierra Nevada. *Science Advances*, *7*(47), eabe6417. https://doi.org/10.1126/sciadv.abe6417

Houghton, M., Dodge, D., Krieger, R., Johnson, Jackie, Mazur, L., & Pomales, T. (1999). *Update to the Toxic Air Contaminant List* (p. 44). Sacramento, CA, USA: California Air Resources Board.

Jackson, R. B., Saunois, M., Bousquet, P., Canadell, J. G., Poulter, B., Stavert, A. R., et al. (2020). Increasing anthropogenic methane emissions arise equally from agricultural and fossil fuel sources. *Environmental Research Letters*, *15*(7), 071002. https://doi.org/10.1088/1748-9326/ab9ed2

Jeong, S., Hsu, Y.-K., Andrews, A. E., Bianco, L., Vaca, P., Wilczak, J. M., & Fischer, M. L. (2013). A multitower measurement network estimate of California's methane emissions: CALIFORNIA'S METHANE EMISSIONS. *Journal of Geophysical Research: Atmospheres*, *118*(19), 11,339-11,351. https://doi.org/10.1002/jgrd.50854

Jeong, S., Newman, S., Zhang, J., Andrews, A. E., Bianco, L., Bagley, J., et al. (2016). Estimating methane emissions in California's urban and rural regions using multitower observations. *Journal of Geophysical Research: Atmospheres*, *121*(21), 13,031-13,049. https://doi.org/10.1002/2016JD025404

Navarro, K. M., Cisneros, R., & Balmes, J. R. (2016). Air-Quality Impacts and Intake Fraction of PM2.5 during the 2013 Rim Megafire. *Environ. Sci. Technol.*, 9.

Prichard, S. J., O'Neill, S. M., Eagle, P., Andreu, A. G., Drye, B., Dubowy, J., et al. (2020). Wildland fire emission factors in North America: synthesis of existing data, measurement needs and management applications. *International Journal of Wildland Fire*, *29*(2), 132. https://doi.org/10.1071/WF19066

Saunois, M., Stavert, A. R., Poulter, B., Bousquet, P., Canadell, J. G., Jackson, R. B., et al. (2020). The Global Methane Budget 2000–2017. *Earth System Science Data*, *12*(3), 1561–1623. https://doi.org/10.5194/essd-12-1561-2020

UNEP. (2022). *Spreading like Wildfire – The Rising Threat of Extraordinary Landscape Fires* (A UNEP Rapid Response Assessment.). Nairobi: United Nations Environment Programme.

USDA. (2017). USDA - National Agricultural Statistics Service - 2017 Census of Agriculture - Volume 1, Chapter 2: County Level Data. Retrieved December 9, 2020, from

Wecht, K. J., Jacob, D. J., Sulprizio, M. P., Santoni, G. W., Wofsy, S. C., Parker, R., et al. (2014). Spatially resolving methane emissions in California: constraints from the CalNex aircraft campaign and from present (GOSAT, TES) and future (TROPOMI, geostationary) satellite observations. *Atmospheric Chemistry and Physics*, *14*(15), 8173–8184. https://doi.org/10.5194/acp-14-8173-2014

Weisel, C. P. (2010). Benzene exposure: An overview of monitoring methods and their findings. *Chemico-Biological Interactions*, *184*(1–2), 58–66. https://doi.org/10.1016/j.cbi.2009.12.030

Xu, Q., Westerling, A. L., Notohamiprodjo, A., Wiedinmyer, C., Picotte, J. J., Parks, S. A., et al. (2022). Wildfire burn severity and emissions inventory: an example implementation over California. *Environmental Research Letters*, *17*(8), 085008. https://doi.org/10.1088/1748-9326/ac80d0

Chapter 2: Solar column based CH_4 emission estimates of dairy farms at local scales in the San Joaquin Valley

Acknowledgement of Co-Authorship

This work was completed with contributions from Isis Frausto-Vicencio, Sajjan Heerah, Marc L. Fischer, Alison R. Marklein, Yifan Ding, Ranga R. Thiruvenkatachari, Harrison A. Parker, Seongeun Jeong, Aaron G. Meyer, Akula Venkatram, Manvendra Dubey, Francesca M. Hopkins.

Abstract

California dairy farms are estimated to emit close to 50% of the state's methane (CH_4) emissions, but the magnitude and the intra-annual variability from the dairy CH_4 source is highly uncertain. Quantifying and reducing CH_4 is critical for meeting California's climate targets and mitigating climate change. To help constrain CH_4 emissions from California dairies, we studied variations in dairy CH_4 emissions across four seasons from spring 2019 to winter 2020. We measured total atmospheric column gradients (ΔXCH_4) from a dense group of dairies in the San Joaquin Valley (SJV) using portable EM27/SUN solar-viewing spectrometers placed upwind and downwind of ~40 dairy farms housing >30,500 cows. Measurements collected during different seasons provide insight into the meteorological factors that drive the time-varying patterns observed during the year. We estimate CH_4 emissions using a mass balance approach and compare observed emissions to a facility-level emission prior. Analysis of the EM27/SUN measurements suggests that CH_4 fluxes were larger in summer. We discuss these results in the context of bottom-up modeling driven by seasonal variations in farm management and climate. This

study will help constrain CH_4 emissions from California dairies, examine how seasonal variability should be handled in these emissions estimates, and demonstrate new modeling approaches for analyzing XCH_4 data at these fine scales.

2.1 Introduction

Global atmospheric methane (CH_4) concentrations continue to rise mainly due to intensification of emissions from agriculture activities, waste management, and oil and natural gas (ONG) production (Jackson et al., 2020; Saunois et al., 2020). CH_4 is a potent greenhouse gas with a global warming potential (GWP) of 86 over a 20-year time scale (IPCC, 2014) and for this reason has become a concern. The latest global CH_4 budget estimates that agricultural sources enteric fermentation and manure management on dairy operations contribute 15% to the total emissions (Jackson et al., 2020). Methane's strong GWP combined with its relatively short atmospheric lifetime of 12 years makes it an ideal target for mitigating climate change and meeting greenhouse reduction targets proposed by national and global organizations (Chen et al., 2016; Viatte et al., 2017).

In California, the dairy sector is the largest sources of CH_4 contributing 54% of the CH_4 statewide emissions. Additionally, the emissions have increased by 20% between 2000 and 2018, respectively (CARB, 2019; CARB, 2020). Regionally, the San Joaquin Valley (SJV) has the largest CH_4 emissions (0.94 ± 0.18 Tg/yr) in the state (Cui et al., 2019) and is home to 90% of the state's dairy cattle that emit significant amounts of CH_4 through the dairy cattle's enteric fermentation and the farm's manure management (USDA, 2017). Dairy farms in the SJV region use primarily a wet manure management method that

involves storing the manure in lagoons and ponds where it anaerobically decomposes to produce CH_4 (Meyer et al., 2011). Methane is also generated through enteric fermentation by gut microbes in the cow rumen that is dependent on the composition of animal feed (Moraes et al., 2014). However, many of the factors controlling dairy farm emissions are poorly quantified, which contributes to nearly 2-fold discrepancies between activity-based bottom-up inventories and top-down estimates derived from atmospheric observations (Cui et al., 2017; Jeong et al., 2016; Miller et al., 2013; Trousdell et al., 2016). Additionally, new mitigation techniques are being introduced to dairy farm manure management practices such as digesters and identifying the ideal measurement technique to capture changes will be necessary.

California's regulatory bottom-up inventory for CH_4 from manure management and enteric fermentation uses emission factors based on annually averaged meteorological inputs set by the IPCC (CARB, 2019; Marklein et al., 2021). This neglects seasonal and spatial differences in emissions that can introduce uncertainties in the CH_4 emission factor that are used to calculate the inventory. For example, a study of two dairy facilities in the SJV of California found that CH_4 emissions from a liquid manure storage were between 3-6 times higher in the summer than in the winter, accounting for 70-80% of total annual CH_4 emissions (Arndt et al., 2018). Additional seasonal studies are necessary to understand how CH_4 emissions from dairies change throughout the year, and how to extrapolate beyond measurement periods to annual estimates.

Solar column gradients have previously been employed to estimate CH_4 emissions from dairy farms in Southern California following the differential column measurement

technique with the EM27/SUN solar-tracking Fourier-transform solar spectrometers (FTS) (Chen et al., 2016; Viatte et al., 2017). Chen et. al (2016) demonstrated that a mass balance approach can be applied to measurements at upwind and downwind locations using a differential column technique to estimate emissions from a local source. Viatte et al. (2017) utilized a Weather Research and Forecasting model in large-eddy simulation mode (WRF-LES) to model emissions from a group of dairy farms in a 6 km x 9 km area. Both methods proved to be effective in estimating emissions from dairy farms at the 1-10 km local scale. Column measurements are sensitive to sources nearby, regional, and continental scales. Using two or more solar column instruments, the long-range influence of time variations in the CH_4 mole fraction of the incoming air mass can be reduced with simultaneous measurements at upwind and downwind locations (Chen et al., 2016). The EM27/SUN instruments have also been deployed for urban emissions studies to measure gradients and estimate emissions of CO_2 and CH_4 (Dietrich et al., 2021; Jacobs et al., 2020; Jones et al., 2021; Makarova et al., 2020; Vogel et al., 2019; Zhao et al., 2019).

In this study, we deployed EM27/SUN solar spectrometers to measure atmospheric columns of methane (X_{CH4}) upwind and downwind of a small cluster of dairy farms in the SJV to estimate their emissions. The different environmental conditions across seasons in which we measured allow us to explore how farm management practices and temperature may influence CH_4 emissions across seasons. The goals of this study are to help constrain CH_4 emissions from California dairies, to examine how seasonal variability should be handled in these emissions estimates, and to demonstrate new modeling approaches for analyzing atmospheric columns of CH_4 at fine scales.

2.2 Methods

2.2.1 Study site

Tulare County produces the most dairy products in the U.S. (USDA, 2017). The USDA 2017 Census estimated there were about 1 million (1,057,272) cattle and calves in Tulare County with milk cows (500,402) accounting for 47% of the county's total livestock (USDA, 2017). We chose an isolated area with ~40 dairy farms north of the City of Visalia in Tulare County to estimate CH_4 emissions from dairy farms using differential column measurements with mobile solar spectrometers. These measurements are described in the sections below and the setup is illustrated in Figure 2.1.

2.2.2 Differential column measurements

We used the differential column measurement technique to measure gradients in total column of methane (ΔX_{CH4}) of an area north of Visalia, CA containing a cluster ("the cluster") of 41 dairy farms, 2 feedlots, and 1 landfill with an estimated total CH_4 emissions of 29.7 Gg/yr (Marklein et al., 2021). Within the cluster we further targeted dairy farms in the area highlighted in Figure 2.1c. The dairy farms within the target area house more than 30,500 milking cows and represent a variety of dairy farm sizes with individual farms housing 1,000 to 6,000 milking cows each. The majority of the farms within the cluster have a freestall feeding system consisting of a flush system that flows into the manure storage lagoons (Meyer et al., 2011).

Prevailing wind directions in the SJV are from the northwest driven by the winds entering the San Francisco Bay and flowing to the southeast along the Valley (Frenzel, 1962). The northwest corner of the dairy cluster was selected to measure a local

background whereas the downwind instrument captured CH_4 enhancements as the air column traveled southeast across the dairies (Figure 2.1). The cluster is located 11 km north of the City of Visalia, such that it is upwind of the urban area under predominant northwesterly winds at midday. To the south and west of Visalia is another dairy area with the highest concentration of dairy farms in the SJV. Crop agricultural land surrounds the upwind and downwind sites with few nearby CH_4 sources and is about 40 km away from upwind urban methane emissions from Fresno. This cluster of dairies is in relatively simple terrain, with 1 m of altitude difference between the upwind and downwind measurement sites. The cluster of dairies is located 20 km west of the Sierra Nevada foothills. Winds at sites close to the sidewall slopes reverse direction during the day which can be difficult to model (Zhong et al., 2004).

Measurements at the SJV dairy cluster took place over 5 to 6 days in each of the 4 seasons from March 2019 until January 2020. Total column averages of CH_4 were measured continuously between 10 am and 6 pm at the upwind and downwind locations. The upwind location was consistent between measurement days, while the downwind location varied per day dependent on forecasted winds to maximize sensitivity to dairies of interest (Figure 2.1).

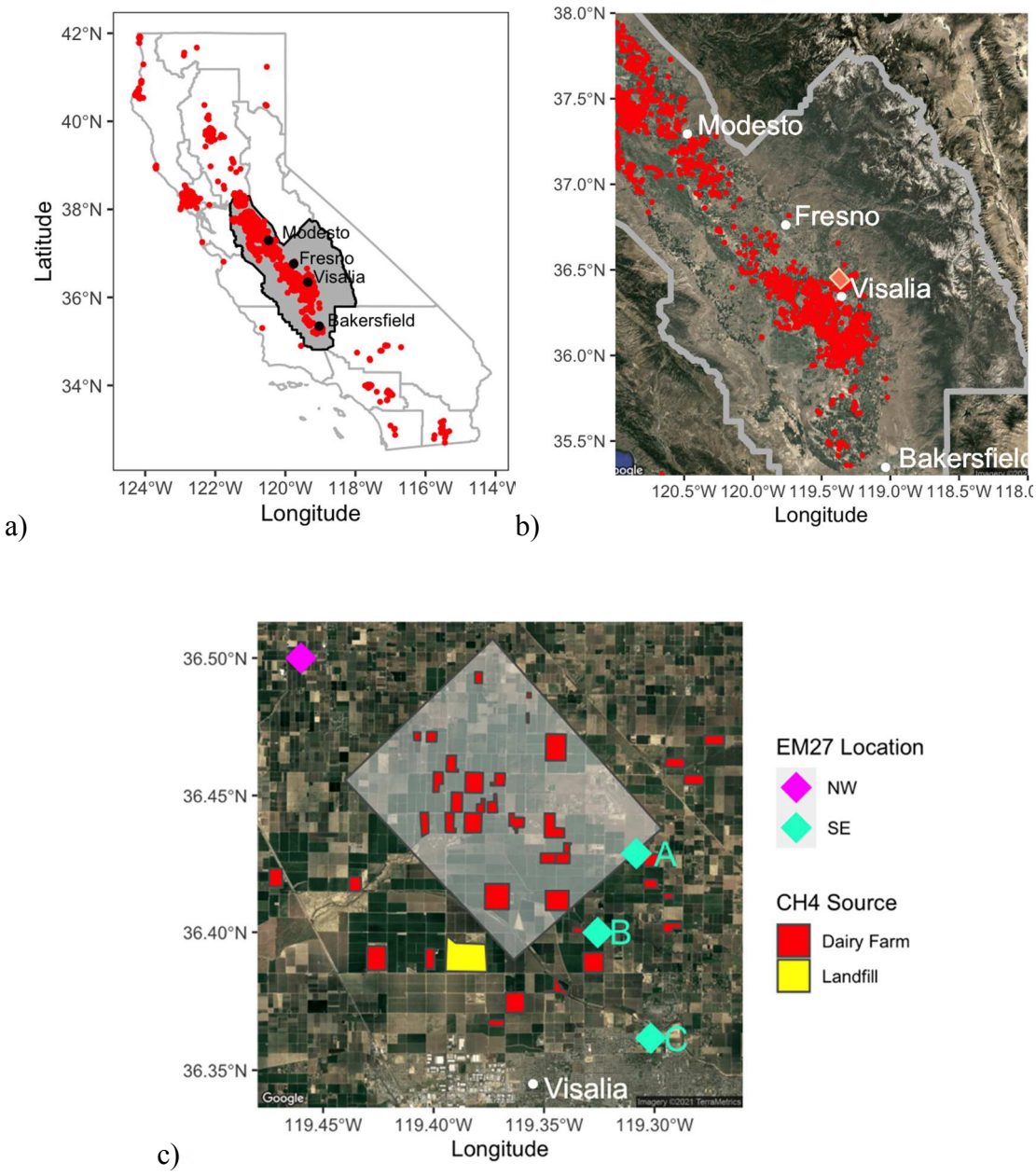

Figure 2.1. a) Dairy farms (shown in red) in California are concentrated in the San Joaquin Valley (SJV, shown in gray). b) Differential column measurements of methane were taken across a cluster of dairy farms in the SJV north of Visalia (yellow highlighted area). c) The EM27/SUN measurement locations northwest and southeast of the dairy farm cluster are represented by diamond shapes with the three downwind locations denoted as A, B or C, dependent on forecasted wind conditions. The target 8 x 10 km^2 area of dairy farms is highlighted, with dairy farms shown in red polygons and a nearby landfill represented by a yellow polygon.

2.2.3 EM27/SUN Fourier transform spectrometer

Atmospheric column-averaged dry-air mole fractions (X_{gas}) of CH_4, CO_2, carbon monoxide (CO), and water (H_2O) were retrieved from the EM27/SUN solar-viewing Fourier Transform Spectrometer (FTS). We use the same Bruker Optics EM27/SUN instruments as in Chen et al., (2016) and Viatte et al., (2017), designated as UA, DN, and HA (Bruker Optics nos. 34, 42, and 45), owned by Los Alamos National Laboratory (LANL), NASA Jet Propulsion Laboratory (NASA-JPL), and Harvard University, respectively. The EM27/SUN instrument is further described and characterized elsewhere (Gisi et al., 2012; Hedelius et al., 2016). The X_{gas} is retrieved from measured interferograms processed by the I2S and GFIT (GGG2014 version) retrieval algorithms automated by the EGI processing suite (Hedelius et al., 2016). Surface pressure is required to retrieve dry air columns in GGG and we use Coastal Environmental Systems ZENO weather station to record surface pressure for retrievals. Retrievals also require atmospheric profiles of temperature, pressure, altitude and water and these profiles were extracted from NCEP/NCAR reanalysis product (Kalnay et al., 1996).

Extensive side-by-side measurements of the EM27/SUN instruments with instruments from the Total Column Carbon Observing Network (TCCON) were done before and after each measurement period to ensure system stability, correct for any biases, and tie our measurements to the World Meteorological Organization (WMO) scale. Differences between instruments can be due to resolution, instrument imperfections and instabilities, and instruments can drift noticeably when measuring over several months (Hedelius et al., 2016). For this reason, the EM27/SUN instruments were co-located within

a few meters from the aperture of the IFS125, high-resolution spectrometers that constitute TCCON, located at the California Institute of Technology (CIT) and NASA Armstrong. The ua instrument (LANL) was used during every collection period and used as a transfer standard to other instruments when the CIT TCCON instrument was not operational (Spring 2019 field campaign).

To determine calibration factors, we assume a linear model forced through the origin for each gas: $X_{TCCON} = X_{EM27} R_{CH4}$ (Chen et al., 2016; Hedelius et al., 2016). We consider the different averaging kernels of the EM27/SUN and TCCON instrument following Hedelius et al's., (2016) Equation A4 to adjust the EM27/SUN retrievals before comparing with TCCON. A summary of the correction factors is shown Appendix A1, Figure A1.1

2.2.4 Wind observations

We made micrometeorological measurements during all campaign periods at a single location inside the cluster dairy area (Figure 2.1c) with two 3-D sonic anemometers (CSAT3, Campbell Scientific, Inc.) mounted on a stationary tower at 3 and 10 m. We utilized winds measured at 10 m to drive a simple column model to estimate CH_4 emissions. Figure 2.2 shows wind conditions observed during seasonal measurement periods in March, June, and September 2019, and January 2020. The summer and fall months, June, and September, had consistent northwest wind directions with higher mean wind speeds of 3.28 and 2.64 m/s, respectively, while the winter and spring months, January, and March, were variable in wind direction with lower mean wind speeds of 1.89 and 1.75 m/s, respectively.

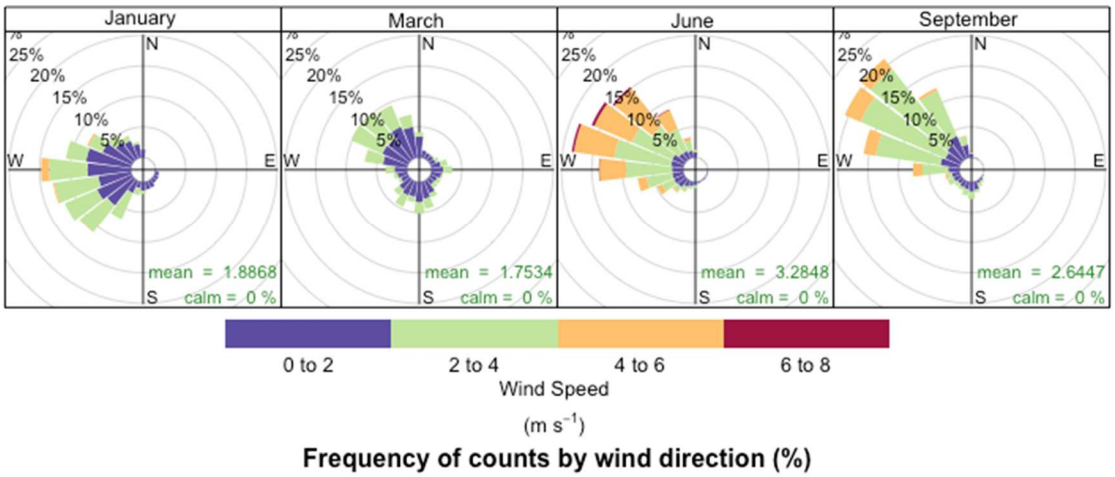

Figure 2.2. Wind roses from sonic anemometer located within the dairy cluster. Data shown is only during measurement periods.

2.2.5 Mass balance technique for estimating emissions of CH_4

We used a differential column measurements technique, and we adapted the simple column model described by Chen et al. (2016) to calculate CH_4 emissions from the solar column measurements. The column-averaged dry-air mole fractions of CH_4 (X_{CH4}) were measured simultaneously northwest and southeast of a cluster of dairies in the SJV for several days during March, June, and September of 2019, and January of 2020. During the January campaign we had three EM27/SUN instruments and were able to set two downwind SE sites. The dairies in the SJV are sparse (Figure 2.1) compared to the dairy farms studied in Southern California by Chen et al. (2016) and Viatte et al. (2017) where uniform emissions were assumed over the 6 x 9 km Chino dairy area. The assumption of spatially uniform emissions is likely the largest source of error for this technique and may lead to overestimating dairy emissions. To mitigate this error, rather than assuming a uniform emission across the dairy cluster area, we modify Chen's mass balance equation

to instead consider the area and length of dairy farm transected by the wind vectors. We also assume that air masses are well mixed horizontally as air masses transit over dairy farms.

The CH_4 emission rate (E_{CH4}) is computed as the product of the CH_4 enhancement (ΔX_{CH4}, ppb) (Equation 1), the mass-enhancement weighted wind velocity ($\overline{U}$, m/s), the vertical column air density (SC_{air}, molecules/m^2), and the area of the total dairy farm area (A_{Dairy}, m^2) intersected by the wind vectors during each sampling period and is inversely proportional to the length of dairy farm intersected (L_{Dairy}, m) (Equation 2).

$$\Delta X_{CH4} = X_{CH4,\ downwind} - X_{CH4,\ upwind} \quad (1)$$

$$E_{CH4} = \frac{\Delta X_{CH4}\ SC_{air}\ \overline{U}\ A_{Dairy}}{L_{Dairy}} \quad (2)$$

As suggested by Chen et al., (2016), we average X_{CH4} and other meteorological variables at 5 minutes to study emissions at local scales. The mean wind speed was obtained from the sonic anemometer present within the cluster of dairy farms further described in Section 2.2.4. To determine $\overline{U}$, a wind profile is approximated from 10 m to a mixing height (z_{emiss}) assuming a log profile at neutral stability conditions (Chen et al., 2016, Equations 11 and 13). The area density SC_{air} was calculated from pressure measured at the surface by the ZENO weather station. The area of each dairy farm within the cluster was estimated by mapping polygons over dairy farms in Google Earth. We examined the intersection of 5-minute averaged wind vectors with dairy farms to estimate A_{Dairy} as the total area of intersected dairies, and L_{dairy} as the average length of wind vectors intersecting the dairy farms. An example of this can be found in the Appendix A1, Figure A1.2. The 5-minute emission estimates were then averaged over a day. The mean daily emission

estimates are reported for each season with an uncertainty determined by the standard error of the mean.

To apply the differential column measurements technique for estimating emissions from the dairy cluster, northwesterly winds are required to capture both a clean local background and an enhancement as an air mass travels over the dairies. We selected measurement periods where the wind conditions were favorable by filtering measurement periods for northwest winds ($270° \geq \overline{U} \leq 360°$) and wind speeds higher than 1 m/s. Due to the influence of wind direction on the magnitude of X_{CH4} observed from other dairies outside the cluster as discussed in Section 2.3.1, we remove initial observations to ensure we sampled the same airmass at both sites based on estimates of the time lag it took the air mass entering the domain to reach the downwind instrument. Half the travel time that it took the airmass to transit across the cluster was calculated as the ratio of distance between instruments and wind speed. We did not use measurement periods where the wind was from the south or east and excluded days where the greater SJV dairy farms primarily located south of our study area influenced measurements. Greater SJV dairy CH_4 influence was verified by the footprint of the EM27/SUN from the atmospheric transport model WRF-STILT (Appendix A1, Figure A1.3).

2.3 Results

2.3.1 Observed gradients of X_{CH4}

We observed gradients in X_{CH4} between our NW and SE instruments that varied strongly over the course of the day with wind patterns. When predominant winds were from the NW, we observed positive ΔX_{CH4} values ranging from 2.1 to 23.7 ppb, with a

mean of 9.9 ± 5.7 ppb across seasons. Variability on the order of minutes in X_{CH4} in the timeseries is attributed to concentrated CH_4 plumes traversing over the instruments, representing the influence from dairy farm activities at local scales. This difference between two instruments illustrates the ability of the differential column method to capture a CH_4 enhancement from this dairy cluster. The ΔX_{CH4} means are 8.57 ± 0.59, 9.40 ± 0.54, 3.95 ± 0.28, and 17.70 ± 1.86 (SEM, standard error of the mean) ppb for March 2019, June 2019, September 2019, and January 2020, respectively.

Occasional periods of S/SE winds, such as on the mornings of March 24 & 30, and during March 26, inverted the direction of the gradient. Many dairy farms are found to the south and west of the dairy farm cluster (Figure 2.1, b), and consequently during southerly wind periods the EM27/SUN instruments were sensitive to a different group of dairy farms in the greater SJV. Regional influence from dairy farms in the greater SJV is prominent during the early mornings before the southerly wind direction shifted to northerly winds. On some days, the influence of the large concentration of dairies SW of Visalia were observed (6/24, 9/11, 9/13, 02/02) measuring elevated X_{CH4} at both the NW and SE sites, while other days only one instrument captured the emissions from the greater SJV dairies (3/24, 3/30, 6/21, 6/22), suggesting spatially heterogenous wind conditions between the two sites (Appendix A1, Figure A1.3). On the contrary, when the wind direction was steadily from northwest, we measured consistently lower X_{CH4} than when the wind direction is from the south at both sites, suggesting we only were sensitive to the smaller group of dairies of interest (i.e., ~40 dairy farm cluster).

We filtered the data to isolate conditions that enabled us to detect the signal from the cluster. A total of 20 measurements days were collected between March of 2019 and January 2020. After filtering for ideal conditions (NW winds > 1 m/s) and removing days with greater SJV dairy farm emissions (e.g., 3/24 and 3/30), only 15 days met the filtering criteria and X_{CH4} values used to estimate emissions are shown as colored highlighted areas in Figure 2.3. The observed day-to-day variability in X_{CH4} in all seasons suggests a strong dependence on meteorological factors such as wind speeds and a diurnal cycle driven by wind directional shifts. The wind direction was predominantly from Northwest during the summer and fall months while it was more variable during the winter and spring months (Figure 2.2).

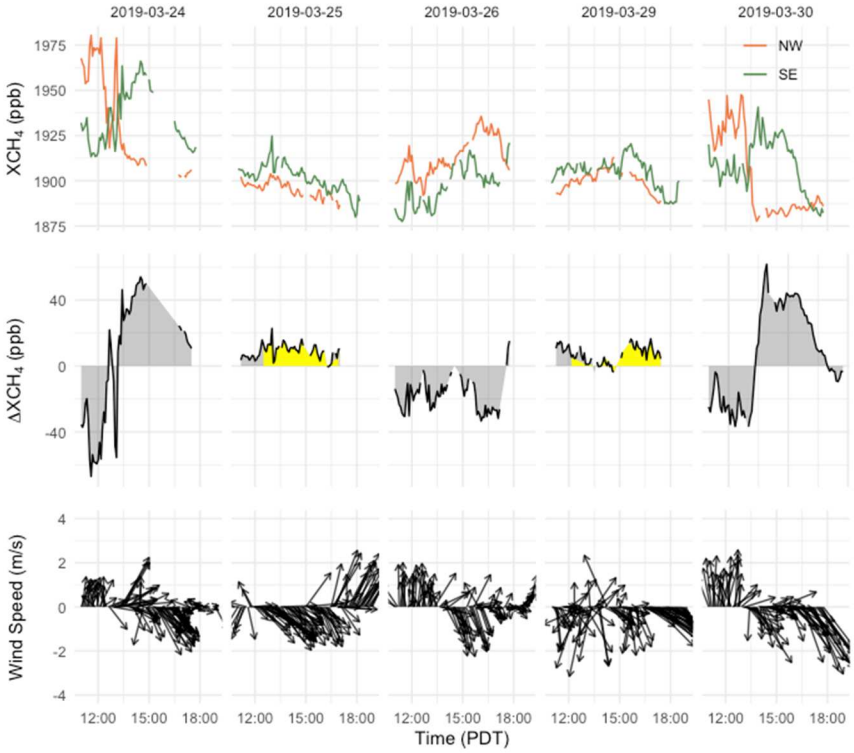
2019-03-24
2019-03-25
2019-03-26
2019-03-29
2019-03-30
NW
SE
XCH4 (ppb)
1975
1950
1925
1900
1875
ΔXCH4 (ppb)
40
0
-40
Wind Speed (m/s)
4
2
0
-2
-4
12:00
15:00
18:00
Time (PDT)

a)

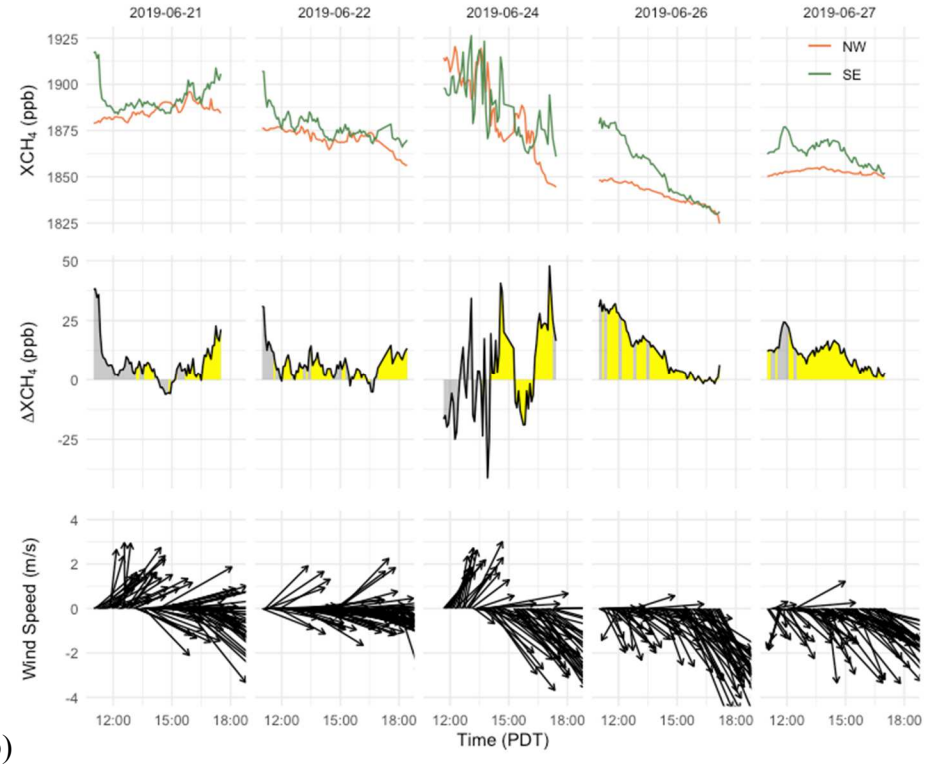
2019-06-21
2019-06-22
2019-06-24
2019-06-26
2019-06-27
NW
SE
XCH4 (ppb)
ΔXCH4 (ppb)
Wind Speed (m/s)
12:00
15:00
18:00
Time (PDT)

b)

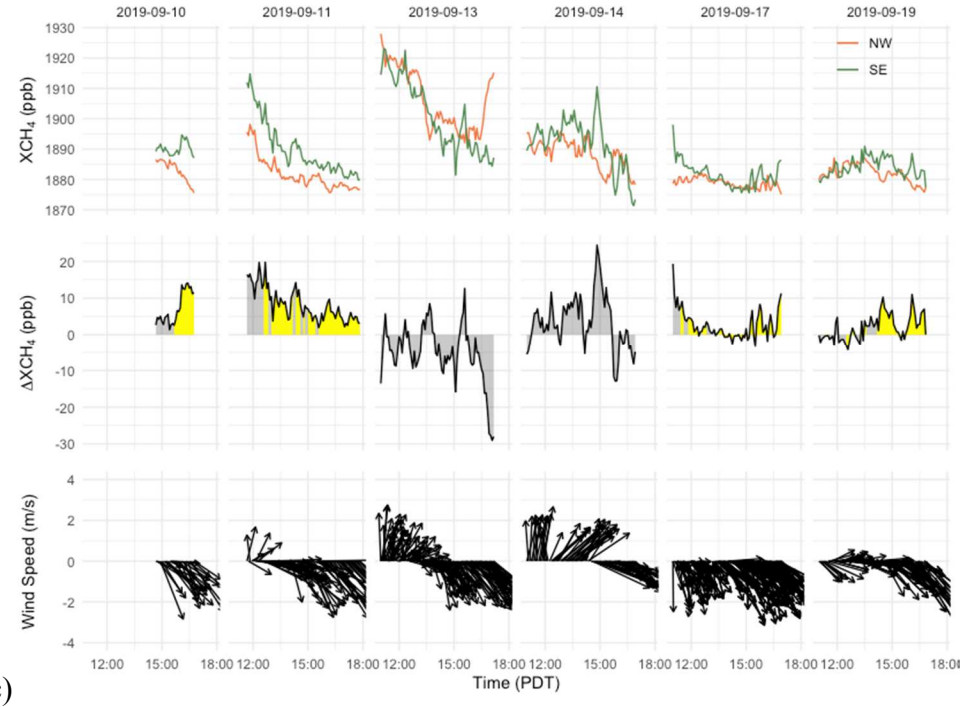
2019-09-10
2019-09-11
2019-09-13
2019-09-14
2019-09-17
2019-09-19
NW
SE
XCH4 (ppb)
ΔXCH4 (ppb)
Wind Speed (m/s)
12:00
15:00
18:00
Time (PDT)

c)

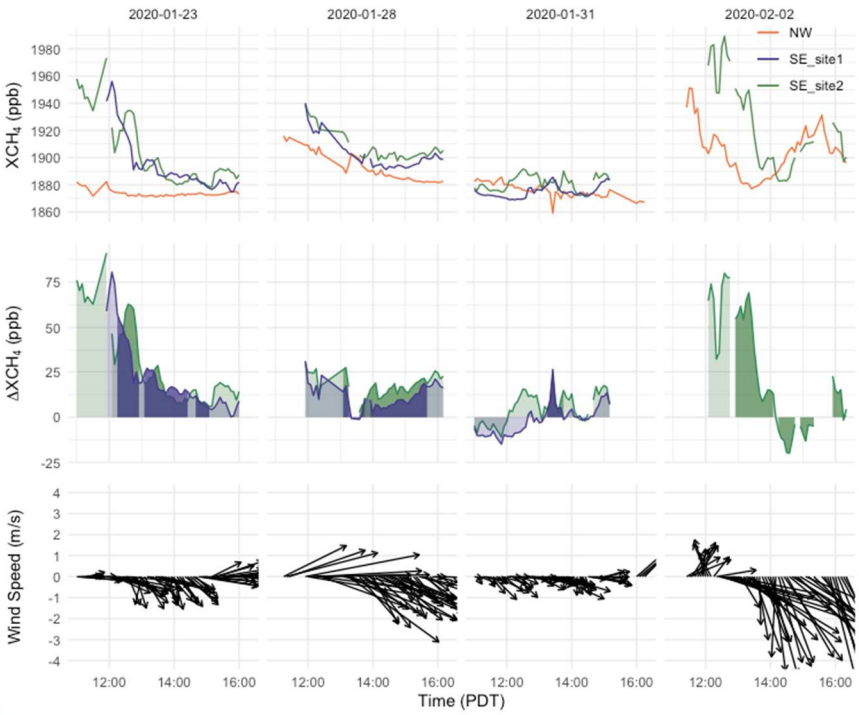

d)

Figure 2.3. Column-averaged X_{CH4} measured at sites NW and SE of the dairy cluster, SE – NW column differences (ΔX_{CH4}) and wind vectors averaged every 5 minutes for a) March 2019, b) June 2019, c) September 2019, and d) January 2020 seasons. Highlighted areas (yellow in March, June, September, and dark blue/green in January for the two instruments used) show time periods where all wind condition assumptions are met and used for estimating emissions. Negative values indicate winds were in opposite direction shifting the upwind and downwind locations.

2.3.2 Emission estimates of CH_4 from the dairy cluster

Using the mass balance approach, we computed emissions from the dairy cluster from ΔX_{CH4} measured when wind conditions meet the assumptions of the technique, namely, northwest winds above 1 m/s. We then compare observed emission rates to bottom-up (BU) emission estimates from dairy farms intersected by the five-minute averaged wind vectors where emissions are based on the number of cows, manure management practices, and state emission factors (Marklein et. al, 2021). We present this comparison as a scaling factor that informs us whether the calculated emissions are higher or lower than the bottom-up emissions. We calculated emission rates for each measurement day summarized in Figure 2.4. The mean daily emission estimates are reported for each measurement period with the standard error of the mean (i.e., 1-σ).

Emission estimates of CH_4 for each day ranged from 4.6 to 68.2 Gg CH_4/yr with a mean of 35.9 ± 19.8 (1SD). The seasonal mean estimates were 28.1 ± 2.5, 48.1 ± 2.5, 26.2 ± 6, 35.0 ± 3.4 for March, June, September, and January, respectively (Table 2.1). Comparing the different instrument configurations among sampling date, and hence sensitivity to different dairies, we then computed a scaling factor that is a ratio of calculated emissions divided by the bottom-up emission estimate from the same sources. The bottom-up (BU) emission estimates use the same five-minute averaged wind vectors intersecting dairy farms picked up by the measurements, with emissions estimates for these farms are based on the number of cows, manure management practices, and state regulatory emission factors (Marklein et. al, 2021). In January, two instruments were available to measure downwind of the dairy cluster at different sites (A and B) that had been measured in the

seasons prior. During northwest wind conditions, Configuration B was sensitive to more dairies than Configuration A. This was observed in the emissions estimate, but when compared to their respective bottom-up, the scaling factor agreed within error. We find that emission factors are uniform across the dairies with this approach, and although the two configurations are sensitive to different areas, and they give the same scaling it means the areas they are measuring are probably off from the prior in the same way.

Comparing the daily estimates to the bottom-up inventory, scaling factors had a mean of 1.9 ± 0.5, 3.7 ± 0.8, 1.6 ± 0.3, 2.6 ± 0.4 for March, June, September, and January, respectively (Table 2.1). The bottom-up prior does not consider seasonal differences, thus scaling factors are expected to reflect this. Scaling factors were larger than 1 in most cases. The range of measurements overlapped across most seasons, but emissions tended to be highest in summer with significantly lower emissions in fall (Figure 2.4b).

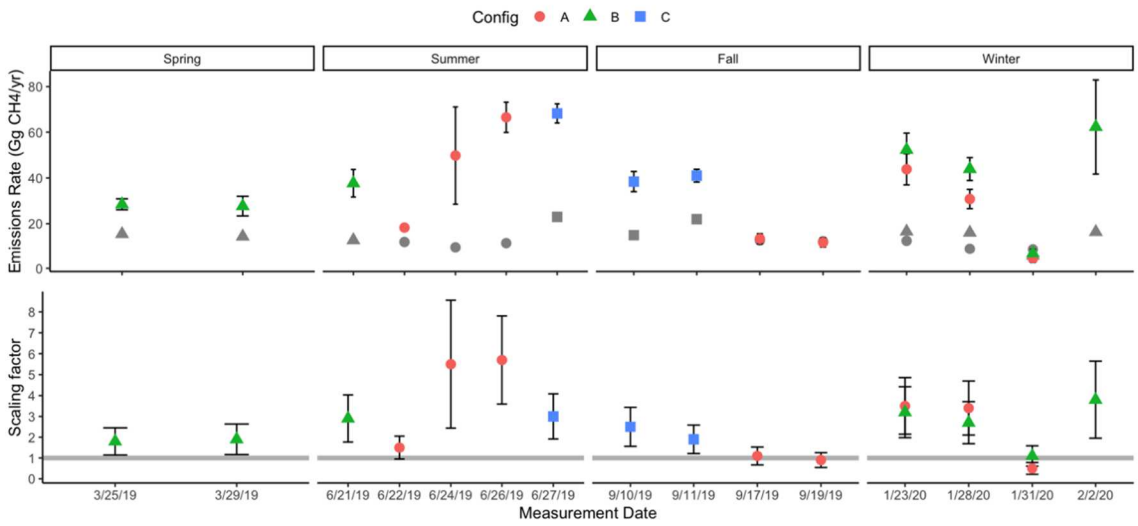

Figure 2.4 Estimated emission rate of CH_4 from dairy cluster using the mass balance approach. The points are colored by configuration. The grey color denotes the corresponding bottom-up estimate based on a dairy prior by Marklein et al 2021. The comparison between the observation-based estimates and the bottom-up estimates are shown as a scaling factor with 1:1 line in grey in the bottom panel.

Table 2.1. Summary of average seasonal mass balance emission rate estimates and the corresponding scaling factor after compared to bottom-up emissions summarized by season.

Season	Emission rate (Gg CH_4/yr)	Scaling factor
Spring	28.1 ± 2.5	1.9 ± 0.5
Summer	48.1 ± 2.5	3.7 ± 0.8
Fall	26.2 ± 6	1.6 ± 0.3
Winter	35.0 ± 3.4	2.6 ± 0.4

2.4 Discussion

2.4.1 Differential X_{CH4} measurements for emission estimates from dairy farms

Day-to-day variability was observed in the measured X_{CH4} from a dairy farm cluster with a strong dependance on wind conditions; a diurnal cycle was observed of winds shifting from southerly to northerly winds by midday. The shift in wind directions affected the magnitude of measurement signals and also determined what periods of stable wind conditions were appropriate to estimate emissions with the mass balance approach. Applying the differential column technique using only two instruments greatly reduces 25% of measurements we can use when data is filtered for wind directions to ensure the same air mass is measured by both instruments. This highlights the importance of gathering large number of measurements when applying simple mass balance models that rely on particular wind conditions due to loss of data from stringent filters. Filtering for ideal conditions, we were able to use a simple mass balance column model to estimate emissions from the dairy farms within the cluster.

Our measurement technique using ground-based remote sensing instruments measured a mix of dairy farm emissions coming from expected sources of CH_4, enteric fermentation and anaerobic manure lagoons. Roughly 50% of annual CH_4 emissions are expected from enteric fermentation while 50% is expected from manure management. Emissions of CH_4 at the farm scale are expected from the manure lagoons, settling basins, feed lots, and open lots where dairy cows reside. While our measurement technique does not differentiate between the different sources, we can estimate total emissions from farms within the cluster of interest. Due to the different downwind measurement location

(configuration A, B, or C) and the fact that wind direction was variable, we were not sensitive to the same dairies each day; however, we are able to compare our atmospheric-based emissions to a bottom-up inventory and across seasons, with the assumption that dairies in the cluster had similar management practices.

2.4.2 Seasonal trends follow temperature and manure volatile solid availability

We conducted seasonal measurements to estimate and determine the factors that influence dairy farm emissions in the SJV. Enteric fermentation emissions are largely driven by cow diet, which varies seasonally; however, these changes are small and not expected to yield a measurable difference in CH_4 emissions. In contrast, we expect seasonal changes in CH_4 emissions from the storage of liquid manure in anaerobic lagoons that are strongly dependent on volatile solid availability and lagoon temperature (Leytem et al., 2017; Mangino et al., 2001). We find that emissions from the dairy cluster were highest during the summer with 47.7 ± 2.5 Gg/yr whereas the lowest emitting season was fall with 26.2 ± 6 Gg/yr, through fall and spring were not statistically different. High summer emissions are consistent with the expectation of high temperatures driving the highest methane production rates, and low fall emissions are consistent with expected volatile solid availability, which reaches a minimum in fall due to substrate depletion following summer and annual lagoon cleanout. We find similar seasonal summer and winter patterns as Leytem et al. (2013) where CH_4 emissions from lagoons dairy farms in Idaho were measured over the course of one year. The authors found that the spring and summer had similar CH_4 emissions with equal contribution from open free stall area and wastewater ponds and lower emission in the fall and winter. They observed a 33-35% drop from

manure lagoons during the fall and winter seasons relative to spring and summer. We find a 45% drop between summer and fall seasons from a mix of enteric fermentation and manure management. Assuming 50% of our CH_4 estimates are from manure management, we expect a 23% drop from manure management. Winter is expected to have smaller emissions due to manure lagoon cleanout in September, however our observations match the same pattern that Jeong et. al, 2016 described in their SJV study.

2.4.3 Seasonal emission trends correlate stronger with wind speed

While temperature and manure volatile solid availability are thought to be the main drivers of CH_4 emissions from manure management, other studies have observed that higher wind speeds have increased the rate of evasion of CH_4 from lagoon surfaces (e.g., Leytem et al. 2016). Observations were collected during ambient temperatures ranging from 12.4 to 36.1°C and wind speeds from 1 to 9 m/s throughout the different seasons. The daily emission estimates and scaling factors had no correlation with temperature but showed a strong correlation with wind speed (Figure 2.6). The dataset of 5-min emission estimates (Figure 2.5) had very little relationship between CH_4 emissions and wind speed (R^2 = <0.01; P = 0.01) and no relationship between CH_4 emissions and air temperature (R^2 = <0.01; P = 0.86). Linear regressions of meteorological variables and averaged emission estimates of CH_4 reveal weak correlations with wind speed and air temperature (Figures 2.5 and 2.6). Although we expected temperature to be the dominant driver of emissions from dairy farms (Mangino et al., 2001), these results demonstrate that other variables are important such as wind speeds and farm level activities. Summer emissions have been

observed to be highest at dairy farms in other studies (Arndt et al., 2018; Leytem et al., 2017). However, studies (Heerah et al., 2021; Leytem et al., 2013) have noted the importance of other factors may influence emissions like wind speed, rainfall and volatile solid availability. Precipitation increases turbulent mixing of the lagoon surface and can add additional manure wastewater to lagoon in open dairies (Carranza et. al, In Prep). Interestingly, analyzing by season we find a negative relationship between emissions and air temperature in the winter ($R^2 = 0.35$; $P < 0.001$) and summer ($R^2 = 0.04$; $P < 0.001$). This negative relationship is opposite of what was expected since increased lagoon temperatures affect manure decomposition and consequently CH_4 emissions. On the contrary, we found a stronger correlation between wind speeds and emissions for spring ($R^2 = 0.33$; $P < 0.001$) and Fall ($R^2 = 0.11$; $P < 0.001$). A diurnal dependence on wind speeds and temperature were also observed in Leytem et al. (2013) from on-farm measurements. We find that day-to-day variability in measured X_{CH4} is influenced by both winds and temperature, but wind speeds drive the differences across seasons more than temperature. The fact that the temperature and wind are positively correlated with temperature across the seasonal scales, but not the within the season, suggests that on longer-term time scales (e.g. monthly) temperature is a factor in the emissions but that at short time scales there are other factors that are more important.

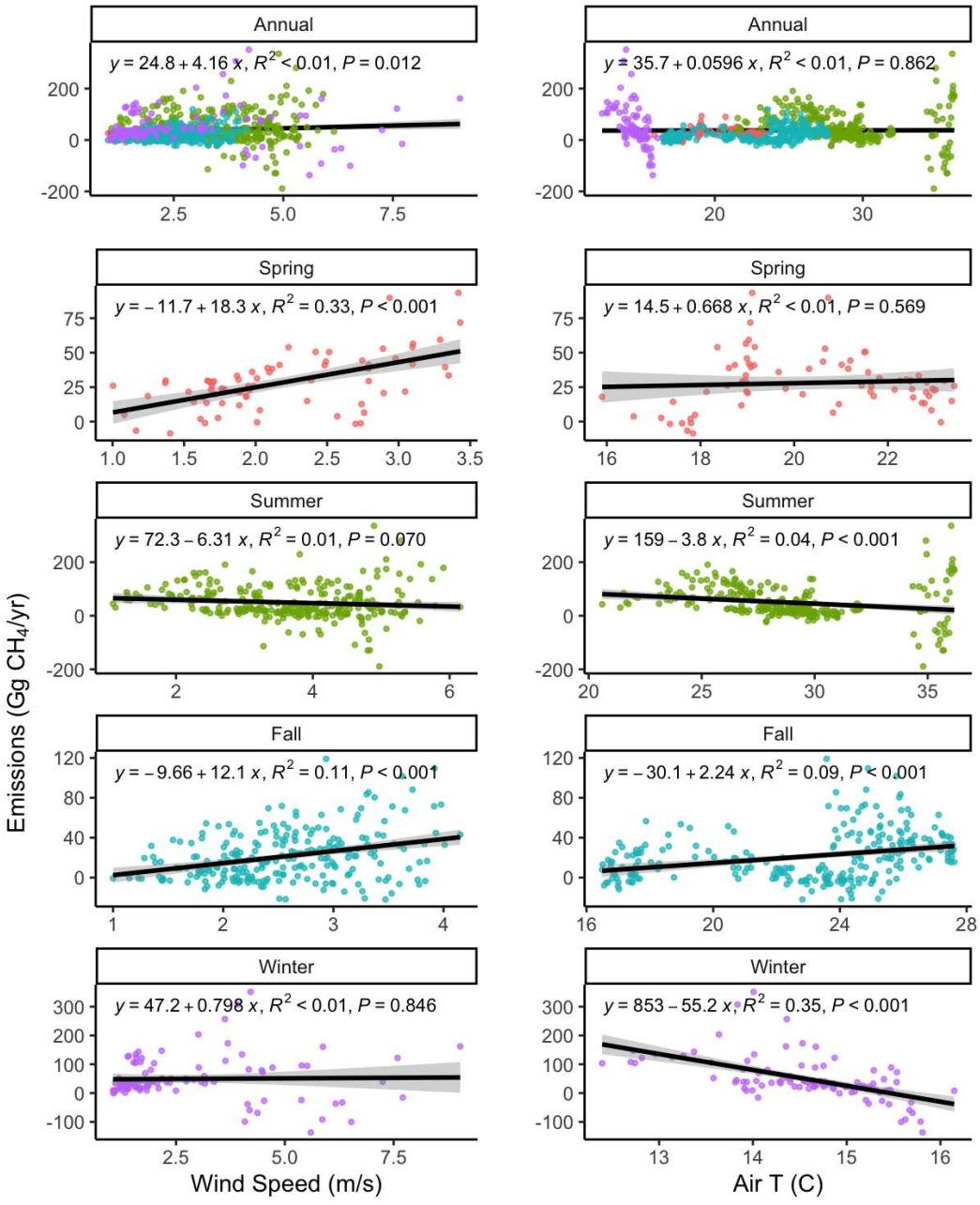

Figure 2.5. Linear regressions of 5-min emission estimates of CH_4 with wind speed and air temperature.

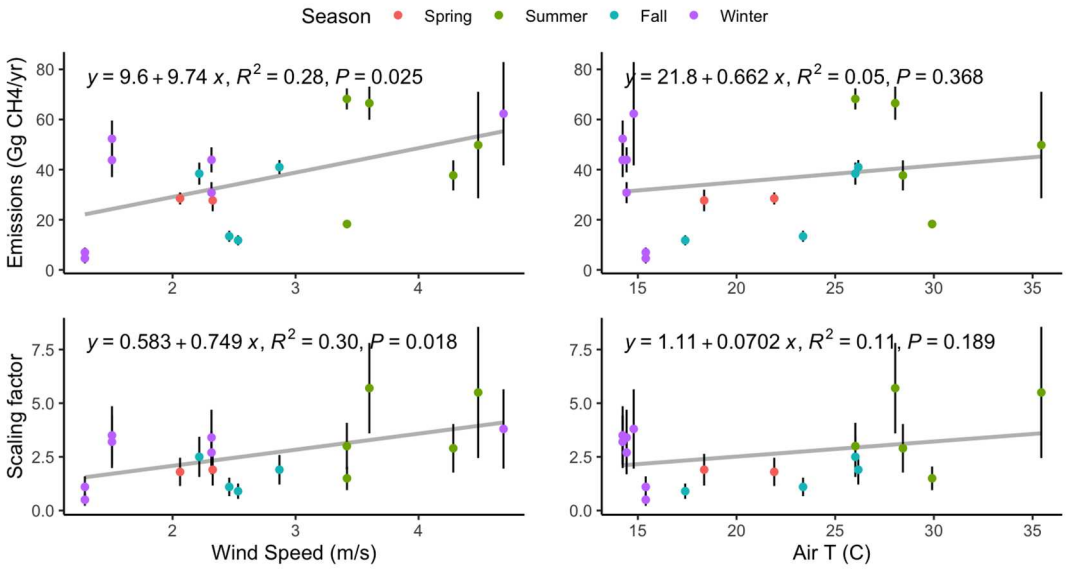

Figure 2.6. Linear regressions of daily emission estimates of CH_4 and corresponding scaling factors with wind speed and air temperature.

2.4.4 Comparison of emission factors for dairy cows in the SJV and Southern California

We compared our results with emission estimates measured with EM27/SUN solar spectrometers to the dairy farms in Southern California measured by Chen et al., (2016). Chen et al. (2016) measured a gradient of ~10 ppb during low wind speed conditions (~2 m/s) over a similar area of dairy farms (6 x 9 km^2) and estimated between 22.5 to 25.5 Gg (± 26%) CH_4/yr from the dairy source. We targeted ~40 dairies housing more than 30,500 cows while the Chino study targeted over 90 dairies housing 115,000 cows (Viatte et al., 2017). Our annual mean estimate from the 8 x 10 km^2 area of dairy farms is 35.9 ± 19.8 (1SD) Gg CH_4/yr. Although we targeted fewer dairy farms with less cows overall, our estimates from the SJV dairy farms are greater than dairy farms in the Chino dairies. Comparing our estimates per cow head, SJV cows emit ~5 times more CH_4 than Chino

cows. This highlights the magnitude of CH_4 emissions emitted by SJV dairy farms and the differences in managing animal waste. At the Chino dairies, open lot style is predominant, and a mix of wet and dry manure management is practiced. Dry manure management is expected to produce less CH_4 than the flushing of animal waste to manure lagoons. This demonstrates that wet manure management practices emit significantly more CH_4 than dry manure management, and the differential column technique is able to detect differences of this magnitude.

2.4.5 Differential column measurements to verify success of CH_4 mitigation

As the state of California invests in technology to mitigate emissions from dairy farms in the form of mechanical separators and anaerobic digesters, monitoring will become important to determine how effective these mitigation strategies are in reducing emissions of CH_4. The question remains of which measurement technique will be most adequate in assessing potential emissions reductions in the atmosphere. Different techniques such as in situ, mobile, eddy co-variance and tower-based measurements have been used to determine emissions from dairy farm at a variety of spatial scales from on-farm sources ($<1km^2$), whole facility ($1km^2$), local (10 km^2) and regionally (100 km^2). Within the cluster of dairies six of them are in the process of installing or are scheduled to install a digester. We estimated the effects of the 6 digesters installed in this cluster at the local scale and determined whether this technique will be able to detect reductions in emissions. Like in Marklein et al. (2021) following the USEPA, we assume a 75% efficiency in anaerobic digesters. We predict a total reduction of CH_4 emissions by 3.29

Gg CH_4/yr. Marklein et al. (2021) predicts that statewide manure emissions will be reduced by 26% from the implementation of mechanical separators and anaerobic digesters. Given the variability in estimated emissions measured by the solar spectrometer, this technique would not be adequate for capturing reductions from digesters at local scales and reductions would likely fall within the expected error.

2.4.6 Limitations to EM27/SUN differential CH_4 column technique

Our estimates of CH_4 in the SJV are based on daytime measurements during a limited number of days throughout the year. Solar column measurements are limited to daytime hours as the instrument requires the sun as the light source. For this reason, we were not able to capture nighttime emissions. As shown in Arndt et al. (2018), there are diurnal fluctuations in emissions from animal feeding throughout the day and lower nighttime emissions mainly due to less enteric fermentation from animals. Additionally, measurements were not continuous and only gathered a limited amount of 4-6 days per season. Unless instruments are secured properly as they have been done in long term network studies, measurements require a research team at two stations. Although a larger network of instruments would have been preferred, instrument availability was limited to two instruments that were used during most seasons except in January when three were available. For accurate measurement of emission reductions, more robust, continuously monitoring stations should be installed.

2.5 Conclusions

We have shown that X_{CH4} measurements using ground-based remote sensing paired with a mass balance model can be used to estimate emissions of CH_4. Our findings show

that CH_4 emissions from the dairy cluster were highest during the summer with 47.7 ± 2.5 Gg/yr whereas the lowest emitting seasons were fall and spring with 26.2 ± 6 Gg/yr and 28.1 ± 2.5, respectively. We find seasonal patterns consistent with Leytem et al. 2013 and Jeong et al 2016. These results demonstrate that other variables are important such as wind speeds and farm level activities and that on longer-term time scales (e.g. monthly) temperature is a factor in the emissions but that at short time scales there are other factors that are more important. This study contributes to the growing literature of work dedicated to understanding the distribution and processing controlling emission of CH_4. Future work can involve long term monitoring stations with their locations optimized to capture emissions year-round in order to accurately investigate the dominant processes that control short- and long-term changes over the year.

2.6 Acknowledgements

The authors thank Jonathon Franklin and Steve Wofsy at Harvard University and Greg Osterman at the NASA Jet Propulsion Laboratory for lending two of the EM27/SUN instruments used for the study. James Podolske at NASA Armstrong for help with the side-by-sides calibration measurements. Michael Rodriguez, Cindy Yañez, Dulce Frausto, Michelle Carr, Alondra Moreno, Nicole Jacobs, and Celia Limon for assisting in data collection. Authors would also like to thank Isaac Lino for building the cooling enclosure. We would also like to thank our funding source the University of California Office of the President Lab Fees Research Program (award LFR-18-548581) & National Science Foundation Graduate Research Fellowship Program to IFV. Work at Lawrence Berkeley National Laboratory was partially supported by Contractor Supporting Research (CSR)

funding from Berkeley Lab, provided by the Director, Office of Science, U.S. Department of Energy, under Contract No.DE-AC02-05CH11231.

2.7 References

Arndt, C., Leytem, A. B., Hristov, A. N., Zavala-Araiza, D., Cativiela, J. P., Conley, S., et al. (2018). Short-term methane emissions from 2 dairy farms in California estimated by different measurement techniques and US Environmental Protection Agency inventory methodology: A case study. *Journal of Dairy Science*, *101*(12), 11461–11479. https://doi.org/10.3168/jds.2017-13881

CARB. (2020). *California Greenhouse Gas Emissions for 2000 to 2018 Trends of Emissions and Other Indicators*. Retrieved from https://ww3.arb.ca.gov/cc/inventory/pubs/reports/2000_2018/ghg_inventory_trends_00-18.pdf

CARB. (2019). Methane (CH4). Retrieved November 25, 2020, from https://ww3.arb.ca.gov/cc/inventory/background/ch4.htm

Chen, J., Viatte, C., Hedelius, J. K., Jones, T., Franklin, J. E., Parker, H., et al. (2016). Differential column measurements using compact solar-tracking spectrometers. *Atmospheric Chemistry and Physics*, *16*(13), 8479–8498. https://doi.org/10.5194/acp-16-8479-2016

Cui, Y. Y., Brioude, J., Angevine, W. M., Peischl, J., McKeen, S. A., Kim, S.-W., et al. (2017). Top-down estimate of methane emissions in California using a mesoscale inverse modeling technique: The San Joaquin Valley: Methane Emission Estimates in SJV of CA. *Journal of Geophysical Research: Atmospheres*, *122*(6), 3686–3699. https://doi.org/10.1002/2016JD026398

Cui, Y. Y., Vijayan, A., Falk, M., Hsu, Y.-K., Yin, D., Chen, X. M., et al. (2019). A Multiplatform Inversion Estimation of Statewide and Regional Methane Emissions in California during 2014–2016. *Environmental Science & Technology*, *53*(16), 9636–9645. https://doi.org/10.1021/acs.est.9b01769

Dietrich, F., Chen, J., Voggenreiter, B., Aigner, P., Nachtigall, N., & Reger, B. (2021). MUCCnet: Munich Urban Carbon Column network. *Atmospheric Measurement Techniques*, *14*(2), 1111–1126. https://doi.org/10.5194/amt-14-1111-2021

Frenzel, C. W. (1962). Diurnal Wind Variations in Central California. *Journal of Applied Meteorology and Climatology*, *1*(3), 405–412. https://doi.org/10.1175/1520-0450(1962)001<0405:DWVICC>2.0.CO;2

Gisi, M., Hase, F., Dohe, S., Blumenstock, T., Simon, A., & Keens, A. (2012). XCO2 measurements with a tabletop FTS using solar absorption spectroscopy. *Atmospheric Measurement Techniques*, *5*(11), 2969–2980. https://doi.org/10.5194/amt-5-2969-2012

Hedelius, J. K., Viatte, C., Wunch, D., Roehl, C. M., Toon, G. C., Chen, J., et al. (2016). Assessment of errors and biases in retrievals of XCO2, XCH4, XCO, and XN2O from a 0.5 cm−1 resolution solar-viewing spectrometer. *Atmos. Meas. Tech.*, 20.

Heerah, S., Frausto-Vicencio, I., Jeong, S., Marklein, A. R., Ding, Y., Meyer, A. G., et al. (2021). Dairy Methane Emissions in California's San Joaquin Valley Inferred With Ground-Based Remote Sensing Observations in the Summer and Winter. *Journal of Geophysical Research: Atmospheres*, *126*(24). https://doi.org/10.1029/2021JD034785

IPCC. (2014). *Climate Change 2014: Mitigation of Climate Change. Working Group III Contribution to the Fifth Assessment Report of the Intergovernmental Panel on Climate Change*. (O. Edenhofer, R. Pichis-Madruga, Y. Sokona, E. Farahani, S. Kadner, A. Seyboth, et al., Eds.). New York, NY: Cambridge University Press.

Jackson, R. B., Saunois, M., Bousquet, P., Canadell, J. G., Poulter, B., Stavert, A. R., et al. (2020). Increasing anthropogenic methane emissions arise equally from agricultural and fossil fuel sources. *Environmental Research Letters*, *15*(7), 071002. https://doi.org/10.1088/1748-9326/ab9ed2

Jacobs, N., Simpson, W. R., Wunch, D., O'Dell, C. W., Osterman, G. B., Hase, F., et al. (2020). Quality controls, bias, and seasonality of CO2 columns in the boreal forest with Orbiting Carbon Observatory-2, Total Carbon Column Observing Network, and EM27/SUN measurements. *Atmospheric Measurement Techniques*, *13*(9), 5033–5063. https://doi.org/10.5194/amt-13-5033-2020

Jeong, S., Newman, S., Zhang, J., Andrews, A. E., Bianco, L., Bagley, J., et al. (2016). Estimating methane emissions in California's urban and rural regions using multitower observations. *Journal of Geophysical Research: Atmospheres*, *121*(21), 13,031-13,049. https://doi.org/10.1002/2016JD025404

Jones, T. S., Franklin, J. E., Chen, J., Dietrich, F., Hajny, K. D., Paetzold, J. C., et al. (2021). Assessing Urban Methane Emissions using Column Observing Portable FTIR Spectrometers and a Novel Bayesian Inversion Framework. *Atmospheric Chemistry and Physics Discussions*, 1–30. https://doi.org/10.5194/acp-2020-1262

Kalnay, E., Kanamitsu, M., Kistler, R., Collins, W., Deaven, D., Gandin, L., et al. (1996). The NCEP/NCAR 40-Year Reanalysis Project. *Bulletin of the American Meteorological Society*, *77*(3), 437–472. https://doi.org/10.1175/1520-0477(1996)077<0437:TNYRP>2.0.CO;2

Leytem, Dungan, R. S., Bjorneberg, D. L., & Koehn, A. C. (2013). Greenhouse Gas and Ammonia Emissions from an Open-Freestall Dairy in Southern Idaho. *Journal of Environmental Quality*, *42*(1), 10–20. https://doi.org/10.2134/jeq2012.0106

Leytem, Bjorneberg, D. L., Koehn, A. C., Moraes, L. E., Kebreab, E., & Dungan, R. S. (2017). Methane emissions from dairy lagoons in the western United States. *Journal of Dairy Science*, *100*(8), 6785–6803. https://doi.org/10.3168/jds.2017-12777

Makarova, M. V., Ionov, D. V., Foka, S. C., Blumenstock, T., Warneke, T., Virolainen, Y. A., et al. (2020). Emission Monitoring Mobile Experiment (EMME): an overview and first results of the St. Petersburg megacity campaign-2019, 45.

Mangino, J., Bartram, D., & Brazy, A. (2001). Development of a Methane Conversion Factor to Estimate Emissions from Animal Waste Lagoons, 15.

Marklein, A. R., Meyer, D., Fischer, M. L., Jeong, S., Rafiq, T., Carr, M., & Hopkins, F. M. (2021). Facility-scale inventory of dairy methane emissions in California: implications for mitigation. *Earth System Science Data*, *13*(3), 1151–1166. https://doi.org/10.5194/essd-13-1151-2021

Meyer, D., Price, P. L., Rossow, H. A., Silva-del-Rio, N., Karle, B. M., Robinson, P. H., et al. (2011). Survey of dairy housing and manure management practices in California. *Journal of Dairy Science*, *94*(9), 4744–4750. https://doi.org/10.3168/jds.2010-3761

Miller, S. M., Wofsy, S. C., Michalak, A. M., Kort, E. A., Andrews, A. E., Biraud, S. C., et al. (2013). Anthropogenic emissions of methane in the United States. *Proceedings of the National Academy of Sciences*, *110*(50), 20018–20022. https://doi.org/10.1073/pnas.1314392110

Moraes, L. E., Strathe, A. B., Fadel, J. G., Casper, D. P., & Kebreab, E. (2014). Prediction of enteric methane emissions from cattle. *Global Change Biology*, *20*(7), 2140–2148. https://doi.org/10.1111/gcb.12471

Saunois, M., Stavert, A. R., Poulter, B., Bousquet, P., Canadell, J. G., Jackson, R. B., et al. (2020). The Global Methane Budget 2000–2017. *Earth System Science Data*, *12*(3), 1561–1623. https://doi.org/10.5194/essd-12-1561-2020

Trousdell, J. F., Conley, S. A., Post, A., & Faloona, I. C. (2016). Observing entrainment mixing, photochemical ozone production, and regional methane emissions by aircraft using a simple mixed-layer framework. *Atmospheric Chemistry and Physics*, *16*(24), 15433–15450. https://doi.org/10.5194/acp-16-15433-2016

UNEP. (2021). *Global Methane Assessment: Benefits and Costs of Mitigating Methane Emissions*. Retrieved from http://www.unep.org/resources/report/global-methane-assessment-benefits-and-costs-mitigating-methane-emissions

USDA. (2017). USDA - National Agricultural Statistics Service - 2017 Census of Agriculture - Volume 1, Chapter 2: County Level Data. Retrieved December 9, 2020, from

Viatte, C., Lauvaux, T., Hedelius, J. K., Parker, H., Chen, J., Jones, T., et al. (2017). Methane emissions from dairies in the Los Angeles Basin. *Atmospheric Chemistry and Physics*, *17*(12), 7509–7528. https://doi.org/10.5194/acp-17-7509-2017

Vogel, F. R., Frey, M., Staufer, J., Hase, F., Broquet, G., Xueref-Remy, I., et al. (2019). XCO2 in an emission hot-spot region: the COCCON Paris campaign 2015. *Atmospheric Chemistry and Physics*, *19*(5), 3271–3285. https://doi.org/10.5194/acp-19-3271-2019

Zhao, X., Marshall, J., Hachinger, S., Gerbig, C., Frey, M., Hase, F., & Chen, J. (2019). Analysis of total column CO2 and CH4 measurements in Berlin with WRF-GHG. *Atmos. Chem. Phys.*, 24.

Zhong, S., Whiteman, C. D., & Bian, X. (2004). Diurnal Evolution of Three-Dimensional Wind and Temperature Structure in California's Central Valley. *JOURNAL OF APPLIED METEOROLOGY*, *43*, 21.

Chapter 3: Ground solar absorption observations of total column CO, CO_2, CH_4, and aerosol optical depth from California's Sequoia Lightning Complex Fire: Emission factors and modified combustion efficiency at regional scales

This chapter is under review in:

Frausto-Vicencio, I., Heerah, S., Meyer, A. G., Parker, H. A., Dubey, M., and Hopkins, F. M.: Ground solar absorption observations of total column CO, CO2, CH4, and aerosol optical depth from California's Sequoia Lightning Complex Fire: Emission factors and modified combustion efficiency at large scales, Atmos. Chem. Phys. Discuss. [preprint], https://doi.org/10.5194/acp-2022-671, in review, 2022.

Abstract

With global wildfires becoming more widespread and severe, tracking their emissions of greenhouse gases and air pollutants is becoming increasingly important. Wildfire emissions have primarily been characterized by in situ laboratory, and field observations at fine scales. While this approach captures the mechanisms relating emissions to combustion phase and fuel properties, their evaluation on large scale plumes has been limited. In this study, we report remote observations of total column trace gases and aerosols in the 2020 wildfire season of smoke plumes from the Sierra Nevada of California with an EM27/SUN solar Fourier transform infrared (FTIR) spectrometer. We derive total column aerosol optical depth (AOD), emission factors (EF) and modified combustion efficiency (MCE) for these fires, and evaluate relationships between them based on combustion phase at large scales. We demonstrate that the EM27/SUN effectively detects changes of CO, CO_2 and CH_4 in the atmospheric column at ~10 km scales that are attributed to wildfire emissions. These observations are used to derive total column EF_{CO}

of 120.5 ± 12.2 and EF_{CH4} of 4.3 ± 0.8 for a large smoke plume event in mixed combustion phases. These values are consistent with in situ relationships measured in similar temperate coniferous forest wildfires. FTIR derived AOD was compared to a nearby AERONET station and observed ratios of AOD to averaged air mole fraction of CO (X_{CO}) were consistent with those previously observed from satellites. We also show that co-located X_{CO} observations from the TROPOMI satellite-based instrument are 9.7% higher than our EM27/SUN observations during the wildfire period. Finally, we put wildfire CH_4 emissions in context of the California state CH_4 budget and estimate that 213.7 ± 49.8 Gg CH_4 were emitted by large wildfires in California during 2020, about 13.6% of the total state CH_4 emissions in 2019. Our novel application of an EM27/SUN solar spectrometer to quantify wildfire emission ratios at large scales follows predictive relationships that are consistent with in situ studies, offering promise for extensive monitoring from ground networks and satellite remote sensing.

3.1 Introduction

Wildfires are a major source of air pollutants, including particulate matter (PM), carbon monoxide (CO), and greenhouse gases, primarily carbon dioxide (CO_2) and methane (CH_4) (Akagi et al., 2011; Wiedinmyer et al., 2011; Andreae, 2019). The high levels of PM and CO released from fires are dangerous to human health and degrade air quality on a local, regional, and global scale (Schneising et al., 2020; Aguilera et al., 2021). CO is an air toxic and is considered an indirect greenhouse gas as it is a major sink for the hydroxyl radical (OH), increasing the abundance of CH_4 through photochemical feedbacks (Li et al., 2018) and also produces ozone (O_3), a short-lived greenhouse gas. CO_2 and CH_4

are the dominant greenhouse gases and are responsible for most of the current anthropogenic climate change (IPCC, 2014). A majority of carbon emissions from wildfires are of CO_2, CO, and CH_4 (~95%) while the remainder are carbonaceous aerosols (~5%) (Sommers et al., 2014; Urbanski, 2014). Although emissions from fires are biogenic sources of CO_2, they are released rapidly compared to the slow timescales of carbon uptake required to grow vegetation fuels. Increased fire activity increases atmospheric CO_2 in the short term, and can locally alter the terrestrial carbon cycle balance by reducing photosynthetic CO_2 uptake under high levels of vegetation disturbance (CARB, 2018). While CO_2 losses can be estimated as a function of burned area and fuel consumption, emissions of CO, CH_4, and aerosols are more difficult to estimate because they vary greatly with fire conditions. As global wildfires become more widespread and severe, tracking emissions of greenhouse gases and air pollutants from smoke will become increasingly important for efforts to track emissions of greenhouse gases and understand the impacts of fire on the atmosphere (Aguilera et al., 2021; Wilmot et al., 2022).

Our understanding of the atmospheric impacts of increasing fire activity relies on accurate observations and process-based estimation of fire emissions that have been developed using in situ measurements (Urbanski, 2014). While several space-based instruments can retrieve and derive emissions of important trace gases globally, observations are limited by spatiotemporal coverage and focus on aerosol burden from smoke plumes with limited attention to trace gases, and a lack of integration of trace gases and aerosols. Ground-based solar spectrometers present a new technique to measure and understand fire emissions at regional scales, and temporally complement satellite

observations. Column measurements are insensitive to the planetary boundary layer growth and are less affected by nearby point sources than in situ measurements, making them a good candidate for regional-scale monitoring (Lindenmaier et al., 2014). The EM27/SUN is a ground-based remote sensing instrument that is relatively portable and robust for field deployments. These instruments are the basis for the ground-based network of FTIR COCCON (COllaborative Carbon Column Observing Network), which complements NDACC (Network for the Detection of Atmospheric Composition Change) and TCCON (Total Column Carbon Observing Network), two high resolution FTIR trace gas monitoring networks (Frey et al., 2019; Wunch et al., 2011; Toon et al., 2009; De Mazière et al., 2018).

Field-based measurements of biomass burning in temperate forests are limited and sparse (Burling et al., 2011; Urbanski, 2014), despite the increase in burning activity in the Western U.S. (Zhuang et al., 2021). The EM27/SUN provides vertically integrated column measurements of CH_4, CO_2, and CO which allows for calculating modified combustion efficiency (MCE) and emission factors (EF) in the total column of smoke plumes downwind of wildfires. MCE values give insight into the relative amounts of flaming and smoldering combustion of the fire. Pure flaming combustion has an MCE of 0.99, while the MCE for smoldering varies from 0.65 to 0.85. A value near 0.90 indicates equal contributions of flaming and smoldering combustion (Akagi et al., 2011). EF are defined as the mass of gas or aerosol emitted per dry biomass consumed and are critical inputs for models to accurately calculate emissions and construct wildfire inventories (Urbanski, 2014). Providing new EFs will help improve regional biomass burning estimates. Past

studies have derived atmospheric column-based EFs with respect to CO from wildfires using solar FTIR spectrometers (Kille et al., 2022; Paton-Walsh et al., 2005; Lutsch et al., 2020, 2016; Viatte et al., 2014, 2015). The observed small changes in CO_2 with respect to the large atmospheric background has limited previous FTIR-based studies in their ability to derive EFs with respect to CO_2. This has consequently inhibited the calculation of MCE. Here, we present the first EFs with respect to CO_2 and MCE for wildfires calculated by total-column FTIR.

During part of the 2020 wildfire season, we deployed the EM27/SUN in the SJV downwind of two major wildfires, the Creek Fire and Sequoia Lightning Fire (SQF) Complex, in the Sierra Nevada. We report $EF_{CO/CO2}$ and $EF_{CH4/CO2}$ from the SQF Complex, a mixed conifer forest wildfire in the Sierra Nevada, and follow the wildfire's combustion phases with MCE values. Furthermore, because ground-based column measurements operate on similar scales as satellites and regional atmospheric models (McKain et al., 2015), we compared EM27/SUN measurements with satellite greenhouse gas observations from TROPOMI collected during the fires. We quantify MCE, EF for CO_2 and CH_4, and AOD enhancements from the SQF using EM27, we compare CO retrievals to TROPOMI, we compare AOD retrieval to an AERONET site, and we put wildfire CH_4 emissions in context of the California state CH_4 budget. Our work demonstrates a novel application of the ground based EM27/SUN solar spectrometers in wildfire monitoring and contributes to the development of techniques for analyzing remotely sensed greenhouse gas measurements.

3.2 Data Sources and Methods

3.2.1 EM27/SUN Atmospheric Column Observations

We measured the column-averaged dry air mole fractions (X_{gas}) of CH_4, CO_2 and CO (X_{CH4}, X_{CO2}, and X_{CO}) in a location 60 km west of the SQF Complex (Castle and Shotgun fires) and 80 km southwest of the Creek wildfires in the Sierra Nevada, and southeast of major dairy farms in the SJV (Figure 3.1, panel a). The SQF Complex fires began on Aug. 19 after a dry thunderstorm and lightning event ignited the fires in the Sierra Nevada. By Sept. 12, the SQF Complex had grown to 283 km^2. The Creek fire began on the evening of Sept. 5 and upper-level high winds produced a pyro-cumulus cloud on Sept. 6 that reached an altitude over 15 km (Morris III and Dennis, 2020). Smoke filled the valley and smoky overcast skies remained in large parts of the SJV for the next two weeks as fires kept burning. In total, the SQF Complex consumed 686 km^2 and Creek consumed 1515 km^2, placing both these fires among the top 20 largest California wildfires (Morris III and Dennis, 2020).

The Bruker Optics EM27/SUN solar-viewing Fourier Transform Spectrometer owned by Los Alamos National Laboratory (LANL) collected continuous daytime column measurements in Farmersville, California (36.31, -119.19) from Sept. 8 until Oct. 17, 2020, for a total of 40 days of observations. The EM27/SUN solar spectrometer has been previously used to study emissions from urban and agriculture CH_4 and CO_2 sources (Chen et al., 2016; Viatte et al., 2017; Dietrich et al., 2021; Alberti et al., 2022a; Makarova et al., 2021; Heerah et al., 2021). The recent addition of a CO detector in Bruker's EM27/SUN Fourier Transform Infrared (FTIR) spectrometer increases the instrument's utility for

measuring combustion sources and as a validation tool for TROPOMI column X_{CO} as it covers the same spectral region (Hase et al., 2016). The EM27/SUN uses the sun as the light source which allows it to derive aerosol optical depth (AOD) as demonstrated by Barreto et al. (2020) at the TCCON FTIR and AERONET site at Izaña, Spain. In their study, TCCON spectra were degraded to the same resolution as the EM27/SUN (0.5 cm-1) and they concluded that EM27/SUN spectra would be able to effectively derive AOD. Following their approach, we derive AOD for the wildfire period from our measurements. Further details of the AOD calculation are found in Section 3.2.4.

EM27/SUN X_{gas} values were retrieved from unaveraged double sided interferograms using the I2S and GFIT (GGG2014 version; https://tccon-wiki.caltech.edu/) retrieval algorithms automated by the EGI processing suite (Hedelius et al., 2016). Surface pressure is required to retrieve dry air columns in GGG and we used Coastal Environmental Systems ZENO weather station to record surface pressure at our field site for retrievals. Retrievals also require atmospheric profiles of temperature, pressure, altitude and water and these profiles were extracted from NCEP/NCAR reanalysis product (Kalnay et al., 1996). We calibrated the EM27/SUN via co-located measurements alongside the IFS125, a high-spectral-resolution FTIR operated by TCCON at the California Institute of Technology (CIT), both before and after the collection periods to determine calibration factors (R_{gas}) assuming a linear model forced through the origin for each gas, e.g., $X_{TCCON} = X_{EM27} R_{gas}$ (Chen et al., 2016; Hedelius et al., 2016). The TCCON network sets the standard as the current state-of the art ground-based validation system for remote sensing and satellite-based observations of greenhouse gases (Wunch et al., 2011), and TCCON

observations are tied to the World Meteorological Organization (WMO) standard greenhouse gas scale. Co-locating the EM27/SUN and TCCON instruments ensures system stability of the EM27/SUN after transportation to field sites. Co-located measurements were performed on Sept. 2–3, 2020 and Oct. 30–Nov. 1, 2020. Results of the correction factors from the co-located measurements are shown in Table A2.1 of Appendix A2. The TCCON instrument also uses the GFIT retrieval algorithm with the same a priori profiles; however, due to different instrument spectral resolutions and averaging kernels, we correct for the differences between the EM27/SUN and TCCON instrument following Hedelius et al., 2016 (Equation A4) to adjust the EM27/SUN retrievals before comparing with TCCON and deriving calibration factors.

Prior to measurements in California, the EM27/SUN was stationed in Fairbanks, Alaska for several months. Given the different settings used with the CamTracker, the solar disk was not centered on the camera and this misalignment was found on Sept. 7. Based on co-located measurements with the CIT TCCON on Sept. 2 and 3, it was determined that the observations within the second detector of XCO were affected on the days prior when camera was misaligned (Sept. 2, 3, 6, and 7). For this reason, we report measurements of X_{CO}, X_{CO2} and X_{CH4} beginning on Sept. 8 and use the Oct. 30 – Nov. 1 co-located measurements for calculating correction factors. AOD was derived from micro windows within the first detector, thus calculations of AOD were not affected.

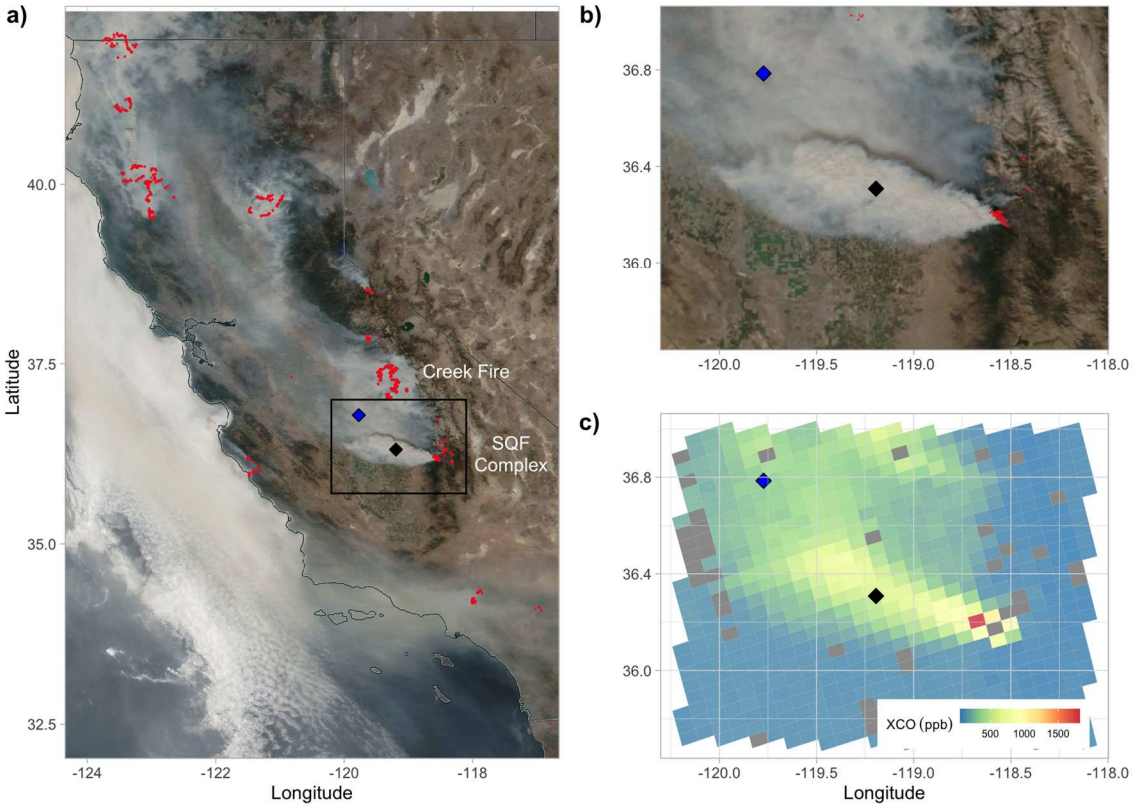

Figure 3.1. a) Satellite imagery captured by NOAA-20 VIIRS of heavy smoke in California on September 12, 2020, highlighting fire and thermal anomalies in red (NASA Worldview; worldview.earthdata.nasa.gov), and with black diamond shape showing the EM27 measurement location and blue diamond shape the AERONET observational site. b) Inset shows more detail of the smoke plume within the SJV from the SQF Complex in the Sierra Nevada, shown by red thermal anomalies at the right of the image. c) Inset of TROPOMI X_{CO} overpass at 2020-09-12 13:54 PDT.

3.2.2 TROPOMI Column Measurements

TROPOMI is an instrument launched in late 2017 onboard the European Space Agency's (ESA) Sentinel-5-Precursor (S5P). The instrument measures Earth radiance spectra in the ultraviolet (UV), NIR and SWIR allowing for measurements of a wide range of atmospheric trace gases and aerosol properties (Veefkind et al., 2012). The satellite has a sun-synchronous orbit with daily global coverage and a spatial resolution of 5.5 x 7 km^2 for CH_4 and CO operational level 2 (L2) products. The offline (OFFL) CO total column L2 data product filtered for quality assurance values > 0.5 are used in this work as recommended in the product readme file (https://sentinel.esa.int/documents/247904/3541451/Sentinel-5P-Carbon-Monoxide-Level-2-Product-Readme-File, last access: 4 Aug 2022). This selection filters out high solar zenith angles, any corrupted retrievals, and influences from high clouds. The majority of the TROPOMI X_{CH4} product was flagged out near the observational site during our measurement period, and hence was not included in this analysis. Following Sha et al., 2021, the TROPOMI CO column densities were converted to X_{CO} (ppb) by using the modeled surface pressure and total column of H_2O to calculate the column of dry air.

We evaluated the agreement between the retrieved X_{CO} from EM27/SUN and TROPOMI overpasses during the measurement period. This allows for a novel evaluation of the TROPOMI sensor under wildfire conditions of high X_{CO} and aerosol loading in the atmosphere. A correction factor was calculated to account for differences in the a priori profile used in the retrieval of X_{CO} in both instruments. We follow the a priori substitution method described in (Sha et al., 2021; Jacobs, 2021) to calculate an additive factor for the

EM27/SUN. Due to the possibility of measuring narrow smoke plumes on subgrid spatiotemporal scales, we perform a sensitivity study to determine the best co-location criteria for the EM27/SUN to TROPOMI comparison by varying the maximum radius (5 – 50 km) from the observational site and averaging time (5 – 30 min) for the EM27/SUN measurements around the TROPOMI overpass time. We require a minimum threshold of at least three 1-minute averages within the averaging time aggregations.

3.2.3 AERONET Data

AERONET (http://aeronet.gsfc.nasa.gov/ accessed on 15 June 2022) is a global network of sun/sky radiometer with over 600 sites operated around the globe. AERONET observations include measurements of aerosol optical depth, microphysical and radiative properties. The stations are frequently calibrated, and they set the standard for aerosol measurements and validation for satellite products. AERONET measures AOD at several spectral windows from 340, 380, 440, 500, 675, 870, 940, 1020 and 1640 nm. The Ångström exponent (AE), describing the wavelength dependence of aerosol optical thickness, is calculated from the spectral AOD. We used the AERONET Level 2.0 version 3 AOD and AE data from the Fresno_2 site (36.78, -119.77) that has been operating in the same location since 2012. This site is located about 90 km away from our EM27/SUN site. Further quality control information can be found in Giles et al., 2019.

3.2.4 AOD Calculation

To calculate AOD from the EM27/SUN solar measurements, we follow the methods described in Barreto et al. (2020) who found good agreement between AERONET

and TCCON FTIR-derived AOD at the high altitude Izaña Observatory in Spain. Their analysis was performed on degraded TCCON FTIR solar spectra (0.5 cm^{-1}) to assess the capability of lower resolution FTIR EM27/SUN instruments to detect aerosol broadband signal. A recommended ten interferogram scans were co-added to increase the signal to noise ratio for a total integration of 1 minute. We calculated AOD from four recommended micro windows with high solar transmission centered at 1020.9, 1238.25, 1558.25, and 1636 nm and compare to a nearby AERONET site located in Fresno, CA.

We apply the methods further described in Barreto et al. (2020) that are based on the Beer-Lambert-Bougher attenuation law:

$$V_\lambda = V_{o,\lambda} \cdot d^{-2} \cdot \exp(-m \cdot \tau_\lambda) \quad (1)$$

where V_λ is the measured solar irradiance at wavelength λ, $V_{o,\lambda}$ is the spectral irradiance outside the Earth's atmosphere at wavelength λ, d is the ratio of mean to actual sun-earth distance, and m is the optical air mass (Kasten and Young 1989). The V_o is derived from the Langley method by utilizing the measured solar intensity (V) versus the optical air mass (m) and extrapolating to an optical air mass of zero. The total optical depth (τ_λ) is the sum of the optical depth of Rayleigh scattering ($\tau_{R,\lambda}$), gas absorption ($\tau_{g,\lambda}$), and aerosols ($\tau_{a,\lambda}$):

$$\tau_\lambda = \tau_{R,\lambda} + \tau_{g,\lambda} + \tau_{a,\lambda}. \quad (2)$$

Barreto et al. (2020) carefully selected and evaluated several FTIR micro windows to minimize the gas absorption, thus $\tau_{g,\lambda}$ is considered negligible. Rayleigh scattering is calculated following Bodhaine et al. (1999) using the pressure measured at the

measurement site by the ZENO weather station. The AOD $\tau_{a,\lambda}$ can then be calculated by subtracting Rayleigh scattering from the equation below:

$$\tau_{a,\lambda} = \frac{\ln(V_{o,\lambda} \cdot d^{-2} \cdot) - \ln(V_{\lambda})}{m} - \tau_{R,\lambda} \, . \tag{3}$$

A cloud filter is applied to the spectra based on the measured fractional variation in solar intensity (fvsi). We set this quality filter to a maximum of 0.5% variability to ensure minimum cloud interference. The optical air mass range for Langley plot calibrations were performed from 1.5 > m > 7 to avoid large errors at smaller air masses and turbidity influence at solar noon. A plot of ln(Vo) is found in Appendix A2, Figure A2.1. displaying the calculated ln(Vo) over time from September to November 2020. Mirror degradation and exposure to dust or ash from fires can be observed in a declining ln(Vo) and a sudden jump in ln(Vo) is observed in late October and early November after the mirrors were cleaned, suggesting that debris had diminished the solar intensity measured by the FTIR instrument. Due to the varying ln(Vo), we calculate AOD only for the first week of data collection (Sept. 8 – 15) using the ln(Vo) obtained during the earlier period of September, summarized in Table A2.2 of Appendix A2.

A time series of the FTIR-derived AOD for the four micro windows is shown in Figure A2.2 of Appendix A2 where a spectral dependance of the aerosol absorption can be observed in the plot with longer wavelengths recording smaller AOD. Although our FTIR-derived AOD is limited to the spectral range from the FTIR detector (1020.9 – 1636 nm), we used the Ångström exponent to derive FTIR AOD at 500 nm to enable a comparison

with other studies shown in Figure 3.4. A plot of AOD at 1020.9 and 1636 nm with AERONET at 1020 and 1640 nm can be found in the Appendix A2, Figure A2.3.

3.2.5 Estimating Emission Factors and Modified Combustion Efficiency

We demonstrate the capability of ground-based solar column measurements to calculate important variables for fire research including EFs and MCE for determining fire emissions and understanding different combustion phases of wildfires. As a case study, Sept. 12 observations were selected as this day had the highest observed X_{CO} and dominant influence from the SQF Complex (Figure 3.1b). The SQF Complex was a lightning-sparked fire that began on Aug. 19, 2020, in the Sierra Nevada mixed conifer forest. We estimate emission ratios of CH_4 and CO ($ER_{CH4/CO2}$ and $ER_{CO/CO2}$) by calculating the slope from a York linear regression of CO and CH_4 excess mole fractions (ΔX_{CO} and ΔX_{CH4}) relative to CO_2.

$$ER_X = \frac{\Delta X}{\Delta CO_2} = \frac{X_{Fire} - X_{Background}}{CO_{2\,Fire} - CO_{2\,Background}}. \quad (4)$$

Emission factors ($EF_{CH4/CO2}$ and $EF_{CO/CO2}$) were then calculated as shown in equation 5 by multiplying the ER by the molar mass of either CO or CH_4 (MM_X), divided by the molar mass of carbon (MM_C), and total carbon emitted (C_T) while assuming 500 ± 50g C is emitted per kilogram of dry biomass consumed ($M_{Biomass}$) (Akagi et al., 2011; Burling et al., 2010). C_T is given by Equation 6, where n is the number of carbon-containing species measured, Nj is the number of carbon atoms in species j, and ΔCj is the excess mixing ratio of species j (Yokelson et al., 1999).

$$EF_X = \frac{ER_X}{C_T} * \frac{MM_X}{MM_C} * M_{Biomass} \quad (5)$$

$$C_T = \sum_{j=1}^{n} N_j \times \frac{\Delta C_j}{\Delta CO_2} \quad (6)$$

The MCE is commonly used as a relative measure between the smoldering and flaming combustion phases. Smoldering emissions have an MCE from 0.65-0.85, pure flaming emissions have an MCE of 0.99 and emissions near 0.9 have roughly equal amounts of flaming and smoldering combustion (Akagi et al., 2011). MCE was calculated by dividing excess mole fraction of CO_2 (ΔCO_2) by the total excess mole fraction of CO and CO_2:

$$MCE = \frac{\Delta CO_2}{\Delta CO + \Delta CO_2}. \quad (7)$$

Due to averaging kernel differences across the trace gases, an averaging kernel correction is applied to Equations 4 and 7, see Appendix 2.1. The enhancement over background mixing ratios (ΔX_{gas}) for each measurement day was calculated by subtracting the background ($X_{gas, bkdg}$) determined as the 2nd percentile of daily measured mixing ratios (X_{gas}). A sensitivity test showed that emission ratios did not significantly change if background was calculated using 1st-5th percentiles. The monthly background in September was 411.3 ppm for X_{CO2}, 99.4 ppb for X_{CO} and 1905.3 ppb for X_{CH4}. The monthly average mixing ratios measured in situ at Mauna Loa for CO_2 were 411.5 ± 0.2 ppm and CH_4 1884.7 ± 1 ppb during September 2020 (https://gml.noaa.gov/obop/mlo/).

3.3 Results

3.3.1 Observations X_{CO}, X_{CO2}, and X_{CH4} from wildfires in the San Joaquin Valley

The first week of trace gas measurements are shown in Figure 3.2 in addition to the daytime fire radiative power (FRP), an indicator of fire intensity measured by Visible Infrared Imaging Radiometer Suite (VIIRS) Active Fire and Thermal Anomalies product from NOAA-20. Fire-emitted CO can be observed in the timeseries and XCO is exceptionally high on Sept. 12, reaching mixing ratios 10 times higher than the previous days. A large smoke plume was captured by the NOAA VIIRS satellite on Sept. 12 originating from the SQF Complex and traveling west directly over the measurement site as seen in Figure 3.1b. Sept. 12 also corresponds to the highest FRP during this record. The next day, Sept. 13, both fires remained active; however, their smoke plumes were transported northward as reflected by a lower XCO in our observations relative to Sept. 12.

X_{CO2} and X_{CH4} were also enhanced on the Sept. 12 smoke event and followed the same trend as X_{CO} over the course of the day. Over 30 dairy farms are located northwest of the measurement site and they are expected to influence observed X_{CH4} and X_{CO2}; dairy influence is notable on days with predominantly westerly winds (e.g. Sept. 8 and 11). X_{CO}, X_{CO2}, and X_{CH4} averaged at 154 ± 78 ppb, 413 ± 1 ppm, and 1938 ± 27 ppb from Sept. 8 to Oct. 17. X_{CO} and X_{CO2} peaked on Sept. 12 at 1012.8 ppb and 421.6 ppm, while X_{CH4} peaked on Sept. 28 at 2050.1 ppm due to dairy farms in the area. The measured X_{CO} on Sept. 12, 2020, is the highest reported X_{CO} value in EM27/SUN literature. Retrievals of X_{gas} using the EM27 in such dense smoke plume has not been reported in previous studies. Using this date as a case study, we calculate total column EF and MCE to study the

evolution of the fire over the course of the day further described in Section 3.3.4. We isolate the Sept. 12 fire smoke plume by taking the X_{CO} mixing ratios that exceeded the 98th percentile (>335.1 ppb) from all observations over our measurement period. This period corresponded to mixing ratios recorded after 12:00 pm when X_{CO} and X_{CO2} began to increase considerably.

The time since emission of the observed smoke plume was estimated to be ~1.5 hr. This was calculated by dividing the distance away from the SQF Complex fire (~60 km) by the average wind speed (11.2 ± 0.8 m/s) at the height of the smoke plume (4.1 ± 1.2 km). The height of the plume was determined by taking a mean of the available pixels within the smoke plume of aerosol layer height product from TROPOMI (http://www.tropomi.eu/data-products/aerosol-layer-height). The mean wind speed measured at 4.1 ± 1.2 km came from a 915 MHz Wind Profiler located in Visalia, CA about 20 km west of the observational site (data available at: ftp://ftp1.psl.noaa.gov/psd2/data/realtime/Radar915/).

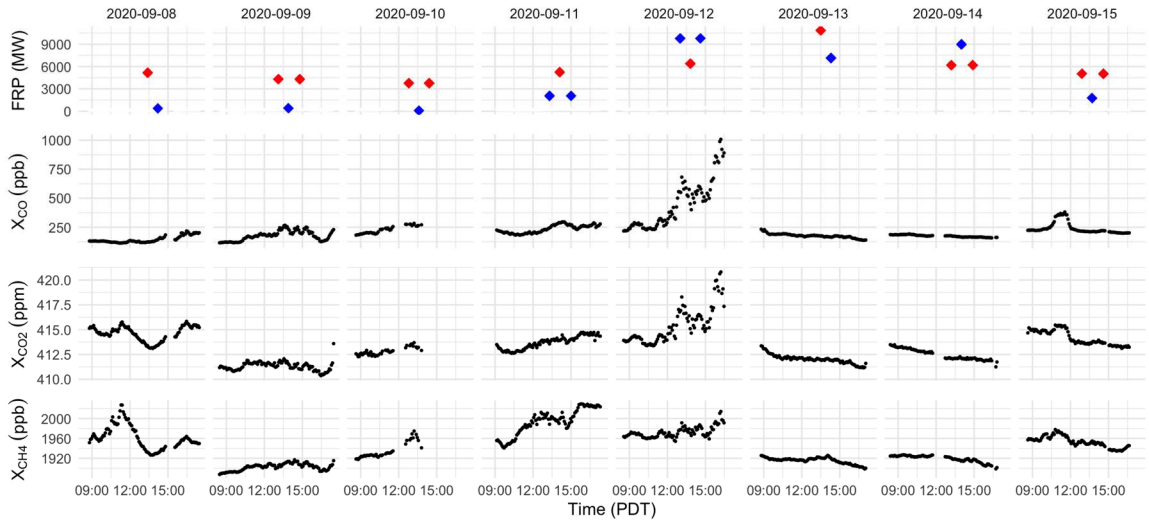

Figure 3.2. Timeseries of daytime FRP from VIIRS NOAA-20 of Creek fire (red) and SQF Complex (black) and of 5-minute mean observations from the ground-based EM27/SUN solar-viewing spectrometer during the first week of measurements September 8 – 15, 2020.

3.3.2 Comparison of EM27/SUN and TROPOMI Retrievals

In this section, we compare X_{CO} retrieved from ground-based EM27/SUN observations downwind of the Sierra Nevada wildfires to satellite-based X_{CO} retrievals from coincident TROPOMI overpasses. Previous studies of X_{CO} and X_{CH4} comparisons between TROPOMI and EM27/SUN's have used a TROPOMI soundings between 50 – 100 km from the observational site and used EM27/SUN measurements between 40 mins – 1 hour TROPOMI overpass as a coincident criteria (Sha et al., 2021; Jacobs, 2021; Sagar et al., 2022; Alberti et al., 2022b). Given the spatial and temporal heterogeneity in smoke plumes from wildfires observed in Figure 3.1 and Figure 3.2, we perform a sensitivity study of different radii (10, 15, 20, 30, 40, 50 km) from our observational site and time averages (10, 15, 20, 30 mins) to determine adequate criteria for comparison during a wildfire event. An illustration of the sensitivity analysis is shown in Figure A2.5, Appendix A2.

We quantify the sensitivity of different TROPOMI radii and averaging times in comparison with our EM27/SUN data by calculating the mean difference, mean relative difference and R^2 between the linear regression fits for the measurements. We find that all combinations produce a positive mean bias, meaning that TROPOMI overestimates X_{CO} compared to the EM27 measurements. TROPOMI pixels within a radius of 5 km averaged with 30-minute aggregations of EM27/SUN gives the lowest mean difference of 10.64 ppb, mean relative difference of 5.5%, and highest correlation coefficient of 0.99, however, only 4 points coincide during the measurement period. To maximize the number of coincidences while maintaining a low bias, we select 15 km as the maximum radius with a 30-minute averaging time. This gives a total of 19 coincident data points and mean difference of 17.2 ppb, mean relative difference of 9.7%, and R^2 of 0.97. A timeseries of the coinciding data pairs from the EM27/SUN 30-minute average observation period with TROPOMI overpass with 15 km radii are shown in Figure 3.3a and the correlations are shown in Figure 3.3b. Applying these spatial and temporal criteria results in large variance for the largest measured X_{CO} due to heterogeneity in the smoke plume event. The EM27/SUN displays a larger variance than TROPOMI due to capturing the 30-minute temporal variability in the plume as it was transported above the instrument. We find a strong correlation between CO column averages with an R^2 of 0.97 and a York linear regression fit of $y = 1.36x - 40.15$. These results suggest an overestimation of 9.7% X_{CO} from TROPOMI observations of wildfires.

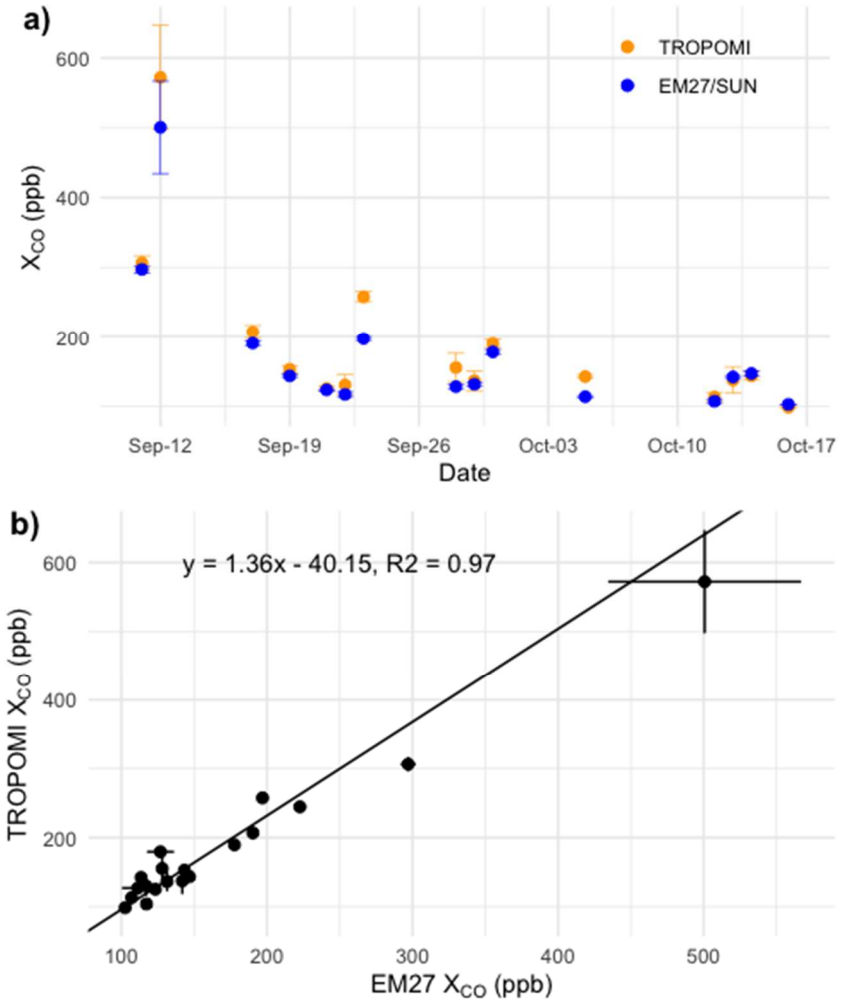

Figure 3.3. a) Timeseries of coinciding EM27/SUN 30-minute average observation period with TROPOMI overpass 15 km from observation site. b) Correlation between coinciding TROPOMI and EM27/SUN data pairs. The error bars are the standard deviation of the TROPOMI averaged pixels at 15 km and EM27/SUN 30-minute observation.

3.3.3 Aerosol optical depth derived from measured solar intensity

We show a timeseries of AOD at 500 nm derived for the first week of measurements in Figure 3.4 (Sept. 8 – 15) plotted with AOD at 500 nm from an AERONET station in Fresno (Sept. 4 – 19), about 90 km north of the measurement site (Figure 3.1). Similar to observations of X_{CO}, enhancements of AOD are observed through the week with the highest recorded AOD on Sept. 12. The observational sites were relatively far from each other (~90 km) and although smoke reaching the two sites varied over these spatial scales, the FTIR AOD follows the same inter-day trend as the AOD measured by the AERONET with a peak in AOD on the 12th. Intraday variability between the sites do not seem to follow the same trend. This suggests that the EM27/SUN AOD estimate was also able to qualitatively capture the increase in aerosols in the SJV as fires burned more intensely and smoke from fires moved into the valley due to synoptic conditions. Differences are observed in the AOD timeseries as these two sites were downwind of two different fires in the Sierra Nevada: the Creek Fire was located directly west of Fresno and the SQF Complex composed of the Castle and Shotgun fires was located directly west of the EM27/SUN measurement site. This may be the reason that the peaks observed at the FTIR site are not seen in the Fresno AERONET data. Ahangar et al. (2022) determined that the SJV air quality was mainly impacted during the Sept. 8 – 15 period with Creek and SQF Complex fires responsible for the majority of the smoke within SJV. Although the Creek fire began on Sept. 5, the air quality began to deteriorate a few days after, possibly due to the westerly downslope winds that pushed the smoke east of the Sierra Nevada at the beginning of the fire (Cho et al., 2022). Low AOD from AERONET was observed prior to

Sept. 8 with values of 0.50 ± 0.28, illustrating the air quality was cleaner and deteriorated after the activity from the Creek and SQF Complex fires increased (Ahangar et al., 2022).

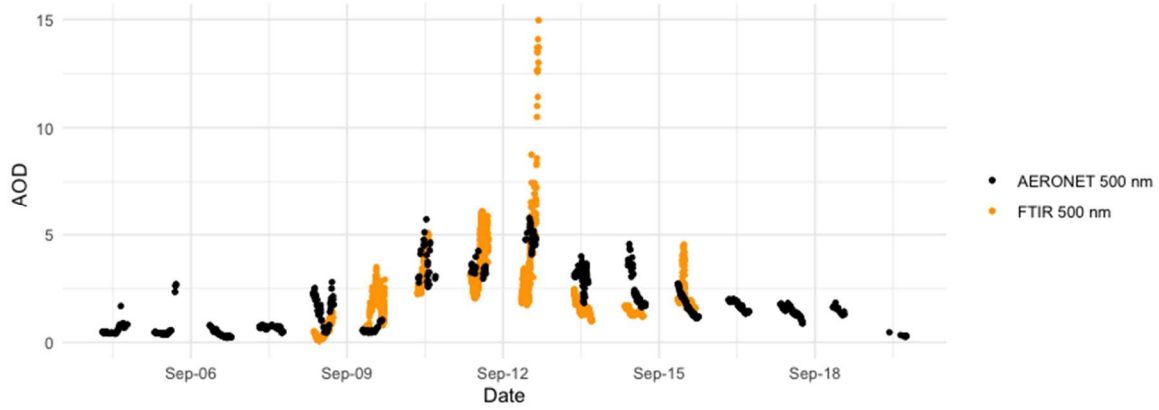

Figure 3.4. FTIR AOD and AERONET AOD at 500 nm. The FTIR AOD at this wavelength was calculated using the Ångström exponent relationship.

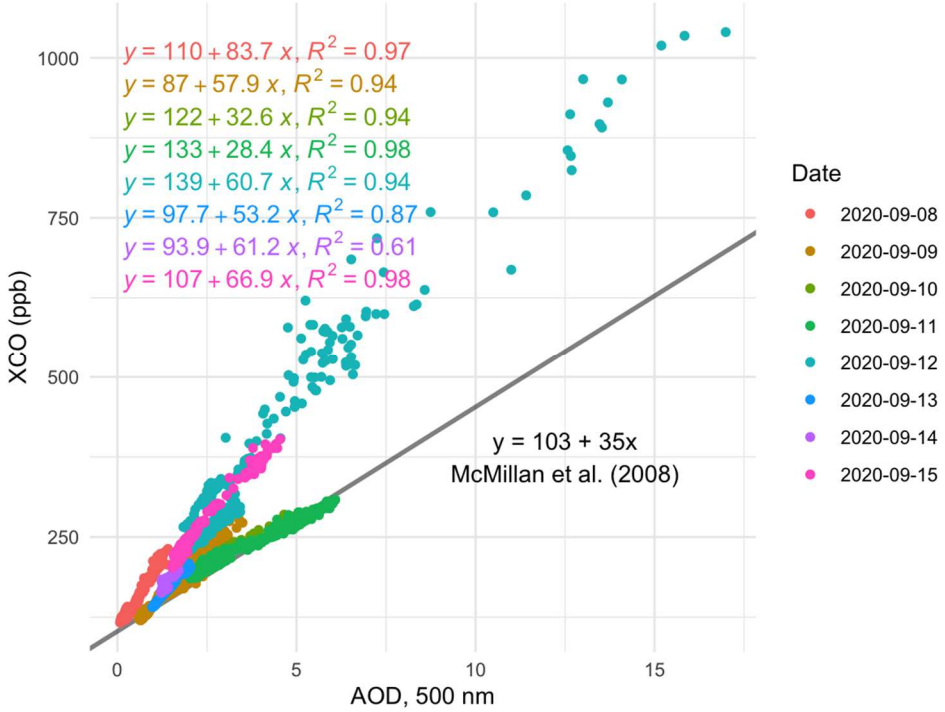

Figure 3.5. Scatterplot correlations of X_{CO} and AOD at 500 nm from the FTIR for each day of the first week Sept. 8 -12. Low smoke days fall along the black line. The teal line corresponds to Sept. 12, the day of highest fire influence in our record.

3.3.4 Emission Factors and Modified Combustion Efficiency

The average MCE for the smoke plume on Sept. 12 was 0.89 ± 0.21, meaning that observations of the smoke plume consisted of a mixture of flaming and smoldering combustion phases (Figure 3.6). During the flaming phase of a fire, CO_2 is produced, and convection is created by high flame temperatures and produces lofting of smoke. High altitude smoke can be transported large distances, corroborated by observations of ash falling from the sky at the measurement site ~60 km away from the fire and clearly observable by satellite imagery (Figure 3.1b). In contrast to the flaming phase, smoldering fires burn at lower intensity, and incomplete combustion side products like CO, CH_4, and organic carbon aerosol are produced. We observed a steady MCE as X_{CO}, X_{CH4}, and AOD increased, indicating influence of smoldering combustion (Figure 3.6, a-e). The MCE calculated from total column observations is averaged over the entire vertical plume as it was being transported over the measurement site. The advantage of a plume integrated MCE is that vegetation is burnt differently throughout the fire and the atmospheric column observations can represent the fire as a whole by integrating the smoke plume heterogeneity in the vertical atmospheric column.

Emission ratios of CO and CH_4 on Sept. 12 were calculated with respect to CO_2. $ER_{CO/CO2}$ was 0.116 and the $ER_{CH4/CO2}$ was 0.0073 (Figure 3.6, f-h), resulting in an EF_{CO2} of 1632.9 ± 163.3 g CO_2 per kg biomass combusted, EF_{CO} of 120.5 ± 12.2 g CO per kg biomass combusted, and a EF_{CH4} of 4.3 ± 0.8 g CH_4 per kg biomass combusted. We compared findings from our gas measurements to literature values in temperate coniferous forest studies from the Sierra Nevada and other locations in North America summarized in

Table 1 and Figure 3.7. All the studies listed in Table 1 except for this study were based on aircraft measurements. Most recently, Prichard et al. (2022) compiled emission factors for North American conifer forests and found a fire average for EF_{CO2} of 1629.54 ± 63.43, EF_{CO} of 104.01 ± 34.93, and EF_{CH4} of 5.05 ± 2.41. Burling et al. (2011) measured the Turtle Fire in the Sierra Nevada, and we find that our MCE overlaps within error with theirs. Finally, CH_4 emissions reported for more smoldering fires that were characterized by direct O_2/CO measurements for 1999 Big Bar fire (Lueker et al., 2001). Our atmospheric column-based EF fall within the ranges of previous literature, highlighting the ability of the EM27/SUN solar spectrometer observations to be used for deriving important variables for fire research.

Table 3.1. Summary of past airborne studies modified combustion efficiency (MCE) and emission factors (EF, g kg^{-1}) relative to CO_2 for temperate coniferous forests in North America and Sierra Nevada.

Studies	**MCE**	**EF CO_2**	**EF CO**	**EF CH_4**
North America				
Radke et al., 1991* – Conifer Forest	0.919	1641	93	3.03
Yokelson et al., 1999* – Southeastern US Pine Forest understory	0.926	1677	86	-
Yokelson et al., 2011 – Mexico Pine-oak	0.908	1603	103	3.66
Burling et al., 2011 –Average conifer forests understory burns*	0.936 ± 0.024	1668 ± 72	72 ± 26	3.0 ± 2.4
Urbanski et al., 2013 – Rocky Mts conifer forest fires	0.85 – 0.92	1527 – 1681	89.3 – 173	4.4 – 12.1
Liu et al., 2017 – Study average	0.912	1454 ± 78	89.3 ± 28.5	4.9 ± 1.5
Sierra Nevada				
Burling et al., 2011				
Turtle Fire* (10-Nov-2009)	0.913	1599	97	5.51
Shaver Fire* (10-Nov-2009)	0.885	1523	126	7.94
Yates et al., 2016				
Rim fire (26-Aug-13)	0.94	1675 ± 285	92.5 ± 16	4.8 ± 0.8
Rim fire (29-Aug-13)	0.94	1711 ± 292	69.5 ± 12	4.7 ± 0.8
Rim fire (10-Sept 13)	0.88	1595 ± 272	138.4 ± 24	7.5 ± 1.3
Liu et al., 2017				
Rim fire (26-Aug-13)	0.923	1478 ± 11	78.7 ± 4	4.43 ± 0.25
This study: SQF Complex fire+	**0.91 ± 0.01**	**1645.0 ± 164.5**	**111.0 ± 19.2**	**5.2 ± 1.1**

*Prescribed burns

+ Measurement uncertainties were calculated by propagating the error from the linear regression standard error, C_T, 10% error from $M_{Biomass}$, and biased introduced from difference in instrument averaging kernel (Appendix A2.1).

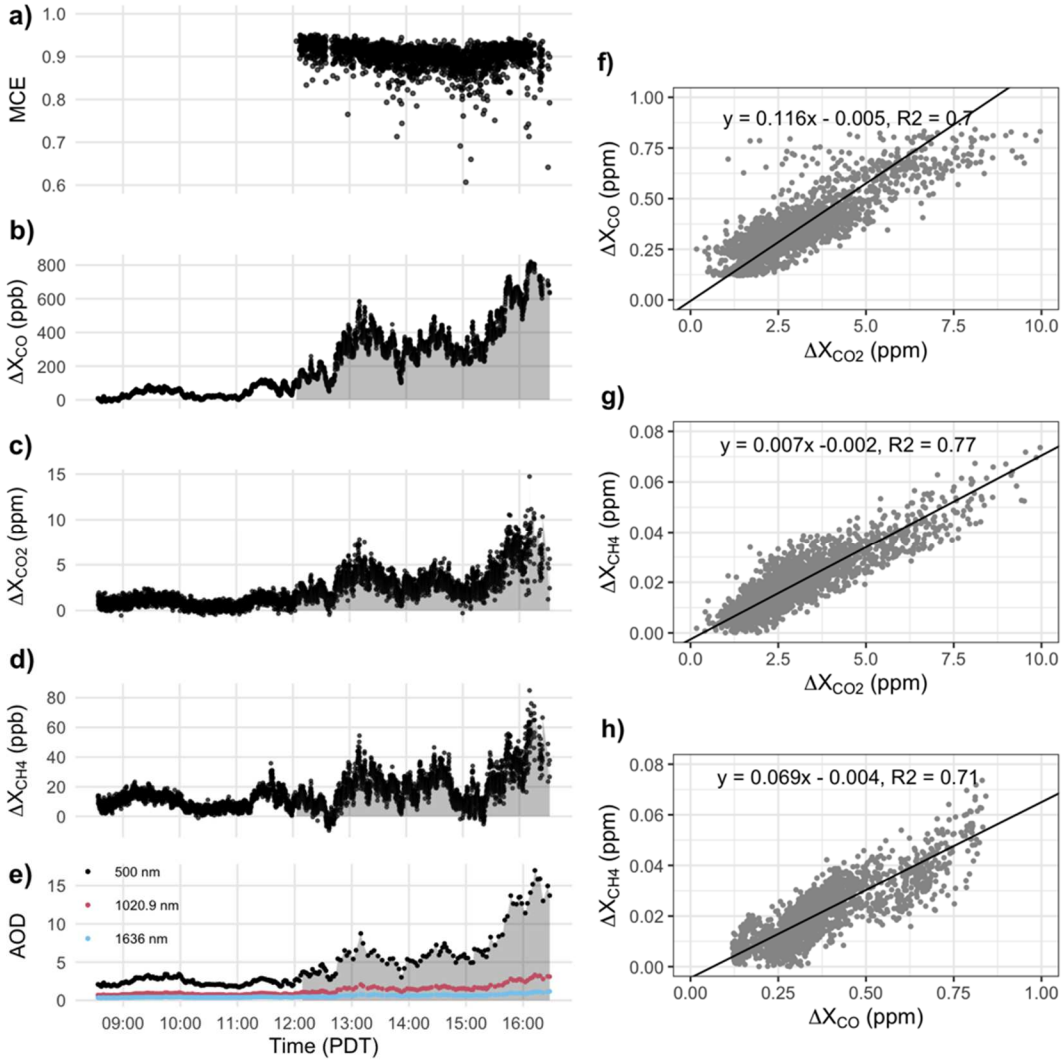

Figure 3.6. Timeseries of September 12, 2020 of a) MCE, b-d), shaded grey area represents the SQF Complex fire plume. d-g) linear regression plots of ΔCO and ΔCH_4 against ΔCO_2 to calculate the slope that represents the ER.

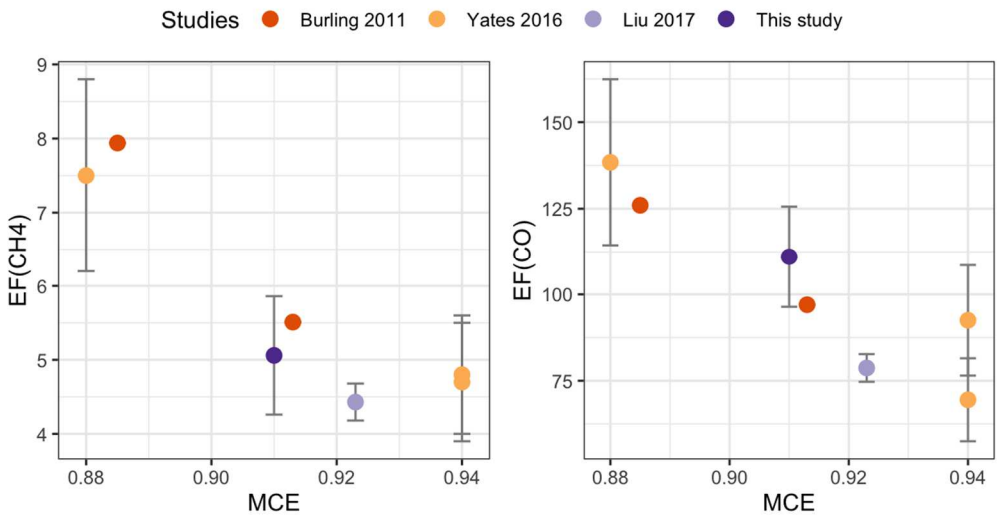

Figure 3.7. Emission factors (g kg^{-1}) as a function of MCE for temperate coniferous forests in Sierra Nevada wildfires.

3.3.5 Enhancement Ratios of SJV Greenhouse Sources

The EM27/SUN's location enabled us to sample transient fire plumes from local and state wildfires, but was also located near a large cluster of dairy farms, which are a large regional source of CH_4 emissions (Heerah et al., 2021; Marklein et al., 2021). Dairy farms are known to emit significant amounts of CH_4 from the animal's enteric fermentation and on-farm manure management. Because fires also emit CH_4, we explored whether dairy and fire sources in this region can be disentangled using ratios of the different species measured by the EM27/SUN. Furthermore, our measured X_{CH4} enhancement ratios relative to X_{CO2} enable us to investigate the contribution of state wildfires to CH_4 emissions in 2020. To constrain the observed enhancements, we compared the enhancement ratios of $\Delta X_{CH4}/\Delta X_{CO2}$ from September – October 2020 to enhancement ratios collected in September 2018 and 2019 in the same local area that characterize non-fire years. September 2018 and 2019 measurements are further described in the Appendix. We

focused on observation days with statistically significant correlations (n = 26 days) between CH^4 and CO^2 enhancements ($R^2 > 0.5$ and $p < 0.05$) to characterize enhancement ratios of the SJV non-fire years.

Figure 3.8 shows the $\Delta X_{CH4}/\Delta X_{CO2}$ enhancement ratios from September 2018, September 2019, and September – October 2020 measurements. We observe a clear influence of dairy farms with larger $\Delta X_{CH4}/\Delta X_{CO2}$ enhancement ratios of 38.4 ± 21.7 and 30.5 ± 5.0 (ppb/ppm), respectively for September 2018 and 2019, exceeding $\Delta X_{CH4}/\Delta X_{CO2}$ wildfire smoke periods. During our 2020 observations, $\Delta X_{CH4}/\Delta X_{CO2}$ reflecting dairy farm influence were found on some days in addition to less steep slopes from smoke influence. This is expected as elevated X_{CO2} and lower X_{CH4} are emitted from wildfires. The Sept. 12 smoke plume event is highlighted in the figure and has a smaller enhancement ratio of 7.3 (ppb/ppm) than dairy farms. Similar ratios of $\Delta X_{CH4}/\Delta X_{CO2}$ were found in Hanford, ~50 km west of our observation site, from an aircraft study ranging from 35.9 – 44.4 (ppb/ppm) during a winter campaign (Herrera et al., 2021). Other column-based studies have determined the X_{CH4}/X_{CO2} for urban sources in the Los Angeles City finding ratios for X_{CH4}/X_{CO2} ranging from 6.65 to 9.96 (ppb/ppm) in 2015 (Chen et al., 2016). Wunch et al., 2009 calculated X_{CH4}/X_{CO2} ratio of 11 ± 2 and showed that urban fossil fuel and wildfire X_{CH4}/X_{CO2} ratios are very similar due to incomplete combustion and ratios are not distinct enough to separate (Wunch et al., 2009). In the vicinity of the measurement site in the SJV, there is a strong influence of dairy farm agriculture and minimal urban emissions away from population centers, thus we are able to separate of X_{CH4}/X_{CO2} from dairy sources, from fire or possible urban emissions. The CH_4/CO_2 enhancement ratios observed in this

area make it evident that dairy farms operations are the dominant source of CH_4 during fire and non-fire periods. Nevertheless, CH_4 enhancements during the strong smoke influence periods greatly exceeded CH_4 enhancements from local dairy sources. The immense scale of 2020 wildfires, summing to 28% of the states' CO_2 budget for the year (CO_2 Inventory Scoping Plan, 2022), in addition our observations of elevated fire derived CH_4, suggest that these fires had a significant effect on the state's CH_4 budget.

Given the importance of reducing CH_4 emissions for meeting California's climate goals, we calculate the amount of CH_4 released from the wildfires that burnt in the state in 2020 using estimated CO_2 emissions from the state's wildfire inventory along with emission ratios of CH_4/CO_2 from our study and the literature on fires in California. The California Air Resources Board (CARB) reported CO_2 emissions of 106.7 Tg of CO_2 was emitted from 2020 wildfires, with individual CO_2 emission estimates from the top 20 wildfires. We use estimated CO_2 emissions from the top 20 wildfires to derive CH_4 emissions. The total emissions of CH_4 are calculated by multiplying the emission or enhancement ratio of wildfire smoke and molecular mass ratios:

$$E_{CH4} = \left(ER_{CH4} \times \frac{M_{CH4}}{M_{CO2}}\right) E_{CO2} \quad (8)$$

where E_{CH4} is the emissions of CH_4 in Gg/yr, ERCH4 with respect to CO_2 in mol/mol, M_{CH4} is the molar mass of CH_4 and M_{CO2} is the molar mass of CO_2, and E_{CO2} are the fire specific emissions in Gg/yr. ER from fires are dependent on vegetation type; fires in California fell into temperate forest, shrubland or grassland vegetation types (Xu et al., 2022). Based on the generic vegetation classification from the FINN model

(https://www.acom.ucar.edu/Data/fire/), we classify the top 20 California wildfires of 2020 into the three types based on the dominant vegetation. The ER for the general vegetation was derived from EFs summarized in Xu et al., 2020 and for the Creek and SQF Complex fires we averaged the EFs summarized in Table 1 for the Sierra Nevada and derive an ER shown in Table A2.3, Appendix A2. The top 20 wildfires represented 92% of CO_2 emissions released from wildfires in 2020 and emitted 213.7 ± 49.8 Gg CH4. Figure 3.9 shows the estimated CH_4 emissions from the top 20 largest wildfires of 2020 compared to CARB's 2019 anthropogenic CH_4 inventory emissions, the most recent inventory year available (CH_4 Inventory Scoping Plan, 2022).

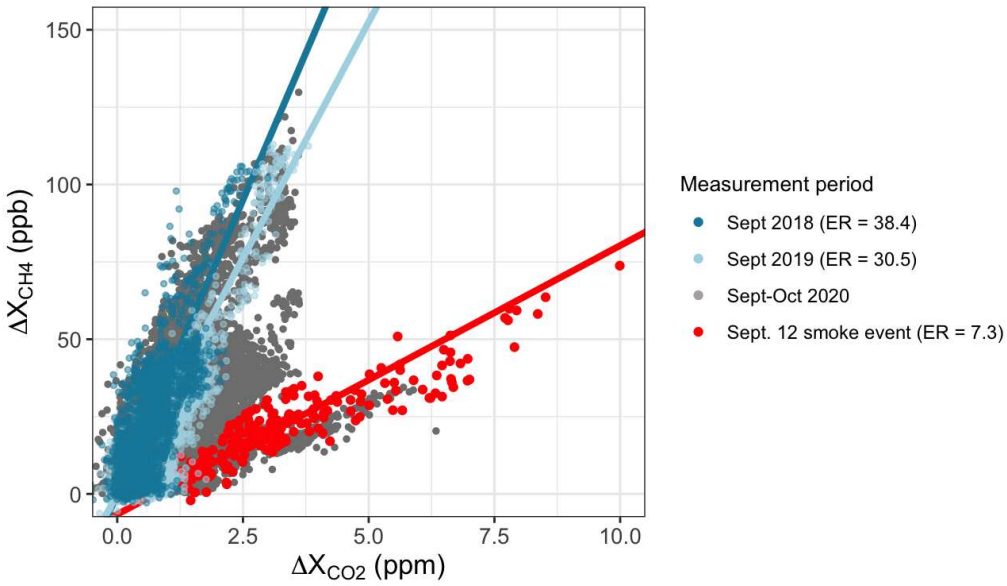

Figure 3.8. Correlation plots of ΔX_{CH4} vs ΔX_{CO2} for SJV measurements collected during non-fire years in Sept. 2018 (blue) and 2019 (light blue), and during fire period of Sept. – Oct. 2020 (gray). The Sept. 12 smoke event (black) highlighted with a linear fit through that day's data clearly shows a distinct $\Delta X_{CH4}/\Delta X_{CO2}$ relationship from other data.

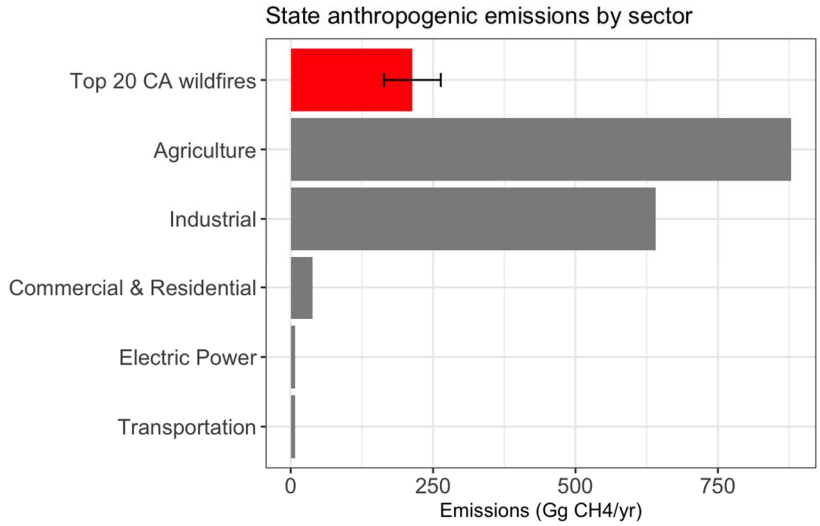

Figure 3.9. California CH_4 emissions from 2020 calculated for the top 20 wildfires compared to the state's anthropogenic CH_4 emissions from the 2019 inventory (CARB, 2019). The industrial sector also includes oil and gas emissions.

3.4 Discussion

We made total column measurements of CO_2, CO, CH_4, and AOD with an EM27/SUN FTIR in the San Joaquin Valley (SJV), California during part of the wildfire season of 2020 from September to October. The emissions of the Creek and SQF Complex fires, two major wildfires burning in the Sierra Nevada, were sampled continuously in the SJV for over a month. We demonstrate that data from the EM27/SUN allows for calculating MCE and EFs in smoke plumes transported from wildfires, especially for high altitude smoke, adding important new estimates for fires in this region. For the Sierra Nevada, only three field-based studies have estimated emission factors in this area despite the increase in wildfires over burns the previous decade (Burling et al., 2011; Yates et al., 2016; Liu et al., 2017). Our emission factor estimates from the September 12 event for CO (120.5 ± 12.2 g kg-1 dry biomass burned) and CH_4 (4.3 ± 0.8 g kg-1 dry biomass burned)

are within the range of those reported from the Sierra Nevada conifer forests (Burling et al., 2011; Yates et al., 2016; Liu et al., 2017). Our atmospheric column-based estimates contribute to the limited number of EF for temperate forests and are particularly important given the scale of the fires that occurred in 2020 in California.

Empirically quantified EFs in temperate conifer forests are limited in number and many of the measurements in these regions are from prescribed burning for land management (Burling et al., 2011; Akagi et al., 2011; Urbanski, 2013). Because prescribed burns typically occur during favorable atmospheric conditions, specified fuel, and during non-wildfire seasons, it is possible that prescribed burn EFs may not represent wildfire EFs that burn under different conditions favorable to wildfires (Urbanski, 2013). There is a need for biome-specific EFs to quantify the amount of trace gas or aerosol emitted per kilogram of biomass burned, and these EFs are essential model inputs for estimating total greenhouse gas and aerosol emissions of fires.

Field measurements have also been limited in measuring a smaller fraction of the smoke plume. Airborne measurements are the most common method to estimate EFs from wildfires and involve aircraft equipped with fast response gas analyzers sampling through smoke plumes (e.g. Yokelson et al., 1999; Yates et al., 2016; Iraci et al., 2022). Although highly effective for large and remote wildfires, this method can be costly and logistically complex, limiting the number of fires sampled during a campaign period (Ross et al., 2013). In situ stations downwind of fires are able to provide measurements when aircraft are unable to fly but they oversample in smoldering conditions where the fire burns less vigorously and emissions are released closer to the ground. Aircraft measurements tend to

sample lofted fire samples in the flaming phase, resulting in different emissions than a fire in situ measurements (Paton-Walsh et al., 2005). Although much has been learned from these methods, an average sample of the fire plumes is difficult to obtain due to variability in emissions from the fire burning at different stages (Paton-Walsh et al., 2005). Open-path FTIR measurements have allowed for "whole-fire" emission factors (Smith et al., 2014). Total-column measurements can provide a plume-integrated EF and MCE; however, calculating EFs with respect to CO_2 in the vertical column has been challenging due to high atmospheric background (Kille et al., 2022; Paton-Walsh et al., 2005; Lutsch et al., 2020, 2016; Viatte et al., 2014, 2015). Portable solar viewing instruments like the EM27/SUN have the advantage of remotely sampling total columns closer to the source and capturing a vertical integration of transported smoke plumes, contributing to the limited number of EFs across biomes and understanding impact on regional smoke influence background.

Simultaneous measurements of ground-based total columns and satellites allow for a spatial and temporal understanding of the fire events. The X_{CO} enhancement from the 2020 wildfires in the Sierra Nevada was also observed from space and smoke plumes up to ten times higher than the local background are visible in the TROPOMI soundings on the Sept. 12. smoke event. Pairing stationary ground-based column observations with satellites can help in understanding regional wildfires at a greater spatial and temporal scale. Although TROPOMI has daily global coverage with great resolution, daily snapshots are often not enough to understand the behavior of a fire. Conversely, stationary ground-based instruments are limited to observing a point in space. As an instrument with capability of measuring atmospheric columns, the EM27/SUN can help close the gap in

the temporal scale of satellite observations. The EM27/SUN measured continuously in the daytime filling in the temporal gaps from the satellite TROPOMI's single overpass observations. A sensitivity study showed that a smaller radius of 5 or 15 km from TROPOMI observations paired with 30-minute averaging around the overpass time gave better statistical agreement during wildfire events. This strong correlation of X_{CO} between TROPOMI and the EM27/SUN has been observed before in urban sites (Sagar et al., 2022; Alberti et al., 2022b) and in rural Alaska (Jacobs, 2021). Jacobs (2021) found that wildfire influences in X_{CO} resulted in high observational variance in EM27/SUN observations and they suggest that this may be due to spatial and temporal variability in the smoke plume measured by TROPOMI and the EM27/SUN. The 9.7% overestimation from TROPOMI found in this study may also be due to averaging of the smoke plume's heterogeneity within each TROPOMI comparison point. Alternatively, Rowe et al. (2022) found that multiple scattering on aerosols may be responsible for 5-10% increased X_{CO} observations from TROPOMI in thick smoke plumes.

The air quality index in the SJV was at an all-time high in the hazardous range for weeks during the 2020 wildfire season (Morris III and Dennis, 2020) and AOD at the AERONET site in Fresno increased by three to five times higher than yearly average from 2002-2019 (Cho et al., 2022). FTIR-derived AOD at 500 nm reached extreme highs during the Sept. 12 smoke plume event, and followed the same trend on other days as the trace gas enhancements. The slopes during low smoke and high smoke days were consistent with previous satellite observations by McMillan et al. (2008). Previously, simultaneous measurements of aerosols and trace gases from the same instrument has been limited due

to the aerosol burden interfering with retrieval of trace gases. For example, the majority of the TROPOMI X_{CH4} product was flagged out completely near the observational site during the Sept 7 – 15 period, and hence was not included in this analysis. The EM27/SUN demonstrated the potential to elucidate trace gas and aerosol relationships even during thick aerosol periods. Similarly, future studies may use simultaneous measurements from TROPOMI X_{CO} product and AOD to study regional impacts from wildfires (Chen et al., 2021). Scattered diffuse light during high aerosol loading from biomass burning may decrease the reliability of the AOD observations, thus further verification of the FTIR-derived AOD during high aerosol loading is required. Since the nearest AERONET station was relatively far away from our EM27/SUN site, we cannot do a true side-by-side comparison. However, the FTIR derived AOD showed the same baseline pattern as the AERONET site in Fresno, demonstrating the ability of the EM27 to simultaneously measure AOD and trace gases through a thick plume of smoke which can elucidate mechanisms within smoke plumes.

As fires become more frequent with climate change, monitoring trace gases and particulates may become especially challenging in mixed source areas like the San Joaquin Valley where concentrations can become amplified by stagnant conditions in the SJV. Moreover, the fire-added CH_4 may hamper evaluation of greenhouse gas emission reduction initiatives at the state and at the global scale by adding unaccounted for CH_4 to the atmosphere. Using CARB's 2020 wildfire emission estimate for CO_2, we calculated the CH_4 contribution from the top 20 largest fires to be 213.7 ± 49.8 Gg CH_4, respectively. These wildfires alone emitted 13.6% of the total state CH_4 emissions, more than the

transportation, electric power, and commercial and residential sectors. While estimated CH_4 emissions from wildfires are smaller in magnitude than inventoried emissions from agriculture and industrial sources, this source should be considered in the state's inventory given its magnitude and large impacts on the atmospheric CH_4 during wildfire periods. Additionally, wildfire emitted CH_4 may be an important and unaccounted positive feedback to climate change given the effect of increasing temperatures on fire severity.

3.5 Conclusions

Over the past 50 years, approximately three quarters of the area burned by wildfires in California's has been in North Coast and Sierra Nevada (Williams et al., 2019), highlighting the importance of studying emission factors from fires in these systems. However, there are surprisingly few observations of emission factors from these fires despite their importance to California's greenhouse gas budgets and air quality. The ground-based EM27/SUN is a useful instrument for understanding emissions of trace gases and aerosols from wildfires at a regional scales. The portable nature of the EM27/SUN allows for deployment downwind of fires for calculating important variables like EF and MCE. Having alternate techniques to calculate emission factors that are not costly or complex to deploy adds to the small number of emissions required to accurately calculate emissions and construct wildfire inventories. Several studies have demonstrated the utility in FTIR-derived EF for studying whole fire emissions from open path instruments (Paton-Walsh et al., 2014) and vertically integrated measurements (Viatte et al., 2013). Our total column MCE and EF with respect to CO_2 are the first to be reported from ground-based FTIR measurements in California.

Wildfire smoke produced overcast skies throughout the Western U.S. during this period, with smoke plumes transported long distances. The EM27/SUN measures a vertically integrated regional signal but is limited spatially compared to observations from satellites. Here we show that a combination of the two can elucidate spatiotemporal variability of wildfire emissions. We find strong agreement between the EM27/SUN and TROPOMI, but TROPOMI overestimates observations by 9.7%. This is consistent with previous studies of EM27 X_{CO} in rural Alaska (Jacobs, 2021) and Idaho wildfires (Rowe et al., 2022). Additionally, our solar spectral measurements were used to derive AOD. We compared to a nearby AERONET site and found AOD values at 1020.9 and 1636 nm that were consistent with AERONET observations. The Ångström exponent was used to calculate FTIR AOD at 500 nm to compare AOD to CO ratios with previous studies. AOD at 500 nm reached extreme levels of up to 15 during the smoke plume event. Good agreements were found of AOD to CO ratios with those observed in McMillian et al., 2008 from MODIS AOD and AIRS CO.

Finally, we find that a significant amount of CH_4 was emitted from the top 20 largest wildfires of 2020 in California. Given the importance of CH_4 emissions reduction for the state, our study suggests wildfires are an important source of CH_4 for California and may delay meeting the state's ambitious goals of reducing emissions. Atmospheric monitoring of CH_4 should account for wildfire periods, as they can significantly affect measured enhancements. Overall, our analysis demonstrates a novel application of the EM27/SUN solar spectrometers and will contribute to the development of techniques for analyzing remotely sensed greenhouse gas measurements from wildfires.

3.6 Acknowledgements

We would also like to thank our funding source the University of California Office of the President Lab Fees Research Program (award LFR-18-548581) & National Science Foundation Graduate Research Fellowship Program. We thank Nicole Jacobs for providing code to apply the averaging kernel correction to EM27/SUN X_{CO} data. We thank Jacob Hedelius for providing code through EGI to read micro windows from EM27/SUN retrievals. The authors thank William Porter for the assistance and access to UCR-Aldo cluster.

3.7 References

Aguilera, R., Corringham, T., Gershunov, A., and Benmarhnia, T.: Wildfire smoke impacts respiratory health more than fine particles from other sources: observational evidence from Southern California, Nat Commun, 12, 1493, https://doi.org/10.1038/s41467-021-21708-0, 2021.

Ahangar, F., Cobian-Iñiguez, J., and Cisneros, R.: Combining Regulatory Instruments and Low-Cost Sensors to Quantify the Effects of 2020 California Wildfires on PM2.5 in San Joaquin Valley, Fire, 5, 64, https://doi.org/10.3390/fire5030064, 2022.

Akagi, S. K., Yokelson, R. J., Wiedinmyer, C., Alvarado, M. J., Reid, J. S., Karl, T., Crounse, J. D., and Wennberg, P. O.: Emission factors for open and domestic biomass burning for use in atmospheric models, Atmos. Chem. Phys., 11, 4039–4072, https://doi.org/10.5194/acp-11-4039-2011, 2011.

Alberti, C., Hase, F., Frey, M., Dubravica, D., Blumenstock, T., Dehn, A., Castracane, P., Surawicz, G., Harig, R., Baier, B. C., Bès, C., Bi, J., Boesch, H., Butz, A., Cai, Z., Chen, J., Crowell, S. M., Deutscher, N. M., Ene, D., Franklin, J. E., García, O., Griffith, D., Grouiez, B., Grutter, M., Hamdouni, A., Houweling, S., Humpage, N., Jacobs, N., Jeong, S., Joly, L., Jones, N. B., Jouglet, D., Kivi, R., Kleinschek, R., Lopez, M., Medeiros, D. J., Morino, I., Mostafavipak, N., Müller, A., Ohyama, H., Palmer, P. I., Pathakoti, M., Pollard, D. F., Raffalski, U., Ramonet, M., Ramsay, R., Sha, M. K., Shiomi, K., Simpson, W., Stremme, W., Sun, Y., Tanimoto, H., Té, Y., Tsidu, G. M., Velazco, V. A., Vogel, F., Watanabe, M., Wei, C., Wunch, D., Yamasoe, M., Zhang, L., and Orphal, J.: Improved calibration procedures for the EM27/SUN spectrometers of the COllaborative Carbon Column Observing Network (COCCON), Atmos. Meas. Tech., 15, 2433–2463, https://doi.org/10.5194/amt-15-2433-2022, 2022a.

Alberti, C., Tu, Q., Hase, F., Makarova, M. V., Gribanov, K., Foka, S. C., Zakharov, V., Blumenstock, T., Buchwitz, M., Diekmann, C., Ertl, B., Frey, M. M., Imhasin, H. Kh., Ionov, D. V., Khosrawi, F., Osipov, S. I., Reuter, M., Schneider, M., and Warneke, T.: Investigation of spaceborne trace gas products over St Petersburg and Yekaterinburg, Russia, by using COllaborative Column Carbon Observing Network (COCCON) observations, Atmos. Meas. Tech., 15, 2199–2229, https://doi.org/10.5194/amt-15-2199-2022, 2022b.

Andreae, M. O.: Emission of trace gases and aerosols from biomass burning – an updated assessment, Atmos. Chem. Phys., 19, 8523–8546, https://doi.org/10.5194/acp-19-8523-2019, 2019.

Burling, I. R., Yokelson, R. J., Griffith, D. W. T., Johnson, T. J., Veres, P., Roberts, J. M., Warneke, C., Urbanski, S. P., Reardon, J., Weise, D. R., Hao, W. M., and de

Gouw, J.: Laboratory measurements of trace gas emissions from biomass burning of fuel types from the southeastern and southwestern United States, Atmos. Chem. Phys., 10, 11115–11130, https://doi.org/10.5194/acp-10-11115-2010, 2010.

Burling, I. R., Yokelson, R. J., Akagi, S. K., Urbanski, S. P., Wold, C. E., Griffith, D. W. T., Johnson, T. J., Reardon, J., and Weise, D. R.: Airborne and ground-based measurements of the trace gases and particles emitted by prescribed fires in the United States, Atmos. Chem. Phys., 11, 12197–12216, https://doi.org/10.5194/acp-11-12197-2011, 2011.

CARB: An Inventory of Ecosystem Carbon in California's Natural & Working Lands, 2018.

CH4 Inventory Scoping Plan: https://ww3.arb.ca.gov/cc/inventory/data/tables/ghg_inventory_scopingplan_2000-19ch4.pdf, last access: 21 August 2022.

CO2 Inventory Scoping Plan: https://ww3.arb.ca.gov/cc/inventory/data/tables/ghg_inventory_scopingplan_2000-19co2.pdf, last access: 21 August 2022.

California Wildfire Emission Estimates: https://ww2.arb.ca.gov/wildfire-emissions, last access: 30 May 2021.

Chen, J., Viatte, C., Hedelius, J. K., Jones, T., Franklin, J. E., Parker, H., Gottlieb, E. W., Wennberg, P. O., Dubey, M. K., and Wofsy, S. C.: Differential column measurements using compact solar-tracking spectrometers, Atmos. Chem. Phys., 16, 8479–8498, https://doi.org/10.5194/acp-16-8479-2016, 2016.

Chen, X., Wang, J., Xu, X., Zhou, M., Zhang, H., Castro Garcia, L., Colarco, P. R., Janz, S. J., Yorks, J., McGill, M., Reid, J. S., de Graaf, M., and Kondragunta, S.: First retrieval of absorbing aerosol height over dark target using TROPOMI oxygen B band: Algorithm development and application for surface particulate matter estimates, Remote Sensing of Environment, 265, 112674, https://doi.org/10.1016/j.rse.2021.112674, 2021.

Cho, C., Kim, S.-W., Choi, W., and Kim, M.-H.: Significant light absorption of brown carbon during the 2020 California wildfires, Science of The Total Environment, 813, 152453, https://doi.org/10.1016/j.scitotenv.2021.152453, 2022.

De Mazière, M., Thompson, A. M., Kurylo, M. J., Wild, J. D., Bernhard, G., Blumenstock, T., Braathen, G. O., Hannigan, J. W., Lambert, J.-C., Leblanc, T., McGee, T. J., Nedoluha, G., Petropavlovskikh, I., Seckmeyer, G., Simon, P. C., Steinbrecht, W., and Strahan, S. E.: The Network for the Detection of

Atmospheric Composition Change (NDACC): history, status and perspectives, Atmos. Chem. Phys., 18, 4935–4964, https://doi.org/10.5194/acp-18-4935-2018, 2018.

Dietrich, F., Chen, J., Voggenreiter, B., Aigner, P., Nachtigall, N., and Reger, B.: MUCCnet: Munich Urban Carbon Column network, Atmos. Meas. Tech., 14, 1111–1126, https://doi.org/10.5194/amt-14-1111-2021, 2021.

Frey, M., Sha, M. K., Hase, F., Kiel, M., Blumenstock, T., Harig, R., Surawicz, G., Deutscher, N. M., Shiomi, K., Franklin, J. E., Bösch, H., Chen, J., Grutter, M., Ohyama, H., Sun, Y., Butz, A., Mengistu Tsidu, G., Ene, D., Wunch, D., Cao, Z., Garcia, O., Ramonet, M., Vogel, F., and Orphal, J.: Building the COllaborative Carbon Column Observing Network (COCCON): long-term stability and ensemble performance of the EM27/SUN Fourier transform spectrometer, Atmos. Meas. Tech., 12, 1513–1530, https://doi.org/10.5194/amt-12-1513-2019, 2019.

Gutierrez, A. A., Hantson, S., Langenbrunner, B., Chen, B., Jin, Y., Goulden, M. L., and Randerson, J. T.: Wildfire response to changing daily temperature extremes in California's Sierra Nevada, Sci. Adv., 7, eabe6417, https://doi.org/10.1126/sciadv.abe6417, 2021.

Hase, F., Frey, M., Kiel, M., Blumenstock, T., Harig, R., Keens, A., and Orphal, J.: Addition of a channel for XCO observations to a portable FTIR spectrometer for greenhouse gas measurements, Atmos. Meas. Tech., 9, 2303–2313, https://doi.org/10.5194/amt-9-2303-2016, 2016.

Hedelius, J. K., Viatte, C., Wunch, D., Roehl, C. M., Toon, G. C., Chen, J., Jones, T., Wofsy, S. C., Franklin, J. E., Parker, H., Dubey, M. K., and Wennberg, P. O.: Assessment of errors and biases in retrievals of XCO2, XCH4, XCO, and XN2O from a 0.5 cm−1 resolution solar-viewing spectrometer, Atmos. Meas. Tech., 20, 2016.

Heerah, S., Frausto□Vicencio, I., Jeong, S., Marklein, A. R., Ding, Y., Meyer, A. G., Parker, H. A., Fischer, M. L., Franklin, J. E., Hopkins, F. M., and Dubey, M.: Dairy Methane Emissions in California's San Joaquin Valley Inferred With Ground□Based Remote Sensing Observations in the Summer and Winter, JGR Atmospheres, 126, https://doi.org/10.1029/2021JD034785, 2021.

Herrera, S. A., Diskin, G. S., Harward, C., Sachse, G., De Wekker, S. F. J., Yang, M., Choi, Y., Wisthaler, A., Mallia, D. V., and Pusede, S. E.: Wintertime Nitrous Oxide Emissions in the San Joaquin Valley of California Estimated from Aircraft Observations, Environ. Sci. Technol., 55, 4462–4473, https://doi.org/10.1021/acs.est.0c08418, 2021.

IPCC: Climate Change 2014: Mitigation of Climate Change. Working Group III Contribution to the Fifth Assessment Report of the Intergovernmental Panel on Climate Change, edited by: Edenhofer, O., Pichis-Madruga, R., Sokona, Y., Farahani, E., Kadner, S., Seyboth, A., Adler, A., Baum, I., Brunner, S., Eickmeier, P., Kriemann, B., Savolainen, J., Schlomer, S., von Stechow, C., and Zwickel, T., Cambridge University Press, New York, NY, 1435 pp., 2014.

Jacobs, N.: Vetting Model and Satellite-Based Estimates of Regional Scale Carbon Exchange at Northern High Latitudes Using Solar-Viewing Infrared Spectroscopy, ProQuest Dissertations Publishing, 2021.

Jain, P., Castellanos-Acuna, D., Coogan, S. C. P., Abatzoglou, J. T., and Flannigan, M. D.: Observed increases in extreme fire weather driven by atmospheric humidity and temperature, Nat. Clim. Chang., 12, 63–70, https://doi.org/10.1038/s41558-021-01224-1, 2022.

Kalnay, E., Kanamitsu, M., Kistler, R., Collins, W., Deaven, D., Gandin, L., Iredell, M., Saha, S., White, G., Woollen, J., Zhu, Y., Chelliah, M., Ebisuzaki, W., Higgins, W., Janowiak, J., Mo, K. C., Ropelewski, C., Wang, J., Leetmaa, A., Reynolds, R., Jenne, R., and Joseph, D.: The NCEP/NCAR 40-Year Reanalysis Project, Bulletin of the American Meteorological Society, 77, 437–472, https://doi.org/10.1175/1520-0477(1996)077<0437:TNYRP>2.0.CO;2, 1996.

Kampe, T. U. and Sokolik, I. N.: Remote sensing retrievals of fine mode aerosol optical depth and impacts on its correlation with CO from biomass burning, Geophys. Res. Lett., 34, L12806, https://doi.org/10.1029/2007GL029805, 2007.

Kille, N., Zarzana, K. J., Alvarez, J. R., Lee, C. F., Rowe, J. P., Howard, B., Campos, T., Hills, A., Hornbrook, R. S., Ortega, I., Permar, W., Ku, I. T., Lindaas, J., Pollack, I. B., Sullivan, A. P., Zhou, Y., Fredrickson, C. D., Palm, B. B., Peng, Q., Apel, E. C., Hu, L., Collett, J. L., Fischer, E. V., Flocke, F., Hannigan, J. W., Thornton, J., and Volkamer, R.: The CU Airborne Solar Occultation Flux Instrument: Performance Evaluation during BB-FLUX, ACS Earth and Space Chemistry, 15, 2022.

Li, M., Karu, E., Brenninkmeijer, C., Fischer, H., Lelieveld, J., and Williams, J.: Tropospheric OH and stratospheric OH and Cl concentrations determined from CH4, CH3Cl, and SF6 measurements, npj Clim Atmos Sci, 1, 1–7, https://doi.org/10.1038/s41612-018-0041-9, 2018.

Lindenmaier, R., Dubey, M. K., Henderson, B. G., Butterfield, Z. T., Herman, J. R., Rahn, T., and Lee, S.-H.: Multiscale observations of CO_2, $^{13}CO_2$, and pollutants at Four Corners for emission verification and attribution, Proc. Natl. Acad. Sci. U.S.A., 111, 8386–8391, https://doi.org/10.1073/pnas.1321883111, 2014.

Liu, X., Huey, L. G., Yokelson, R. J., Selimovic, V., Simpson, I. J., Müller, M., Jimenez, J. L., Campuzano□Jost, P., Beyersdorf, A. J., Blake, D. R., Butterfield, Z., Choi, Y., Crounse, J. D., Day, D. A., Diskin, G. S., Dubey, M. K., Fortner, E., Hanisco, T. F., Hu, W., King, L. E., Kleinman, L., Meinardi, S., Mikoviny, T., Onasch, T. B., Palm, B. B., Peischl, J., Pollack, I. B., Ryerson, T. B., Sachse, G. W., Sedlacek, A. J., Shilling, J. E., Springston, S., St. Clair, J. M., Tanner, D. J., Teng, A. P., Wennberg, P. O., Wisthaler, A., and Wolfe, G. M.: Airborne measurements of western U.S. wildfire emissions: Comparison with prescribed burning and air quality implications, JGR Atmospheres, 122, 6108–6129, https://doi.org/10.1002/2016JD026315, 2017.

Lobert, J. M.: Trace gases and air mass origin at Kaashidhoo, Indian Ocean, J. Geophys. Res., 107, 8013, https://doi.org/10.1029/2001JD000731, 2002.

Lueker, T. J., Keeling, R. F., and Dubey, M. K.: The oxygen to carbon dioxide ratios observed in emissions from a wildfire in northern California, Geophys. Res. Lett., 28, 2413–2416, https://doi.org/10.1029/2000GL011860, 2001.

Lutsch, E., Dammers, E., Conway, S., and Strong, K.: Long-range transport of NH_3, CO, HCN, and C_2H_6 from the 2014 Canadian Wildfires: CANADIAN WILDFIRE EMISSIONS OF NH_3, Geophys. Res. Lett., 43, 8286–8297, https://doi.org/10.1002/2016GL070114, 2016.

Lutsch, E., Strong, K., Jones, D. B. A., Blumenstock, T., Conway, S., Fisher, J. A., Hannigan, J. W., Hase, F., Kasai, Y., Mahieu, E., Makarova, M., Morino, I., Nagahama, T., Notholt, J., Ortega, I., Palm, M., Poberovskii, A. V., Sussmann, R., and Warneke, T.: Detection and attribution of wildfire pollution in the Arctic and northern midlatitudes using a network of Fourier-transform infrared spectrometers and GEOS-Chem, Atmos. Chem. Phys., 20, 12813–12851, https://doi.org/10.5194/acp-20-12813-2020, 2020.

Makarova, M. V., Alberti, C., Ionov, D. V., Hase, F., Foka, S. C., Blumenstock, T., Warneke, T., Virolainen, Y. A., Kostsov, V. S., Frey, M., Poberovskii, A. V., Timofeyev, Y. M., Paramonova, N. N., Volkova, K. A., Zaitsev, N. A., Biryukov, E. Y., Osipov, S. I., Makarov, B. K., Polyakov, A. V., Ivakhov, V. M., Imhasin, H. Kh., and Mikhailov, E. F.: Emission Monitoring Mobile Experiment (EMME): an overview and first results of the St. Petersburg megacity campaign 2019, Atmos. Meas. Tech., 14, 1047–1073, https://doi.org/10.5194/amt-14-1047-2021, 2021.

Marklein, A. R., Meyer, D., Fischer, M. L., Jeong, S., Rafiq, T., Carr, M., and Hopkins, F. M.: Facility-scale inventory of dairy methane emissions in California: implications for mitigation, Earth Syst. Sci. Data, 13, 1151–1166, https://doi.org/10.5194/essd-13-1151-2021, 2021.

McKain, K., Down, A., Raciti, S. M., Budney, J., Hutyra, L. R., Floerchinger, C., Herndon, S. C., Nehrkorn, T., Zahniser, M. S., Jackson, R. B., Phillips, N., and Wofsy, S. C.: Methane emissions from natural gas infrastructure and use in the urban region of Boston, Massachusetts, Proc. Natl. Acad. Sci. U.S.A., 112, 1941–1946, https://doi.org/10.1073/pnas.1416261112, 2015.

McMillan, W. W., Warner, J. X., Comer, M. M., Maddy, E., Chu, A., Sparling, L., Eloranta, E., Hoff, R., Sachse, G., Barnet, C., Razenkov, I., and Wolf, W.: AIRS views transport from 12 to 22 July 2004 Alaskan/Canadian fires: Correlation of AIRS CO and MODIS AOD with forward trajectories and comparison of AIRS CO retrievals with DC-8 in situ measurements during INTEX-A/ICARTT, J. Geophys. Res., 113, D20301, https://doi.org/10.1029/2007JD009711, 2008.

Morris III, G. and Dennis, C.: 2020 Fire Siege, CALFIRE, 2020.

Navarro, K. M., Cisneros, R., and Balmes, J. R.: Air-Quality Impacts and Intake Fraction of PM2.5 during the 2013 Rim Megafire, Environ. Sci. Technol., 9, 2016.

Paton-Walsh, C., Jones, N. B., Wilson, S. R., Haverd, V., Meier, A., Griffith, D. W. T., and Rinsland, C. P.: Measurements of trace gas emissions from Australian forest fires and correlations with coincident measurements of aerosol optical depth, J. Geophys. Res., 110, D24305, https://doi.org/10.1029/2005JD006202, 2005.

Paton-Walsh, C., Smith, T. E. L., Young, E. L., Griffith, D. W. T., and Guérette, É.-A.: New emission factors for Australian vegetation fires measured using open-path Fourier transform infrared spectroscopy – Part 1: Methods and Australian temperate forest fires, Atmos. Chem. Phys., 14, 11313–11333, https://doi.org/10.5194/acp-14-11313-2014, 2014.

Porter, J. N., Miller, M., Pietras, C., and Motell, C.: Ship-Based Sun Photometer Measurements Using Microtops Sun Photometers, J. Atmos. Oceanic Technol., 18, 765–774, https://doi.org/10.1175/1520-0426(2001)018<0765:SBSPMU>2.0.CO;2, 2001.

Prichard, S. J., O'Neill, S. M., Eagle, P., Andreu, A. G., Drye, B., Dubowy, J., Urbanski, S., and Strand, T. M.: Wildland fire emission factors in North America: synthesis of existing data, measurement needs and management applications, Int. J. Wildland Fire, 29, 132, https://doi.org/10.1071/WF19066, 2020.

Ross, A. N., Wooster, M. J., Boesch, H., and Parker, R.: First satellite measurements of carbon dioxide and methane emission ratios in wildfire plumes: GOSAT MEASURE OF CO_2:CH_4 EMISSION RATIO, Geophys. Res. Lett., 40, 4098–4102, https://doi.org/10.1002/grl.50733, 2013.

Rowe, J. P., Zarzana, K. J., Kille, N., Borsdorff, T., Goudar, M., Lee, C. F., Koenig, T. K., Romero-Alvarez, J., Campos, T., Knote, C., Theys, N., Landgraf, J., and Volkamer, R.: Carbon Monoxide in Optically Thick Wildfire Smoke: Evaluating TROPOMI Using CU Airborne SOF Column Observations, ACS Earth Space Chem., 6, 1799–1812, https://doi.org/10.1021/acsearthspacechem.2c00048, 2022.

Sagar, V. K., Pathakoti, M., D.V., M., K.S., R., M.V.R., S. S., Hase, F., Dubravica, D., and Sha, M. K.: Ground-Based Remote Sensing of Total Columnar CO_2, CH_4, and CO Using EM27/SUN FTIR Spectrometer at a Suburban Location (Shadnagar) in India and Validation of Sentinel-5P/TROPOMI, IEEE Geosci. Remote Sensing Lett., 19, 1–5, https://doi.org/10.1109/LGRS.2022.3171216, 2022.

Schneising, O., Buchwitz, M., Reuter, M., Bovensmann, H., and Burrows, J. P.: Severe Californian wildfires in November 2018 observed from space: the carbon monoxide perspective, Atmos. Chem. Phys., 20, 3317–3332, https://doi.org/10.5194/acp-20-3317-2020, 2020.

Sha, M. K., Langerock, B., Blavier, J.-F. L., Blumenstock, T., Borsdorff, T., Buschmann, M., Dehn, A., De Mazière, M., Deutscher, N. M., Feist, D. G., García, O. E., Griffith, D. W. T., Grutter, M., Hannigan, J. W., Hase, F., Heikkinen, P., Hermans, C., Iraci, L. T., Jeseck, P., Jones, N., Kivi, R., Kumps, N., Landgraf, J., Lorente, A., Mahieu, E., Makarova, M. V., Mellqvist, J., Metzger, J.-M., Morino, I., Nagahama, T., Notholt, J., Ohyama, H., Ortega, I., Palm, M., Petri, C., Pollard, D. F., Rettinger, M., Robinson, J., Roche, S., Roehl, C. M., Röhling, A. N., Rousogenous, C., Schneider, M., Shiomi, K., Smale, D., Stremme, W., Strong, K., Sussmann, R., Té, Y., Uchino, O., Velazco, V. A., Vigouroux, C., Vrekoussis, M., Wang, P., Warneke, T., Wizenberg, T., Wunch, D., Yamanouchi, S., Yang, Y., and Zhou, M.: Validation of methane and carbon monoxide from Sentinel-5 Precursor using TCCON and NDACC-IRWG stations, Atmos. Meas. Tech., 14, 6249–6304, https://doi.org/10.5194/amt-14-6249-2021, 2021.

Smith, T. E. L., Paton-Walsh, C., Meyer, C. P., Cook, G. D., Maier, S. W., Russell-Smith, J., Wooster, M. J., and Yates, C. P.: New emission factors for Australian vegetation fires measured using open-path Fourier transform infrared spectroscopy – Part 2: Australian tropical savanna fires, Atmos. Chem. Phys., 14, 11335–11352, https://doi.org/10.5194/acp-14-11335-2014, 2014.

Sommers, W. T., Loehman, R. A., and Hardy, C. C.: Wildland fire emissions, carbon, and climate: Science overview and knowledge needs, Forest Ecology and Management, 317, 1–8, https://doi.org/10.1016/j.foreco.2013.12.014, 2014.

Stephensen, N. and Brigham, C.: Preliminary Estimates of Sequoia Mortality in the 2020 Castle Fire (U.S. National Park Service), 2021.

Toon, G., Blavier, J.-F., Washenfelder, R., Wunch, D., Keppel-Aleks, G., Wennberg, P., Connor, B., Sherlock, V., Griffith, D., Deutscher, N., and Notholt, J.: Total Column Carbon Observing Network (TCCON), in: Advances in Imaging, Fourier Transform Spectroscopy, Vancouver, JMA3, https://doi.org/10.1364/FTS.2009.JMA3, 2009.

UNEP: Spreading like Wildfire – The Rising Threat of Extraordinary Landscape Fires, United Nations Environment Programme, Nairobi, 2022.

Urbanski, S.: Wildland fire emissions, carbon, and climate: Emission factors, Forest Ecology and Management, 317, 51–60, https://doi.org/10.1016/j.foreco.2013.05.045, 2014.

Urbanski, S. P.: Combustion efficiency and emission factors for wildfire-season fires in mixed conifer forests of the northern Rocky Mountains, US, Atmos. Chem. Phys., 13, 7241–7262, https://doi.org/10.5194/acp-13-7241-2013, 2013.

Veefkind, J. P., Aben, I., McMullan, K., Förster, H., de Vries, J., Otter, G., Claas, J., Eskes, H. J., de Haan, J. F., Kleipool, Q., van Weele, M., Hasekamp, O., Hoogeveen, R., Landgraf, J., Snel, R., Tol, P., Ingmann, P., Voors, R., Kruizinga, B., Vink, R., Visser, H., and Levelt, P. F.: TROPOMI on the ESA Sentinel-5 Precursor: A GMES mission for global observations of the atmospheric composition for climate, air quality and ozone layer applications, Remote Sensing of Environment, 120, 70–83, https://doi.org/10.1016/j.rse.2011.09.027, 2012.

Viatte, C., Strong, K., Paton-Walsh, C., Mendonca, J., O'Neill, N. T., and Drummond, J. R.: Measurements of CO, HCN, and C_2H_6 Total Columns in Smoke Plumes Transported from the 2010 Russian Boreal Forest Fires to the Canadian High Arctic, Atmosphere-Ocean, 51, 522–531, https://doi.org/10.1080/07055900.2013.823373, 2013.

Viatte, C., Strong, K., Walker, K. A., and Drummond, J. R.: Five years of CO, HCN, C₂H₆, C₂H₂, CH₃OH, HCOOH and H₂CO total columns measured in the Canadian high Arctic, Atmos. Meas. Tech., 7, 1547–1570, https://doi.org/10.5194/amt-7-1547-2014, 2014.

Viatte, C., Strong, K., Hannigan, J., Nussbaumer, E., Emmons, L. K., Conway, S., Paton-Walsh, C., Hartley, J., Benmergui, J., and Lin, J.: Identifying fire plumes in the Arctic with tropospheric FTIR measurements and transport models, Atmos. Chem. Phys., 15, 2227–2246, https://doi.org/10.5194/acp-15-2227-2015, 2015.

Viatte, C., Lauvaux, T., Hedelius, J. K., Parker, H., Chen, J., Jones, T., Franklin, J. E., Deng, A. J., Gaudet, B., Verhulst, K., Duren, R., Wunch, D., Roehl, C., Dubey,

M. K., Wofsy, S., and Wennberg, P. O.: Methane emissions from dairies in the Los Angeles Basin, Atmos. Chem. Phys., 17, 7509–7528, https://doi.org/10.5194/acp-17-7509-2017, 2017.

Wiedinmyer, C., Akagi, S. K., Yokelson, R. J., Emmons, L. K., Al-Saadi, J. A., Orlando, J. J., and Soja, A. J.: The Fire INventory from NCAR (FINN): a high resolution global model to estimate the emissions from open burning, Geoscientific Model Development, 4, 625–641, https://doi.org/10.5194/gmd-4-625-2011, 2011.

Williams, A. P., Abatzoglou, J. T., Gershunov, A., Guzman□Morales, J., Bishop, D. A., Balch, J. K., and Lettenmaier, D. P.: Observed Impacts of Anthropogenic Climate Change on Wildfire in California, Earth's Future, 7, 892–910, https://doi.org/10.1029/2019EF001210, 2019.

Wilmot, T. Y., Mallia, D. V., Hallar, A. G., and Lin, J. C.: Wildfire plumes in the Western US are reaching greater heights and injecting more aerosols aloft as wildfire activity intensifies, Sci Rep, 12, 12400, https://doi.org/10.1038/s41598-022-16607-3, 2022.

Wunch, D., Wennberg, P. O., Toon, G. C., Keppel-Aleks, G., and Yavin, Y. G.: Emissions of greenhouse gases from a North American megacity: GREENHOUSE GAS EMISSIONS IN LA, Geophys. Res. Lett., 36, n/a-n/a, https://doi.org/10.1029/2009GL039825, 2009.

Wunch, D., Toon, G. C., Blavier, J.-F. L., Washenfelder, R. A., Notholt, J., Connor, B. J., Griffith, D. W. T., Sherlock, V., and Wennberg, P. O.: The Total Carbon Column Observing Network, Phil. Trans. R. Soc. A., 369, 2087–2112, https://doi.org/10.1098/rsta.2010.0240, 2011.

Xu, Q., Westerling, A. L., Notohamiprodjo, A., Wiedinmyer, C., Picotte, J. J., Parks, S. A., Hurteau, M. D., Marlier, M. E., Kolden, C. A., Sam, J. A., Baldwin, W. J., and Ade, C.: Wildfire burn severity and emissions inventory: an example implementation over California, Environ. Res. Lett., 17, 085008, https://doi.org/10.1088/1748-9326/ac80d0, 2022.

Yates, E. L., Iraci, L. T., Singh, H. B., Tanaka, T., Roby, M. C., Hamill, P., Clements, C. B., Lareau, N., Contezac, J., Blake, D. R., Simpson, I. J., Wisthaler, A., Mikoviny, T., Diskin, G. S., Beyersdorf, A. J., Choi, Y., Ryerson, T. B., Jimenez, J. L., Campuzano-Jost, P., Loewenstein, M., and Gore, W.: Airborne measurements and emission estimates of greenhouse gases and other trace constituents from the 2013 California Yosemite Rim wildfire, Atmospheric Environment, 127, 293–302, https://doi.org/10.1016/j.atmosenv.2015.12.038, 2016.

Yokelson, R. J., Goode, J. G., Ward, D. E., Susott, R. A., Babbitt, R. E., Wade, D. D., Bertschi, I., Griffith, D. W. T., and Hao, W. M.: Emissions of formaldehyde, acetic acid, methanol, and other trace gases from biomass fires in North Carolina measured by airborne Fourier transform infrared spectroscopy, J. Geophys. Res., 104, 30109–30125, https://doi.org/10.1029/1999JD900817, 1999.

Zhuang, Y., Fu, R., Santer, B. D., Dickinson, R. E., and Hall, A.: Quantifying contributions of natural variability and anthropogenic forcings on increased fire weather risk over the western United States, 9, 2021.

Chapter 4: Characterizing the Performance of a Compact BTEX Gas Chromatograph-Photoionization Detector for Near Real-Time Analysis and Field Deployment

This chapter is published as:

Frausto-Vicencio, Isis, Alondra Moreno, Hugh Goldsmith, Ying-Kuang Hsu, and Francesca M. Hopkins. 2021. "Characterizing the Performance of a Compact BTEX GC-PID for Near-Real Time Analysis and Field Deployment" Sensors 21, no. 6: 2095. https://doi.org/10.3390/s21062095

Abstract

In this study, we test the performance of a compact gas chromatograph with photoionization detector (GC-PID) and optimize the configuration to detect ambient (sub-ppb) levels of benzene, toluene, ethylbenzene, and xylene isomers (BTEX). The GC-PID system was designed to serve as a relatively inexpensive (~$10k) and field-deployable air toxic screening tool alternative to conventional benchtop GCs. The instrument uses ambient air as a carrier gas, and consists of a Tenax-GR trap preconcentrator, a gas sample valve, two capillary columns, and a photoionization detector (PID) with a small footprint and low power requirement. The performance of the GC-PID has been evaluated in terms of system linearity and sensitivity in field conditions. The BTEX-GC system demonstrated the capacity to detect BTEX at levels as high as 500 ppb with a linear calibration range of 0-100 ppb. A detection limit lower than 1 ppb was found for all BTEX compounds with a sampling volume of 1 L. No significant drift in the instrument was observed. A time-varying calibration technique was established that requires minimal equipment for field operations and optimizes the sampling procedure for field measurements. With an analysis

time of less than 15 minutes, the compact GC-PID is ideal for field deployment of background and polluted atmospheres for near-real time measurements of BTEX. The results highlight the application of the compact and easily-deployable GC-PID for community monitoring and screening of air toxics.

4.1 Introduction

The volatile organic compound (VOC) family of benzene, toluene, ethylbenzene, and xylene isomers (BTEX) are air pollutants that can cause detrimental health effects and degrade air quality through oxidation reactions (Calvert et al., 2002; WHO, 2018). BTEX compounds are monocyclic aromatics and are grouped together because of similarities in their structures, properties, and emission sources (ATSDR, 2004). BTEX compounds are emitted as byproducts of combustion of fossil fuels and biomass, including motor vehicles and wildfires, and through volatilization from crude oil or its derivatives, including gasoline and industrial solvents (Bretón et al., 2017; Koss et al., 2018; Marrero et al., 2016; O'Dell et al., 2020). BTEX compounds are classified as hazardous air pollutants (HAPs) and are regulated by a large number of agencies worldwide including the United States Environmental Protection Agency (US EPA) and the California Air Resources Board (CARB) (Houghton et al., 1999; Sekar et al., 2019).

Among the BTEX family, benzene is the most dangerous as it is a well-known carcinogen and may have adverse health effects on immune, metabolic, respiratory functioning as well as on development (ATSDR, 2021a; Bolden et al., 2015, 2018; Wilbur et al., 2008). Ethylbenzene has been classified as a possible carcinogen, while toluene and xylene isomers can cause damage to the brain and central nervous system with long term

exposure (ATSDR, 2021b; Bolden et al., 2015). BTEX is ubiquitous in the environment at trace levels ranging from sub-ppb to tens of ppb in urban and industrial areas where atmospheric mixing ratios are higher (Baker et al., 2008; Bretón et al., 2017; Gilman et al., 2013; Karl et al., 2009; Liu et al., 2009; Weisel, 2010a; Zeng et al., 2019). Although ambient atmospheric BTEX levels have dropped due to reformulation of gasoline (Sultana & Hoover, 2018), there is evidence of an increase of emissions from oil and natural gas operations (Halliday et al., 2016; Propper et al., 2015). As wildfire events become more common with climate change, exposure to BTEX may increase in rural areas (Dickinson et al., 2020; USGCRP, 2018).

Monitoring of BTEX atmospheric background levels requires instrumentation that is sensitive to sub-ppb levels (Liu et al., 2009; Weisel, 2010b). Current techniques for measuring BTEX include ultraviolet (UV) spectroscopy, infrared (IR) spectroscopy, and gas chromatography (GC) coupled either to a flame ionization detector (FID), photoionization detector (PID) or to a mass spectrometer (MS) (Liaud et al., 2014; Parsons et al., 2011; Scott et al., 2020; Young et al., 2011). Traditional methods require ambient air samples to be drawn into sorbent material or collected in evacuated stainless-steel canisters then transferred to the lab for further analysis. More recently, open path Fourier-transform infrared spectroscopy (FTIR) and proton transfer reaction-mass spectroscopy (PTR-MS) have allowed for near-real time analysis in the field (Sahu et al., 2016); however, these techniques are expensive to purchase and operate due to their need for support gases, power requirements, or large physical size, and hence are not ideal for long-term stationary or

mobile monitoring (Parsons et al., 2011; Sydoryk et al., 2010; Warneke et al., 2011; Yuan et al., 2020).

There is currently a need for more inexpensive, easy-to-operate screening methods to determine the presence of atmospheric BTEX levels, as elucidating the fine-scale spatial patterns of BTEX in populated areas can improve the accuracy of human exposure estimates for the surrounding communities and inform mitigation policy (Sekar et al., 2019). The California Assembly Bill 617 calls for community-focused monitoring in disadvantaged and highly impacted communities (AB-617, 2017). This bill and the existing technology have popularized the use of low-cost and inexpensive sensors to provide an accessible screening method for communities due to the accessible prices, portability, and compact sizes (e.g. Purple Air, Clarity, etc. for particulate matter pollution) (AB-617, 2017; Spinelle et al., 2017). Numerous inexpensive sensors for BTEX and VOCs have been designed (Jian et al., 2013; Lara-lbeas et al., 2019; Skog et al., 2019; Spinelle et al., 2017); however, very few have the combination of sub-ppb sensitivity, selectivity, and relative low cost needed for ambient air monitoring. See Spinelle et al., 2017 and Lara-Ibeas et al., 2019 for a summary of the latest laboratory prototypes and commercially available inexpensive BTEX sensors and GC's (Lara-lbeas et al., 2019; Spinelle et al., 2017).

As a common inexpensive option, PID can be used as a standalone instrument to measure total hydrocarbon presence in real time. Although PIDs have great sensitivity, they are not selective and cannot speciate VOCs. Pairing a PID with a GC allows for speciation of BTEX compounds and lower detection limits. In this study, the performance of an ultra-compact GC-PID is characterized for detecting BTEX at sub-ppb levels. The

instrument configuration is optimized for separation of BTEX compounds. This analytical instrument was developed for operation in the field to be used as a screening tool for onsite and near-real time analysis. This design uses ambient air as the carrier gas to minimize the need for support gases and a calibration strategy is established that is simple and requires minimal equipment. The compact BTEX GC-PID system is composed of the following modules: sampling, preconcentration, separation, and detection described in the following sections (4.2.2). The instrument was characterized in a laboratory setting (4.3.1) and was tested in the field (4.3.8). Section 4.4 discusses findings and offers recommendations followed by concluding remarks in section 4.5.

4.2 Materials and Methods

4.2.1 Prototype of a compact BTEX GC-PID system

The compact BTEX GC-PID system is composed of the following modules: sampling, preconcentration, separation, and detection, further described in Section 4.2.2. The GC system was developed by SRI Instruments (Torrance, CA, USA) and is based on a simpler version of the commercial SRI BTEX GC-PID-FID with a built-in Method 5030 compliant purge and trap concentrator. The modified BTEX GC-PID design (Fig. 1) has the advantage of a reduced size and weight (SRI 110 chassis model) that allows it to be field-deployable and convenient for measurements. The instrument weighs 15 kg with dimensions 36.8 cm x 21.6 cm x 34.3 cm. It is designed for field deployment in background and polluted atmospheres with automatic sampling every 12-15 minutes. The GC-PID instrument operates in isothermal mode where the BTEX molecules separate without an oven temperature ramp. BTEX concentrations measured by the instrument are reported as

mixing ratios defined as the ratio of the mass of the respective BTEX compounds to the mass of dried air in a given volume.

A prototype GC was built by SRI Instruments and tested. Initially, the prototype was built with a distinct configuration to test for the desired sub-ppb limit of detection, selectivity, and separation for monitoring BTEX in ambient air. The column and backflush configurations tested is further discussed below. Ultimately, the configured system operates as follows: preconcentration of sample matrix on Tenax-GR material, separation by 15 m MXT-5 and 30 m MXT-1301 columns (Restek), followed by PID detection at 10.6 eV. Instrument parameters and settings are modified with the PeakSimple software downloadable on the SRI Instruments' website. The instrument operating principles are represented in the schematic shown in Fig. 2. Two instruments were tested with this configuration, which we henceforth refer to as GC1 and GC2.

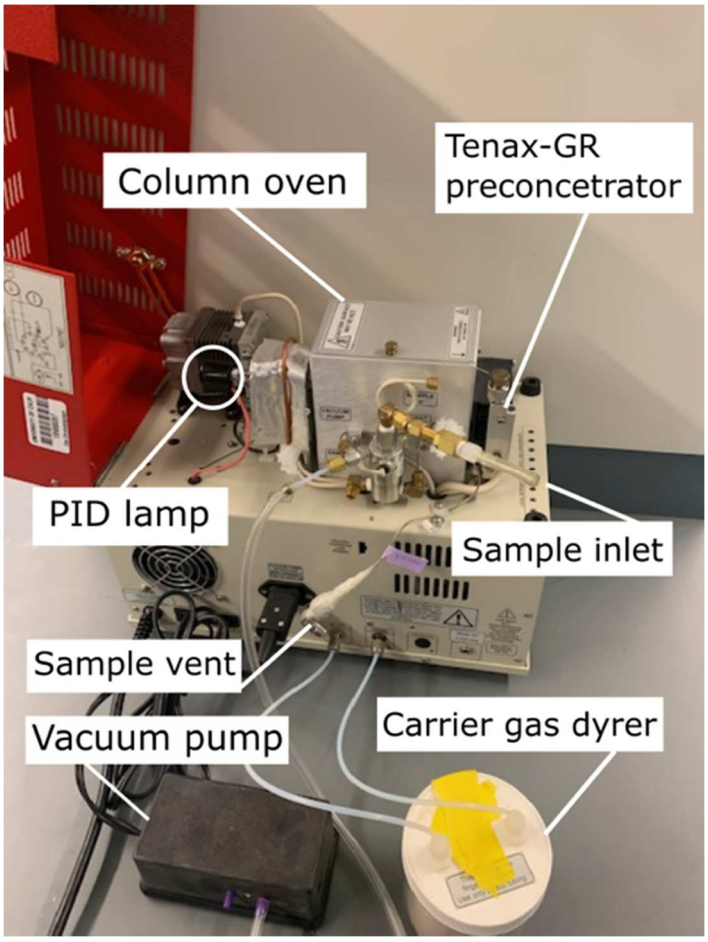

Figure 4.1. Side view of the compact BTEX GC-PID prototype. The system has an ultra-compact chassis (SRI 110 chassis model) weighing 15 kg with dimensions of 36.8 cm x 21.6 cm x 34.3 cm. The low weight and dimensions make it an ideal instrument for stationary or mobile field deployment and monitoring of BTEX molecules at the ppb level.

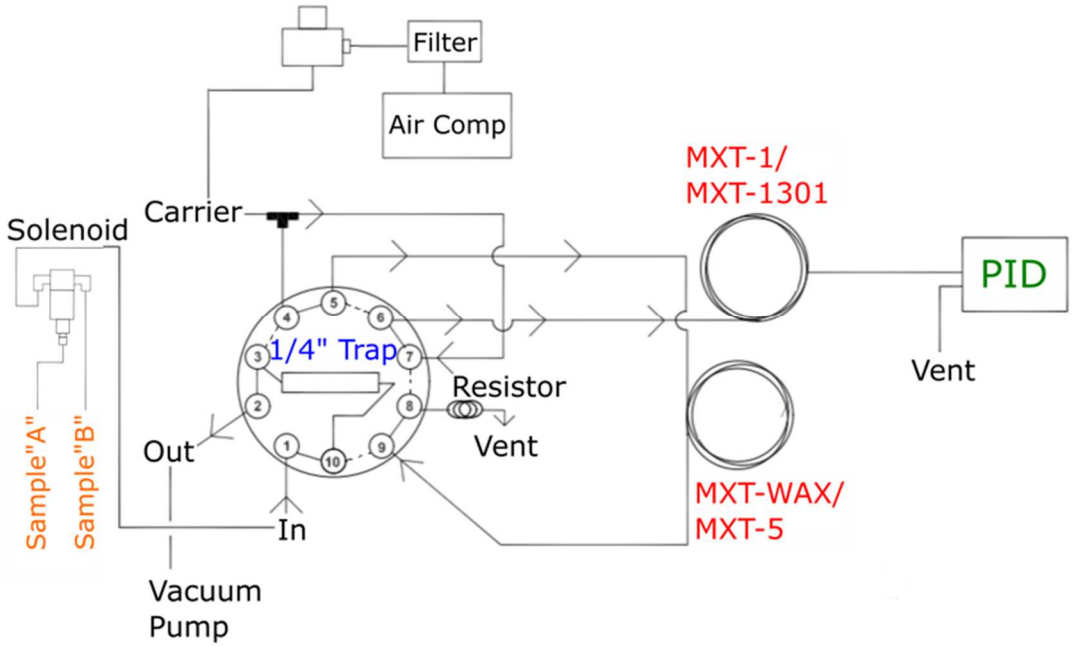

Figure 4.2. Schematic of the compact GC-PID system operating principle with 10-port valve in "load" position (shown as the solid lines) and "inject" position (shown in the dotted line) in a precolumn backflush configuration. Principal components of the different modules are shown in different colors: sampling (orange), preconcentration (blue), separation (red) and detection (green).

4.2.2 System integration and instrument operation

The instrument operating principles are represented in the schematic shown in Fig. 2 in a precolumn backflush configuration. When the valve is in "load" position, the vacuum pump pulls ambient air in through the solenoid (labeled "SOL) set to sample from inlet 1 (labeled "#1 IN"), which is directed to the Tenax-GR trap, then out to vent, loading the Tenax-GR trap with sample at the adsorption temperature (40 °C). Any sample not adsorbed to the Tenax-GR material is vented out through port 2 (labeled "#2 OUT VAC. PUMP"). The trap is heated to the desorption temperature (180 °C) shortly thereafter. At the same time, a carrier gas has been flowing through the columns at a constant flow rate defined by the electronic pressure controller. Once the trap reaches desorption temperature

(180 °C), the valve is actuated to “inject” position where the carrier gas is directed towards the trap sweeping desorbed analytes into the analytical columns (labeled “MXT-WAX/MXT-5” and “MXT-1/MXT-1301” in the diagram). The desorbed analytes are separated by boiling point before reaching the photoionization detector. The PeakSimple software displays a chromatogram in real time with automatic detection of peaks, integration and concentration calculation using a component and calibration file that has been saved prior to sampling. The BTEX molecules appear on the chromatograms based on their boiling point temperatures with benzene first followed by toluene, ethylbenzene, co-eluted meta- and para-xylenes (m,p-xylene) and finally ortho-xylene (o-xylene). The PeakSimple software allows the operator to modify instrument parameters and settings for desired sampling time, modification of event tables, calibration, and manual integration of peaks.

The sampling module consists of an aquarium vacuum pump that pulls the sample matrix into the preconcentrator trap (Fig. 1). The two brass inlets (1/8” (3.175 mm) female) are connected to a two-position solenoid valve that allows for alternating measurements between a calibration standard and an atmospheric sample. The two-inlet option can be used for faster sampling as the valve switches between loading a sample and finishing the previous loaded sample or a calibration gas standard. A plastic male barbed hose fitting with 1” Teflon tube was connected to the brass inlets for all experiments and calibrations conducted in this study.

The preconcentration module consists of a ¼” x 4 ½” (6.35 x 114.3 mm) stainless-steel cylinder packed with 0.5 g Tenax-GR material (2,6-diphenylene-oxide polymer

resin). A volume of gas is pulled through the solenoid valve by a vacuum pump into the Tenax-GR trap. This concentrates the desired volume of sample, trapping volatile organics while largely excluding water before loading the gas into the column. The amount of sample that may be loaded on to the trap is limited by the trap's adsorbent packing. How tightly packed the Tenax-GR trap is may affect the flow rate, thus flow rates for each instrument (GC1 and GC2) were determined to ensure the same sampling volume of 1 L. Sampling times of 1.75 minutes and 2.9 minutes were established for sampling 1 L volume for GC1 and for GC2, respectively. During trapping, ambient air or standard gases are flowed through the trap at 40 °C, until 1 L of this sample matrix has been passed through, depending on the flow rate through each instrument. The trap is then heated to an optimal temperature of 180 °C maintained for 4 mins to allow thermal desorption of BTEX molecules from the Tenax-GR material. The heating system consists of a thermocouple wire and aluminum block with a 100-watt cartridge heater wrapped around the Tenax-GR trap stainless steel tubing with a temperature ramp of 180 °C/minute. The trap is then cooled by a small fan within 3.45 minutes to 40 °C.

The separation module consists of two coupled columns heated in a small air-bath oven at 60 °C. The oven houses the two columns, a small fan, and a 10-port gas sampling valve (Fig.1) that connects the entire system further described in schematic shown in Fig. 2. The small fan circulates air inside the oven to keep an equal distribution of heat. A syringe injection port is included on the side of the oven wall to bypass the Tenax-GR trap, in cases when direct gas sampling is preferred.

Various column configurations and flushing methods were tested to optimize separation of BTEX with a stable baseline while maintaining a low cost for the GC measurement system. Table 1 describes the columns and flushing methods tested, labeled below as configuration a, b, and c.

- **Precolumn backflush to vent (configuration a & c):** This method captures heavier molecules in the precolumn and prevents them from entering the analytical column and reaching the detector. The backflush is carried out at a user defined time to reject water and other high boiling point analytes while the analytical column runs at a constant flow. This configuration has the advantage of the sample matrix having little influence on measurement, allows faster sampling time prevents late eluting compounds from interfering with the subsequent runs, and prevents water in the sample matrix from reaching the column.
- **Backflush to detector (configuration b):** This method bundles C6+ components that elute to the detector after the molecules of interest have passed through the analytical column. This method reduces analysis time and presents a summed total of C6+ molecules displayed in the chromatogram. It also prevents late eluting compounds from interfering with the subsequent runs.

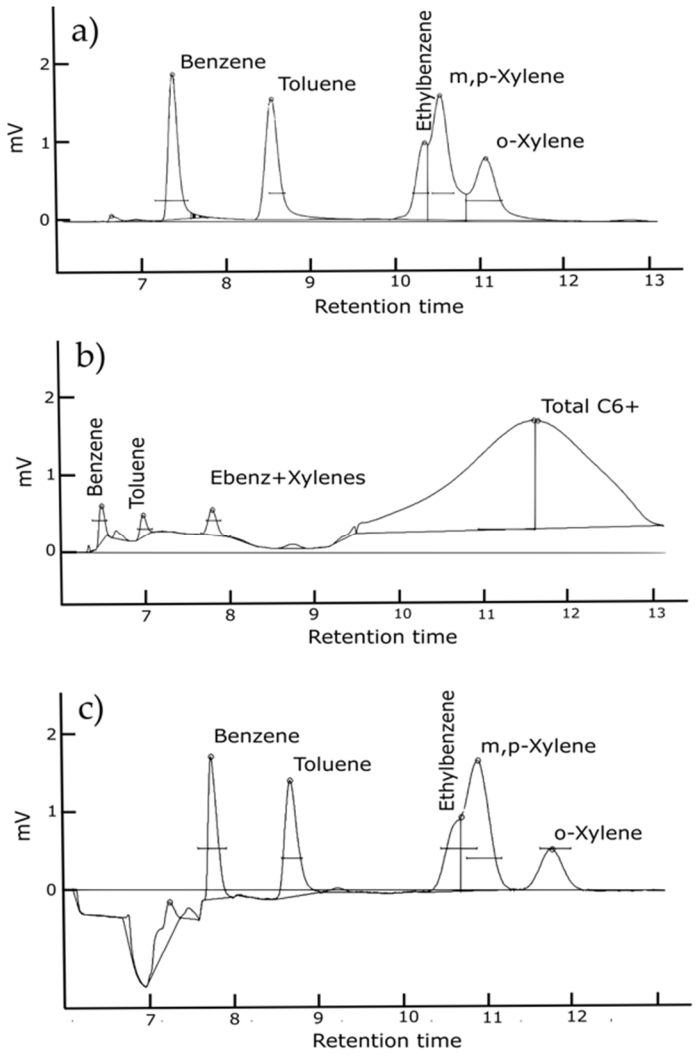

Figure 4.3. Sample chromatograms for three different column and flushing configurations with injection of a 1 ppb BTEX standard. Configurations: a) Separation of heavier BTEX compounds is challenging with the selected columns. b) Heavier hydrocarbons are detected; however, the baseline is not stable and separation of heavier BTEX compounds remains challenging. c) Better separation is observed in the o-xylene; however, separation of ethylbenzene and m,p-xylenes still remains challenging. The baseline shifts when the 10-port solenoid valve rotates, and the precolumn configuration is no longer in series with the analytical column. This causes the column flow to increase and the baseline to shift as seen in c).

Table 4.1. BTEX GC-PID descriptions for configuration a, b, and c. Configuration a and b had the same capillary columns with different backflushing method, while configuration c retained the precolumn backflushing method with new capillary columns. Only benzene and toluene limit of detections are show for comparison purposes.

Configuration	Capillary columns	Backflush Method	Analysis Time (min)	Limit of Detection (ppb)
a (Fig. 3 a)	15 m MXT-WAX 15 m MXT-1	Precolumn backflush	12	Benzene 0.09 Toluene 0.10
b (Fig. 3 b)	15 m MXT-WAX 15 m MXT-1	Backflush to detector	< 20	Benzene 0.37 Toluene 0.11
c (Fig. 3 c)	15 m MXT-5 30 m MXT-1301	Precolumn backflush	< 15	Benzene 0.06 Toluene 0.01

Configuration a and b operated with the precolumn, a 15-m polar phase (0.53 mm ID x 2.0 µm MXT-WAX) capillary column and a 15-m long nonpolar phase capillary (0.53 mm ID, 5.0 µm MXT-1) analytical column. The MXT-WAX column helps to remove water and VOC's other than BTEX. In this configuration, complete separation of the heavier BTEX compounds is challenging with the selected columns. This first configuration was optimized for separation of benzene; however, it did not entirely separate ethylbenzene and xylene isomers without needing an oven temperature ramp, as seen in Fig. 3a. Configuration b had the same columns as configuration a, but was plumbed to backflush to the detector. While the backflush to detector provided information on the number of hydrocarbons present in the sample, the baseline was not stable or consistent (Fig. 3b). This leads to uncertainties when integrating the area of each analyte peak. Thus, we retained the precolumn to detector plumbing. Configuration c was plumbed with capillary columns MXT-5 with 15 m length (0.53 mm ID x 0.25 µm) and MXT-1301 with 30 m length (0.53 mm ID x 0.3 um). The baseline proves to remain stable with a better

separation of the o-xylene, however separation of ethylbenzene and m,p-xylenes remains challenging (Fig. 3c). An oven temperature ramp is necessary to separate those two molecules; however, due to cost consideration the GC remained in isothermal mode with option c as the final configuration. Both GC1 and GC2 were sent back to the manufacturer to be configured with a precolumn backflush and capillary columns MXT-5 and MXT-1301.

Once molecules are separated within the analytical column, the carrier gas directs the analytes toward the detector. The BTEX GC-PID instruments are equipped with a PID detector (Andrews Glass) that responds to compounds whose ionization potential is below 10.6 eV, this includes aromatics and molecules with double carbons. This particular PID has a krypton discharge lamp that fragments the VOC's into negative and positive ions, the amplifier then measures the negative ions created by the lamp's UV energy at 121 nm.

4.2.3 Gas standards and carrier gas

A certified gas mixture composed of 1 ppm of each of the BTEX compounds (1 ppm of benzene, 1 ppm of toluene, 1 ppm of ethylbenzene, 1 ppm of m, p,-xylene and 1 ppm of o-xylene) purchased from Restek (± 5% uncertainty) and MESA Specialty Gases (± 10% uncertainty) were used for experiments performed in the laboratory. In addition, we used a gas mixture of about 1 ppb of each of the BTEX compounds from Apel-Reimer Environmental, Inc. (± 20% uncertainty), NIST-traceable certified, for the time-varying calibration method.

An internal air compressor provides the carrier gas from ambient air without the need for support gases (e.g. He, N2). The "Whisper Quiet" air compressor is built in the

chassis of the GC and controlled by an electronic pressure controller maintained at 9 PSI. The stream of air passes through the Sample Stream Dryer (SRI P/N 8690-0152) housing a Nafion permeable membrane dryer (Permapure P/N ME 110-24-COMP4) contained in the blue indicating molecular sieve to remove water vapor and other impurities from the ambient air carrier gas. The Nafion tube was cleaned as needed following the manufacturer's suggested procedure. The molecular sieve was heated regularly to the manufacturer's recommended temperature to remove moisture from the desiccant beads as they turned brown when saturated.

An experiment was conducted to determine the percent loss of humidity by passing a moist stream of air (62.6% relative humidity) through the Sample Stream Dryer. The Nafion dryer in molecular sieve significantly reduced the humidity to 32.3% in the air stream by close to 50% percent change. See section 4.3.6 for the effect of humidity on BTEX detection.

4.2.4 Calibration methods

Two calibration methods were explored with the GC system using the PeakSimple calibration tool. The first involved diluting 1 ppm BTEX standard with gas tight syringes and/or mass flow controllers in zero air within Tedlar bags. This method required 1000-fold dilution of the 1 ppm BTEX gas standard. This calibration method requires delicate analytical tools which are not ideal to use in the field, thus the second method was preferred and used to characterize the instrument.

The second method tested was the time-varying calibration method that takes advantage of the flexibility in the trap loading time to control the amount of sample

reaching the column and detector. This method relies on the fact that the sampling time on the Tenax-GR trap is linearly proportional to amount of sample loaded, and the area detected by the GC. The linearity of the calibration curve was explored to evaluate appropriate sampling volumes (and times) to cover the concentration range of interest (section 4.3.3). This time-varying method involves less equipment and is ideal for long-term field campaigns where a standard gas can be programmed for automated measurements.

4.2.5 Field deployments

We deployed the GC in a mobile platform by powering it with deep cycle marine batteries coupled to a pure sine inverter. Ambient air samples were drawn in from outside of the moving vehicle through Synflex tubing connected to the GC inlet. The GC draws a maximum of 130 W when the Tenax-GR trap is heated and 60-70 W when idle. For field measurements without the need of wall power, the system can be powered for more than 6 hours by deep cycle marine batteries connected in parallel to a pure sine wave inverter. A modified sine wave inverter was tested, and this method did not power the GC interior fans. The low power consumption makes it an ideal instrument for mobile measurements where power is limited.

For outdoor deployments, we used an OMEGA sensor to record pressure, humidity, and temperature (OMEGA OM-CP-PRHTEMP101A). A GPS tracker used for field deployments to match sampling times with location of site sampled.

4.3 Results

4.3.1 Instrument characterization

Several experiments were conducted to characterize and optimize the performance of the BTEX GC-PID instruments for the detection of ambient levels of BTEX expected to be ~1 ppb. We evaluated the performance by studying the following instrument parameters: linearity of the system, signal with sampled volume, calibration curve range, adsorption capacity of Tenax-GR material, instrument drift, and limit of detection in the sections below.

4.3.2 Linearity of the system

The detection range of the GC-PID system is limited by the adsorption capacity of the Tenax-GR trap in conjunction with the linear detection range of the PID lamp. The GC-PID system relies on the adsorption of BTEX molecules onto the Tenax-GR trap to preconcentrate the analytes for detection at trace levels. PID lamps have excellent sensitivity, detection limits and extensive linear detection ranges, but the latter begins to deviate at higher ppm levels. We test the linearity of the system as a whole with influences from both the Tenax-GR trap and PID detector to determine the maximum range of mixing ratios that is measurable with the instrument. We made a saturation curve by loading 1 L samples of BTEX with mixing ratios ranging from 20 to 5000 ppb (Fig. 4). We investigate the detection limit further described in Section 3.1.3.

Using a mass flow controller, a 1 ppm BTEX gas standard in zero air was diluted into Tedlar bags, and then were analyzed on the GC-PID to make the saturation curve. Prior to each measurement a trap blank was performed to ensure analytes are removed prior

to the next sample. The following concentrations were tested: 20, 38, 65, 100, 200, 400, 500, 750, 1000, 2500, 3000 and 5000 ppb (Fig. 4). We observed that BTEX peak areas are linear at low mixing ratios, but curve toward an asymptote at higher mixing ratios as seen for all analytes by 1000 ppb. This experiment demonstrates that for a sampling volume of 1 L, measurements up to 500 ppb can be made with confidence. Higher mixing ratios will be underestimated due to combined effect of detector linearity limitation and saturation of the Tenax-GR trap. We explore further the linearity of these curves in the next section (4.3.4) to further estimate a range of measurement accuracy.

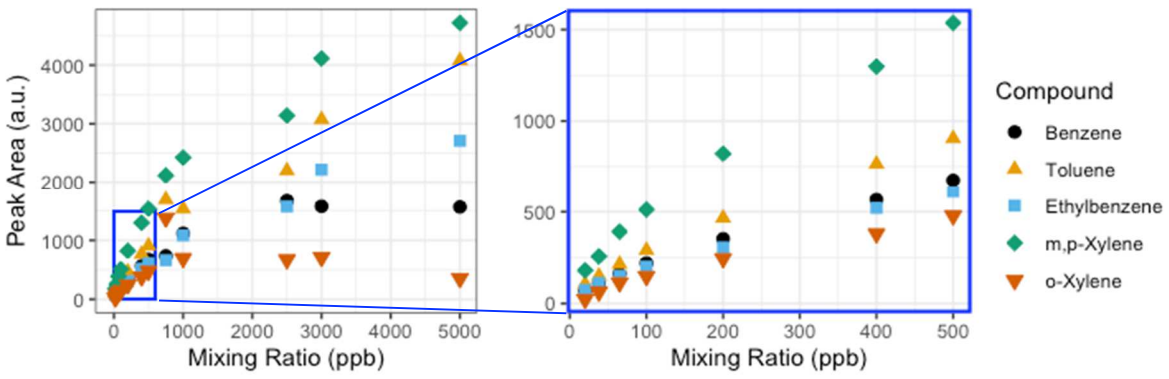

Figure 4.4. We evaluate the detection range of the BTEX GC-PID system by measuring a wide range of mixing ratios until an asymptote is reached. The detection linear range (0-500 ppb) is magnified highlighted by the blue box. The R^2 values for linear fits to each compound are all greater than 0.98.

4.3.3 Detector signal vs sample volume

We then evaluated the influence of varying sample volumes passing through the system to determine the range for the calibration curve using a time-varying method. At background, BTEX is expected to be below 1 ppb, while in the polluted atmospheric, mixing ratios vary greatly and can reach 10's to 100's of ppb. These experiments were

focused on expected ambient BTEX concentrations of 1 ppb. The gas standard composed of 1 ppb of each of the BTEX compounds was loaded onto the Tenax-GR trap while varying the sample volume from 1 to 10 L representing a concentration range of 0.5 ppb to 5 ppb BTEX on the trap. A cleaning step was performed after each analysis to remove any BTEX molecules from the Tenax-GR preconcentrator and prevent influence on the following sample. The cleaning step involved heating the Tenax-GR trap for 3 minutes at the end of the analysis to vent out desorbed analytes followed by cooling of the trap. Blank runs verified that BTEX was fully desorbed before the subsequent analysis. Conducting a cleaning step proved to be an effective method for removing the effects of carry-over from near-background and polluted samples of over 100 ppb. One cleaning step removed 87.1% of carry-over, two cleaning steps removed 92.9% and four cleaning steps removed 95.6% of carry-over. Due to the effectiveness of one cleaning step, we apply this to experiments presented in this study. Cleaning steps were conducted as trap blanks and chromatograms were visually verified for significant removal of carry-over.

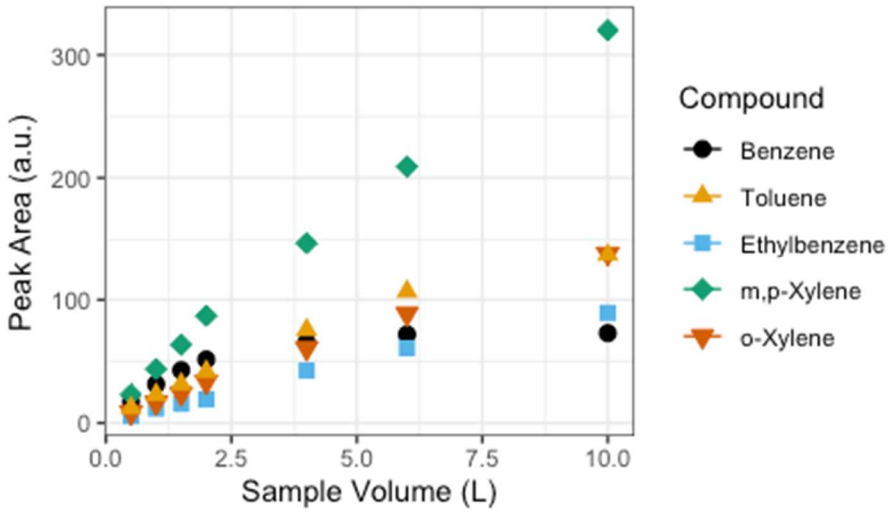

Figure 4.5. Linearity of detected signal to sampling volumes of BTEX compounds. Signal becomes saturated past 2 L, particularly evident for benzene. The error bars represent the standard deviation of the mean of triplicates of peak area. Note: error bars do not appear because they are smaller than the size of the symbol.

We found that past 2 L of sample volume the relationship between the benzene sample volume and instrument response ceases to be linear (Fig. 5). Both GC1 and GC2 showed the same behavior. Probable cause may be that the Tenax-GR trap gets saturated towards a large sample volume. However, linearity in benzene exists at the lower end of the sample volume (0.5, 1, 1.5 and 2 L) as seen in Fig. 5. For calibration purposes, we used volumes ranging from 0.5 to 2 L with 1 ppb BTEX gas standard corresponding to 0.5, 1, 2, 3 ppb that represent expected ambient BTEX mixing ratios. A 1 L sampling volume was determined to be adequate.

Once an adequate range was established for the calibration curve with the time-varying calibration method at the range where linearity exists (0.5 - 2 L), a straight-line calibration model is evaluated. According to the USEPA Method 8000, a straight-line

calibration model can be used when the standard deviation of the calibration factors is less than 20%. The percent standard deviation of the calibration factors (%SD) is shown in Table 2. All BTEX compounds pass the %SD test, therefore the "single line through origin (Ax) [average calibration factor]" method is applied to the experiments conducted in this study and an example is plotted in Fig. 6. The calibration equation, y = mx, where y is detector response (peak area), m is the average calibration factor, and the x is concentration of analyte. We performed the calibration measurements on three different days and calculated the calibration equation (Table 2). We observed no significant differences in calibration curves amongst days. We performed a two tailed t-Test assuming unequal variances of the peak areas. The p-values are greater than 0.05 between dates showing that the calibration equation has a less than 5% chance of being different.

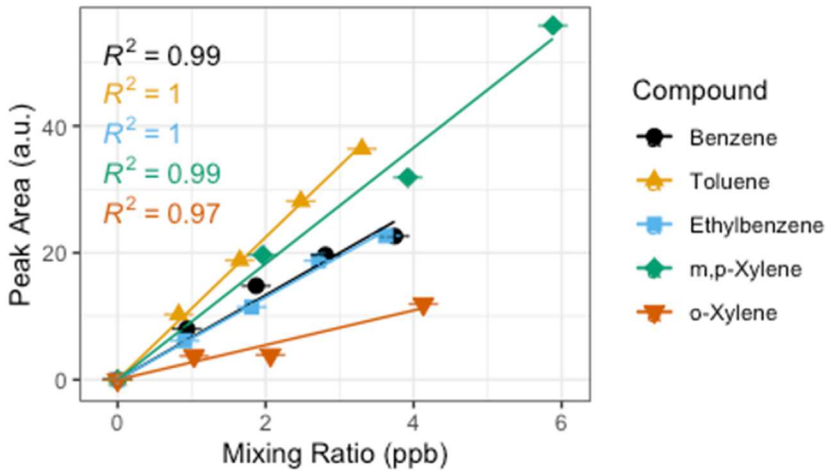

Figure 4.6. Example of calibration curves for BTEX compounds with the time-varying calibration method using sampling volumes: 0.5, 1.0, 1.5 and 2.0 L. The horizontal error bars represent uncertainty from the certified gas standard, while the vertical error bars (smaller than symbol) represent random instrument error. The corresponding R^2 is shown for each BTEX compound.

Table 4.2. Calibration curves for BTEX compounds. SD of slope indicates standard deviation of the slope in the calibration equation. A %SD lower than 20% indicates linearity exists in the calibration curve. N represents the number of points in the curve.

Compound	Date	Calibration equation	SD of slope	R^2	%SD	N
Benzene	2/22/20	y=7.38x	1.10	0.97	7.38	4
	2/24/20	y=5.60x	0.80	0.97	5.67	4
	2/27/20	y=6.87x	1.50	0.97	6.79	3
Toluene	2/22/20	y=11.56x	0.60	1.00	11.11	4
	2/24/20	y=10.99x	0.90	1.00	11.11	4
	2/27/20	y=10.95x	1.30	0.97	10.74	3
Ethylbenzene	2/22/20	y=6.57x	0.30	0.99	6.12	4
	2/24/20	y=5.25x	0.80	0.97	5.00	4
	2/27/20	y=7.18x	1.20	0.89	7.36	3
m,p-xylene	2/22/20	y=9.24x	1.00	0.96	9.35	3
	2/24/20	y=8.44x	0.80	0.98	8.33	4
	2/27/20	y=9.13x	1.60	0.91	9.36	3
o-Xylene	2/22/20	y=2.80x	0.90	0.90	2.89	4
	2/24/20	y=2.67x	0.70	0.99	2.68	3
	2/27/20	y=4.23x	1.10	0.98	4.26	3

4.3.4 Detection limit

Detection limits for each BTEX compound were determined based on analysis of 7 replicate samples of the 1 ppb BTEX gas standard (Table 3). The detection limit (DL) was defined as 3.143 times the standard deviation (SD) of the 7 replicates (DL = SD x 3.143) follow the recommended protocol from CARB (California Air Resources Board, 2018). The sample volume at which the detection limit was computed was at 1 L, which represents the volume at which field measurements will be taken. A 1 ppb BTEX sample was introduced into the GC inlet through a Tedlar bag, a cleaning step was done in between every run. The detection limit of the GC system depends on preconcentration of the sample. A lower limit of detection can be achieved by introducing larger sampling volumes; however as seen in Fig. 5, linearity may not hold beyond sample volumes of 2 L. With a 1 L sampling volume we achieve sub-ppb level detection limits on all compounds for both GC's.

4.3.5 System drift

Table 4. Drift experiments using a 1 ppb BTEX gas standard organized by date. Observed benzene reported in area units (a.u.). For dates where number of 1 ppb gas standard samples (N) were > 1, the standard deviation is shown in parentheses.

Table 4.3. BTEX detection limits for each BTEX GC-PID instrument referred to as GC1 and GC2.

Compound	GC1 (ppb)	GC2 (ppb)
Benzene	0.06	0.19
Toluene	0.10	0.28
Ethylbenzene	0.37	0.18
m,p-Xylene	0.33	0.32
o-Xylene	0.21	0.16

Table 4.4. Drift experiments using a 1 ppb BTEX gas standard organized by date. Observed benzene reported in area units (a.u.). For dates where number of 1 ppb gas standard samples (N) were > 1, the standard deviation is shown in parentheses.

Date	N	Benzene (a.u.)	
10/9/2019	7	13.51	(0.19)
11/25/2019	1	19.24	NA
1/7/2020	1	15.72	NA
1/14/2020	4	12.42	(0.11)
2/19/2020	1	16.92	NA
2/20/2020	3	14.94	(0.47)
2/22/2020	4	14.15	(0.51)
2/24/2020	1	10.65	NA
2/27/2020	1	13.59	NA
3/5/2020	3	11.45	(0.11)

4.3.6 Humidity effects

Water vapor and condensation is known to reduce PID lamp response, therefore relative humidity (RH) effects on detection signal were tested. In the first experiment, we explore the influence that moist carrier gas may have on the analyte detection signal by removing the Nafion dryer from the system. We measured the same BTEX gas standards with moist carrier gas and dry carrier gas. We find that a moist carrier gas reduces the peak areas by 39.5%, 31.9% and 67.6% for benzene, toluene, and ethylbenzene-xylenes, respectively. This experiment demonstrates the importance of drying the carrier gas and the effectiveness of the Nafion dyer for reducing water vapor interferences.

The second experiment was performed outdoors during a precipitation event where humidity levels were recorded to be higher than usual (Fig. 7). Ambient outdoor air was used as the carrier gas and dried as it passed through sample stream dryer (Nafion dryer in desiccant). We repeatedly measured the 1 ppb gas standard while using outdoor ambient air as a carrier gas. This experiment explored whether high humidity would affect detected signal isolating the influence of water vapor and possible condensation on the PID lamp. The measured RH ranged from 40% to 80%, pressure and temperature varied as well. A paired t-Test was performed on the measured concentrations pre-precipitation and post-precipitation event to test whether the rain events were significantly different. The t-test showed there was no statistically significant difference between pre- and post- rain event in measured benzene and toluene mixing ratios with two-tail p-values of 0.4255 and 0.0853, respectively. However, the t-Test showed statistically significant difference in ethylbenzene, m,p-xylenes and o-xylene measured before and after precipitation event with

two-tail p-values of 0.0133, 1.977 x 10-6, and 1.641 x 10-4. This indicates that humidity has a significant impact on the detection of ethylbenzene, m,p-xylenes and o-xylene.

4.3.7 Validation with Conventional canister sampling with laboratory analysis

To validate the performance of the BTEX GC-PID system, we compared the GC-PID measurements to the conventional approach of collecting air in canisters followed by measurement in the lab by a traditional benchtop GC. Two whole air samples were collected in an evacuated 2 L electropolished stainless steel canisters then returned to the University of California, Irvine for analysis of BTEX on a multicolumn, multidetector GC system in the laboratory further described elsewhere (Colman et al., 2001). Vehicle exhaust from a gasoline-powered car was collected with the whole air canister while the GC's were sampling at the same location. The canister was filled within 1 minute of opening the valve while the GC trapped the sample for 2 minutes. While it is difficult to compare the measured BTEX values because of this difference in timing of sample collection, BTEX measurements from canisters are bracketed by the measurements made by the field-deployable GC-PID system (Fig. 8). Although emissions of vehicle exhaust were not uniform in time, the slope of the non-benzene compounds to benzene in Fig. 8 are similar between both methods both measurement methods. The toluene to benzene (T/B) ratio was 1.76, within range of reported T/B literature values of close to 2 for traffic emissions in urban areas (Liu et al., 2009; Sahu et al., 2016). This gives confidence that the GC-PID instruments are not only capable of quick BTEX analyses, but also capable of measuring at high BTEX mixing ratios accurately before saturation occurs.

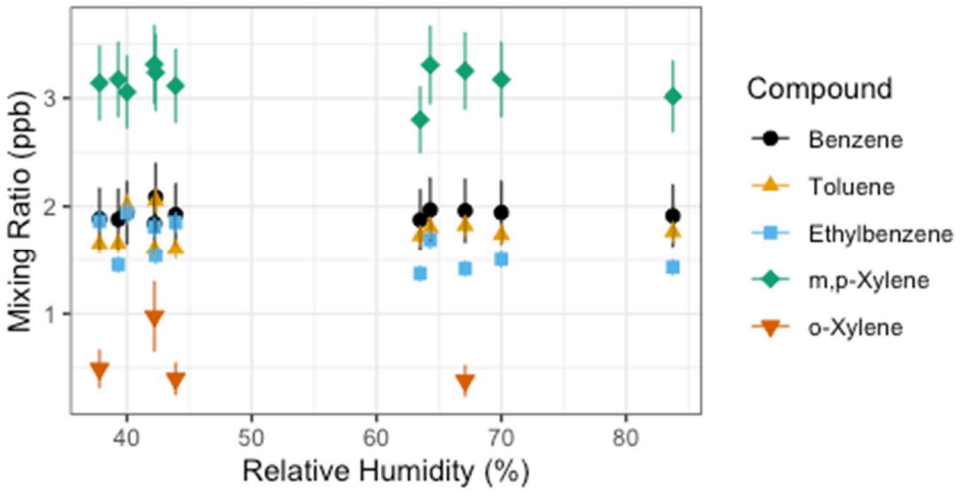

Figure 4.7. BTEX measured concentration of the 1 ppb gas standard. Measured pre-rain event relative humidity (RH) was 30-50%, while the post-rain event occurred during the increased relative humidity >50% RH. Error bars represent propagation of uncertainties from gas standard and random instrument error.

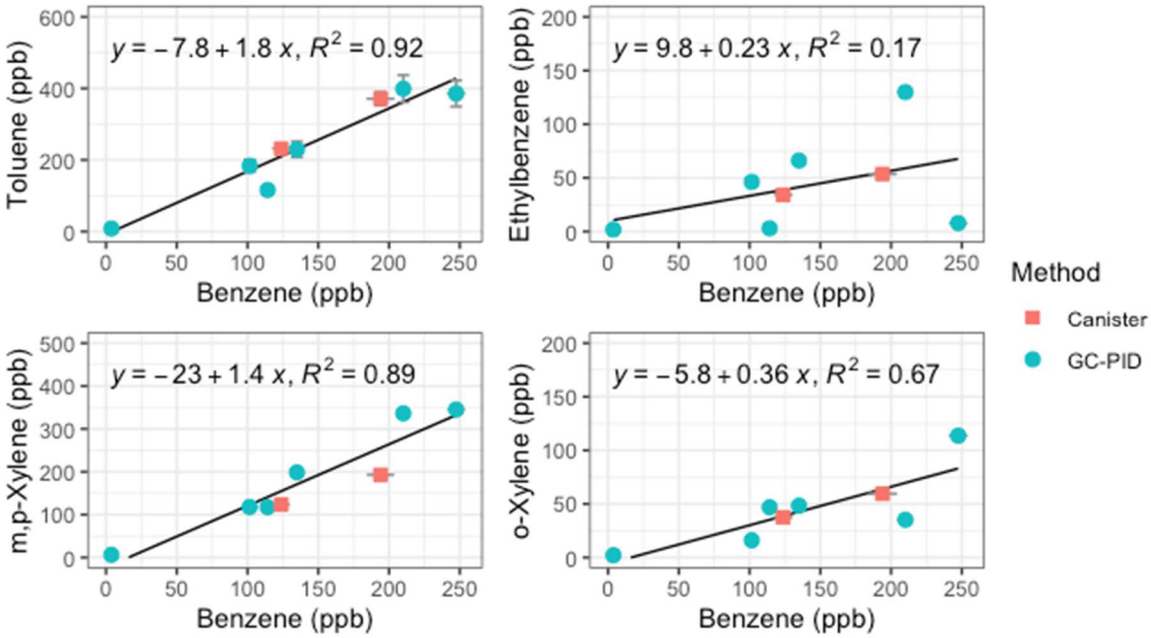

Figure 4.8. Regression plots of BTEX compounds from vehicle exhaust measured by the compact GC-PID instrument (blue) and samples collected in canisters (red) followed by analysis in a traditional benchtop GC. Error bars for the GC-PID are errors propagated from the calibration curve and error bars for the canister samples represent 5% precision accuracy from benchtop GC.

4.3.8 Mobile measurements of traffic emissions

The GCs were placed aboard a mobile platform to demonstrate the ability of the compact GC-PID to measuring environmentally relevant BTEX patterns in a field setting. Ambient outdoor samples were drawn in from outside through Synflex tubing connected to the GC inlet. On February 24th, 2020, we sampled ambient outdoor air with the GC before rush hour (15:00 to 16:00 PST) and during the afternoon rush hour (16:00 to 20:00 PST) at three locations: on the State Route (SR) 60, a heavily trafficked multi-lane highway in Riverside, California (24 samples); a local background measurement site location 6.5 km east of the SR-60 (9 samples); and at nearby gas stations (5 samples) as shown on Fig. 9. The local background site was chosen to be at a residential zone with minimum vehicle traffic and away from the major traffic source. Background measurements were taken before, during, and after the freeway transects to get an idea of the enhancement in BTEX produced by the afternoon rush hour. A GPS tracker was used alongside the GCs to measure location of measurements on and off the freeway.

We observed systematic differences between locations and over the course of the rush hour (Fig. 10). As expected, gas stations had the highest measured BTEX levels from evaporating fuels. Benzene was always higher at gas stations than on freeway or at the local background site, and other species tended to be higher at the gas station as well. On-freeway levels tended to be higher than background when comparing similar time periods, but the increase in emissions over the rush hour was larger than the differences between locations. BTEX mixing ratios increased as SR-60 became congested as the day progressed. A similar increase was observed at the background site, with roughly a

doubling of the benzene mixing ratio from the start of rush hour to the end (Fig. 10). We plotted the ratios benzene for on-freeway samples, and generally saw a strong, linear relationship between benzene and the toluene, ethylbenzene, and the xylene isomers, giving confidence that the emissions were emitted from the same source (Fig. 11). The observed T/B ratio for on-freeway measurements was 1.47. This value is lower than what has been observed in studies from urban traffic, but in accordance with observations of a lower value when a strong diesel contribution is present (Li et al., 2017). The SR-60 is a main route for diesel trucks transporting goods to and from warehouses in the area.

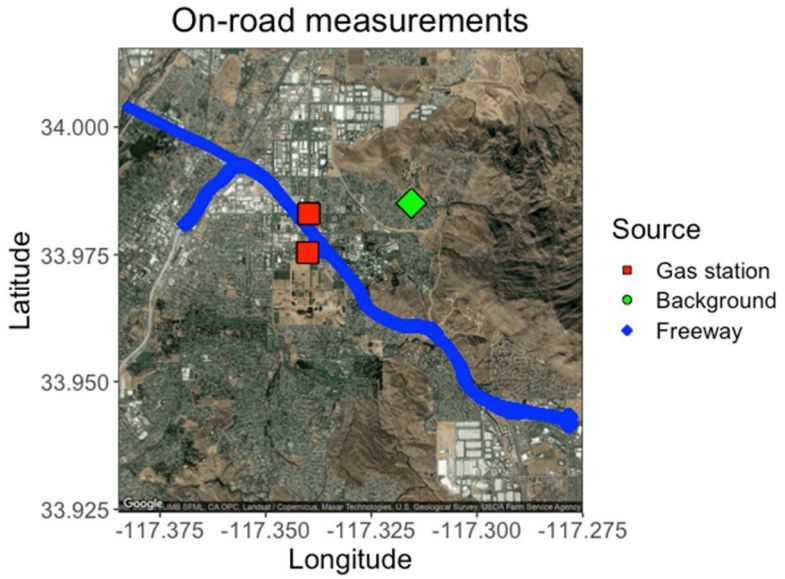

Figure 4.9. Map of freeway route on SR-60 with targeted gas stations and the local background measured 6.5 km east of the SR-60.

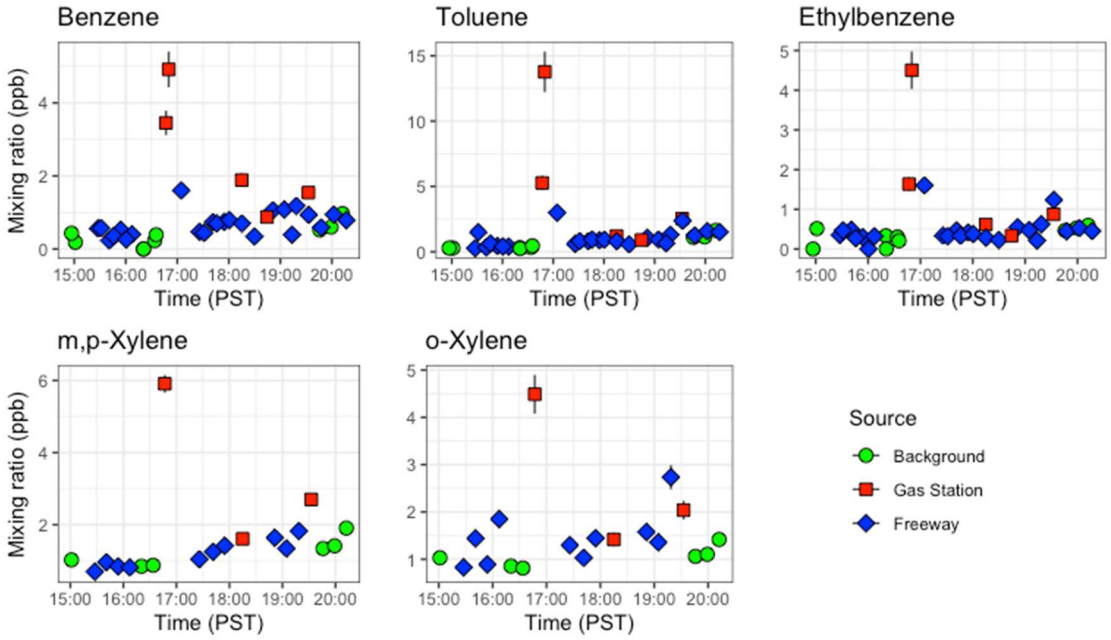

Figure 4.10. Timeseries of BTEX compounds detected by both GC1 and GC2 abroad a mobile platform before rush hour (15:00 to 16:00 PST) and during the afternoon rush hour (16:00 to 20:00 PST). These results show the portability of the compact GC-PID for mobile applications. Error bars represent error propagated from instrument calibration.

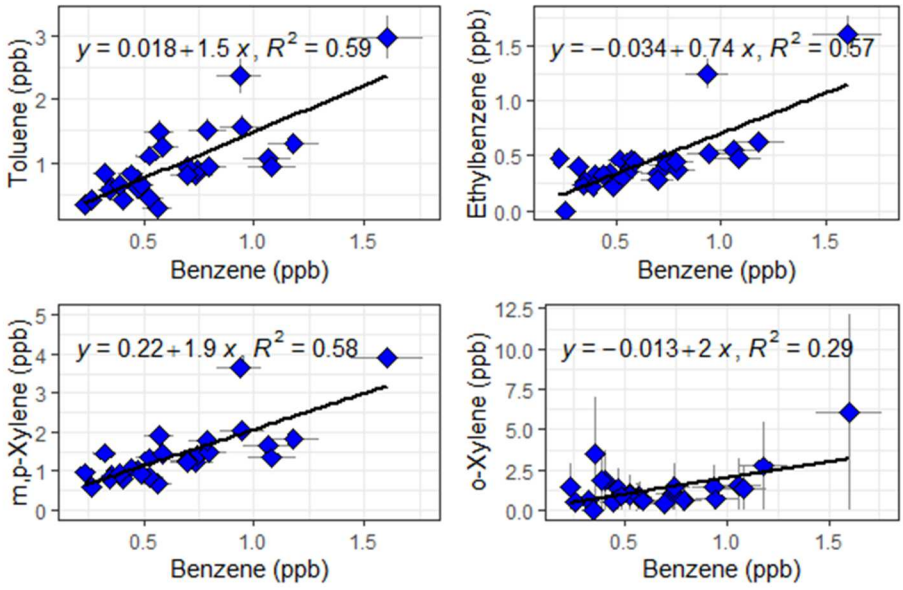

Figure 4.11. Benzene ratios for on-freeway emissions measured by GC1 and GC2 shown with a linear regression fit.

4.4 Discussion

In this study, we demonstrated the capability of a small field-deployable GC-PID for measurements of ambient BTEX levels in field and mobile campaign settings. Although the compact build of the instrument allows for portability that is ideal for field measurements and screening analysis, there are disadvantages to having a small instrument footprint. The chassis can only accommodate a small oven, thus limiting column diameter and temperature programming. The BTEX compounds have a wide range of boiling point temperatures (80 to 138 °C), while the isothermal oven was set to 60 °C. The oven was set closer to the benzene boiling point temperature, explaining why the heavier molecules are slow to elute and have broader peaks. A longer column gives better separation; however, the size of the oven limits the length and diameter of a column. Temperature programming was not included in this design due to added cost estimated at $5,000.

Toxic VOC's in urban air are of low concentration in often complex mixtures. Compounds with a similar structure as benzene (cyclopentane, pentane and cyclohexane) may show up as a small peak before benzene in the chromatogram. In our experiments, small unknown peaks were observed before the benzene peak. This becomes a concern when measuring polluted atmospheres because the area under the peaks can merge, resulting in a loss of the ability to resolve benzene. In addition, when higher mixing ratios are measured, carry-over from the previous sample is observed to influence the subsequent measurement. Regular heating of the trap is recommended to remove adsorbent from the trap. Tenax-GR material is commonly used as the adsorbent material for preconcentration

of BTEX, but other studies have shown that basolite C300 and ZSM-5 zeolites can be a more effective adsorbent material (Lara-lbeas et al., 2019; Megias-Sayago et al., 2020).

Using ambient air as the carrier gas is convenient for field measurements because it decreases the need for support gases. However, He and N_2 are more efficient at pushing molecules through the capillary columns and give a better separation of peaks in the chromatogram. We use ambient air as the carrier gas because it avoids the use of support gases that need constant replacement. The purity of the carrier gas is another important factor to consider, such as presence of VOC's and water vapor. The Tenax-GR trap amplifies the amount of BTEX in the sample, thus when measuring in polluted atmospheres, BTEX in the carrier gas would be of a negligible amount compared to that reaching the detector desorbed off the trap. Any contamination would show up as a constant background and not as a peak. However, an addition of a carbon trap can help reduce VOC impurities in the carrier gas which can be explored in future studies (Sorrels et al., 2018). Humidity has been shown to decrease the detected BTEX signal (You et al., 2020). We used several preventative measures in the design of the GC to remove water influence, such as: trap desorption to remove water in the sample, the precolumn backflush and the Nafion dryer which significantly decreases the amount of water in the sample. These measures all prevent water from reaching the detector; however, we saw that high humidity does indeed reduce the signal detected of ethylbenzene, m,p-xylene and o-xylene. Additionally, saturation of desiccant can affect the amount of water being removed from the stream of air. Daily calibrations done in the field include these uncertainties introduced by relative humidity and other environmental factors.

4.5 Conclusions

This study characterized the performance of a small field-deployable GC as a BTEX screening tool in the field at near-real time measurements. Working closely with the manufacturer we were able to optimize the configuration for speciation of the BTEX compounds and detect at the expected atmospheric background levels. Monitoring of BTEX background levels requires instrumentation that is sensitive to ppb or sub-ppb levels. We demonstrate the detection range of the compact GC-PID to be below 1 ppb for all BTEX compounds and up to 500 ppb. Compared to other commercial systems available and laboratory prototypes, the BTEX GC-PID performs remarkably well.

Three configurations were tested to determine the best selectivity and sensitivity. Two column configurations and flushing methods were explored: precolumn backflush method and backflush to detector. We observed a more stable baseline with the precolumn backflush; thus, we retained the precolumn to detector plumbing with capillary columns MXT-5 with 15 m length (0.53 mm ID x 0.25 μm) and MXT-1301 with 30 m length (0.53 mm ID x 0.3 um). This strategy allows for minimal equipment and relies on ambient air as the carrier gas. We show that linear calibrations can be achieved within 0-100 ppb using the single line through origin (Ax) calibration method on PeakSimple. When expected concentrations are above this range, a non-linear method can be applied, when there are enough data points present to accurately describe the curve.

We demonstrate that the compact design of this GC-PID is ideal for field screening and testing. The design presents the opportunity to screen for BTEX at a higher spatial resolution with possibility of establishing dense networks of VOC measurements. Field-

deployable GCs have the potential to aid in emergency air quality responses (e.g. refinery fires) and give near real-time air pollution measurements. Low-cost and inexpensive GCs offer an exciting alternative to conventional bench-top equipment accessibility allowing monitoring of pollutant with higher spatial resolution in impacted communities that can aid in air quality assessments in support of current regulations (e.g. Assembly Bill 617).

4.6 Acknowledgements

We acknowledge assistance in analyzing the flask samples from the Blake Laboratory at the University of California, Irvine. We thank Michelle Carr, Leoncio Lagarde, Neha Khushalani, and Kelly Perez for their help in data collection.

4.7 References

AB-617, Pub. L. No. AB-617 (2017). Retrieved from https://legiscan.com/CA/text/AB617/id/1642678

ATSDR. (2004). *Interaction Profile for: Benzene, Toluene, Ethylbenzene, and Xylenes (BTEX)*. Atlanta, GA, USA: Agency for Toxic Substances and Disease Registry.

ATSDR. (2021a). ATSDR - Toxic Substances - Benzene. Retrieved February 5, 2021, from https://www.atsdr.cdc.gov/substances/toxsubstance.asp?toxid=14

ATSDR. (2021b). ATSDR - Toxicological Profile: Toluene. Retrieved February 5, 2021, from https://www.atsdr.cdc.gov/toxprofiles/tp.asp?id=161&tid=29

Baker, A. K., Beyersdorf, A. J., Doezema, L. A., Katzenstein, A., Meinardi, S., Simpson, I. J., et al. (2008). Measurements of nonmethane hydrocarbons in 28 United States cities. *Atmospheric Environment*, *42*(1), 170–182. https://doi.org/10.1016/j.atmosenv.2007.09.007

Bolden, A. L., Kwiatkowski, C. F., & Colborn, T. (2015). New Look at BTEX: Are Ambient Levels a Problem? *Environmental Science & Technology*, *49*(9), 5261–5276. https://doi.org/10.1021/es505316f

Bolden, A. L., Schultz, K., Pelch, K. E., & Kwiatkowski, C. F. (2018). Exploring the endocrine activity of air pollutants associated with unconventional oil and gas extraction. *Environmental Health*, *17*(1), 26. https://doi.org/10.1186/s12940-018-0368-z

Bretón, J. G. C., Bretón, R. M. C., Ucan, F. V., Baeza, C. B., Fuentes, M. de la L. E., Lara, E. R., et al. (2017). Characterization and Sources of Aromatic Hydrocarbons (BTEX) in the Atmosphere of Two Urban Sites Located in Yucatan Peninsula in Mexico. *Atmosphere*, *8*(12), 107. https://doi.org/10.3390/atmos8060107

California Air Resources Board. (2018). *Laboratory Quality Control Manual*. Sacramento, CA, USA. Retrieved from https://ww2.arb.ca.gov/sites/default/files/2021-01/nlbqcm%20with%20addendum.pdf

Calvert, J. G., Atkinson, R., Becker, K. H., Kamens, R. M., Seinfeld, J. H., Wallington, T. H., & Yarwood, G. (2002). *The Mechanisms of Atmospheric Oxidation of the Aromatic Hydrocarbons*. Oxford, UK: Oxford University Press.

Colman, J. J., Swanson, A. L., Meinardi, S., Sive, B. C., Blake, D. R., & Rowland, F. S. (2001). Description of the Analysis of a Wide Range of Volatile Organic

Compounds in Whole Air Samples Collected during PEM-Tropics A and B. *Analytical Chemistry*, *73*(15), 3723–3731. https://doi.org/10.1021/ac010027g

Dickinson, G., Bajracharya, A., Durbin, T. A., McGarry, J. K., Miller, D. D., Moser, E. P., et al. (2020, December). *Ground-Based Measurements of Volatile Organic Compounds in Wildfire Smoke during FIREX-AQ Campaign*. Poster presented at the AGU Fall Meeting 2020, Online.

Gilman, J. B., Lerner, B. M., Kuster, W. C., & de Gouw, J. A. (2013). Source Signature of Volatile Organic Compounds from Oil and Natural Gas Operations in Northeastern Colorado. *Environmental Science & Technology*, *47*(3), 1297–1305. https://doi.org/10.1021/es304119a

Halliday, H. S., Thompson, A. M., Wisthaler, A., Blake, D. R., Hornbrook, R. S., Mikoviny, T., et al. (2016). Atmospheric benzene observations from oil and gas production in the Denver-Julesburg Basin in July and August 2014. *Journal of Geophysical Research: Atmospheres*, *121*(18), 11,055-11,074. https://doi.org/10.1002/2016JD025327

Houghton, M., Dodge, D., Krieger, R., Johnson, Jackie, Mazur, L., & Pomales, T. (1999). *Update to the Toxic Air Contaminant List* (p. 44). Sacramento, CA, USA: California Air Resources Board.

Jian, R.-S., Huang, Y.-S., Lai, S.-L., Sung, L.-Y., & Lu, C.-J. (2013). Compact instrumentation of a μ-GC for real time analysis of sub-ppb VOC mixtures. *Microchemical Journal*, *108*, 161–167. https://doi.org/10.1016/j.microc.2012.10.016

Karl, T., Apel, E., Hodzic, A., Riemer, D. D., Blake, D. R., & Wiedinmyer, C. (2009). Emissions of volatile organic compounds inferred from airborne flux measurements over a megacity. *Atmospheric Chemistry and Physics*, *9*(1), 271–285. https://doi.org/10.5194/acp-9-271-2009

Koss, A. R., Sekimoto, K., Gilman, J. B., Selimovic, V., Coggon, M. M., Zarzana, K. J., et al. (2018). Non-methane organic gas emissions from biomass burning: identification, quantification, and emission factors from PTR-ToF during the FIREX 2016 laboratory experiment. *Atmospheric Chemistry and Physics*, *18*(5), 3299–3319. https://doi.org/10.5194/acp-18-3299-2018

Lara-lbeas, I., Rodríguez-Cuevas, A., Andrikopoulou, C., Person, V., Baldas, L., Colin, S., & Le Calvé, S. (2019). Sub-ppb Level Detection of BTEX Gaseous Mixtures with a Compact Prototype GC Equipped with a Preconcentration Unit. *Micromachines*, *10*(3), 187. https://doi.org/10.3390/mi10030187

Li, B., Ho, S. S. H., Xue, Y., Huang, Y., Wang, L., Cheng, Y., et al. (2017). Characterizations of volatile organic compounds (VOCs) from vehicular emissions at roadside environment: The first comprehensive study in Northwestern China. *Atmospheric Environment*, *161*, 1–12. https://doi.org/10.1016/j.atmosenv.2017.04.029

Liaud, C., Nguyen, N. T., Nasreddine, R., & Le Calvé, S. (2014). Experimental performances study of a transportable GC-PID and two thermo-desorption based methods coupled to FID and MS detection to assess BTEX exposure at sub-ppb level in air. *Talanta*, *127*, 33–42. https://doi.org/10.1016/j.talanta.2014.04.001

Liu, J., Mu, Y., Zhang, Y., Zhang, Z., Wang, X., Liu, Y., & Sun, Z. (2009). Atmospheric levels of BTEX compounds during the 2008 Olympic Games in the urban area of Beijing. *Science of The Total Environment*, *408*(1), 109–116. https://doi.org/10.1016/j.scitotenv.2009.09.026

Marrero, J. E., Townsend-Small, A., Lyon, D. R., Tsai, T. R., Meinardi, S., & Blake, D. R. (2016). Estimating Emissions of Toxic Hydrocarbons from Natural Gas Production Sites in the Barnett Shale Region of Northern Texas. *Environmental Science and Technology*, *50*(19), 10756–10764. https://doi.org/10.1021/acs.est.6b02827

Megias-Sayago, C., Lara-Ibeas, I., Wang, Q., Le Calvé, S., & Louis, B. (2020). Volatile organic compounds (VOCs) removal capacity of ZSM-5 zeolite adsorbents for near real-time BTEX detection. *Journal of Environmental Chemical Engineering*, *8*(2), 103724. https://doi.org/10.1016/j.jece.2020.103724

O'Dell, K., Hornbrook, R. S., Permar, W., Levin, E. J. T., Garofalo, L. A., Apel, E. C., et al. (2020). Hazardous Air Pollutants in Fresh and Aged Western US Wildfire Smoke and Implications for Long-Term Exposure. *Environmental Science & Technology*, *54*(19), 11838–11847. https://doi.org/10.1021/acs.est.0c04497

Parsons, M. T., Sydoryk, I., Lim, A., McIntyre, T. J., Tulip, J., Jäger, W., & McDonald, K. (2011). Real-time monitoring of benzene, toluene, and p-xylene in a photoreaction chamber with a tunable mid-infrared laser and ultraviolet differential optical absorption spectroscopy. *Applied Optics*, *50*(4), A90–A99. https://doi.org/10.1364/AO.50.000A90

Propper, R., Wong, P., Bui, S., Austin, J., Vance, W., Alvarado, Á., et al. (2015). Ambient and Emission Trends of Toxic Air Contaminants in California. *Environmental Science & Technology*, *49*(19), 11329–11339. https://doi.org/10.1021/acs.est.5b02766

Sahu, L. K., Pal, D., Yadav, R., & Munkhtur, J. (2016). Aromatic VOCs at Major Road Junctions of a Metropolis in India: Measurements Using TD-GC-FID and PTR-

TOF-MS Instruments. *Aerosol and Air Quality Research*, *16*(10), 2405–2420. https://doi.org/10.4209/aaqr.2015.11.0643

Scott, P. S., Andrew, J. P., Bundy, B. A., Grimm, B. K., Hamann, M. A., Ketcherside, D. T., et al. (2020). Observations of volatile organic and sulfur compounds in ambient air and health risk assessment near a paper mill in rural Idaho, U. S. A. *Atmospheric Pollution Research*, *11*(10), 1870–1881. https://doi.org/10.1016/j.apr.2020.07.014

Sekar, A., Varghese, G. K., & Ravi Varma, M. K. (2019). Analysis of benzene air quality standards, monitoring methods and concentrations in indoor and outdoor environment. *Heliyon*, *5*(11), e02918. https://doi.org/10.1016/j.heliyon.2019.e02918

Skog, K. M., Xiong, F., Kawashima, H., Doyle, E., Soto, R., & Gentner, D. R. (2019). Compact, Automated, Inexpensive, and Field-Deployable Vacuum-Outlet Gas Chromatograph for Trace-Concentration Gas-Phase Organic Compounds. *Analytical Chemistry*, *91*(2), 1318–1327. https://doi.org/10.1021/acs.analchem.8b03095

Sorrels, J. L., Baynham, A., Randall, D. D., & Schaffner, K. S. (2018). Chapter 1 - Carbon Adsorbers. In *EPA Air Pollution Control Cost Manual* (7th Edition). Washington, D.C.: U.S. Environmental Protection Agency. Retrieved from https://www.epa.gov/sites/production/files/2018-10/documents/final_carbonadsorberschapter_7thedition.pdf

Spinelle, L., Gerboles, M., Kok, G., Persijn, S., & Sauerwald, T. (2017). Review of Portable and Low-Cost Sensors for the Ambient Air Monitoring of Benzene and Other Volatile Organic Compounds. *Sensors*, *17*(7), 1520. https://doi.org/10.3390/s17071520

Sultana, D., & Hoover, S. (2018). *GASOLINE-RELATED AIR POLLUTANTS IN CALIFORNIA - TRENDS IN EXPOSURE AND HEALTH RISK, 1996 TO 2014* (p. 423). Sacramento, CA, USA: Office of Environmental Health Hazard Assessment.

Sydoryk, I., Lim, A., Jäger, W., Tulip, J., & Parsons, M. T. (2010). Detection of benzene and toluene gases using a midinfrared continuous-wave external cavity quantum cascade laser at atmospheric pressure. *Applied Optics*, *49*(6), 945–949. https://doi.org/10.1364/AO.49.000945

USGCRP. (2018). Fourth National Climate Assessment. Retrieved February 5, 2021, from https://nca2018.globalchange.gov

Warneke, C., Roberts, J. M., Veres, P., Gilman, J., Kuster, W. C., Burling, I., et al. (2011). VOC identification and inter-comparison from laboratory biomass burning using PTR-MS and PIT-MS. *International Journal of Mass Spectrometry*, *303*, 6–14. https://doi.org/10.1016/j.ijms.2010.12.002

Weisel, C. P. (2010a). Benzene exposure: An overview of monitoring methods and their findings. *Chemico-Biological Interactions*, *184*(1–2), 58–66. https://doi.org/10.1016/j.cbi.2009.12.030

Weisel, C. P. (2010b). Benzene exposure: An overview of monitoring methods and their findings. *Chemico-Biological Interactions*, *184*(1–2), 58–66. https://doi.org/10.1016/j.cbi.2009.12.030

WHO. (2018). *Benzene* (Vol. 120). International Agency for Research on Cancer.

Wilbur, S., Wohlers, D., Paikoff, S., Keith, L., & Faroon, O. (2008). ATSDR evaluation of health effects of benzene and relevance to public health. *Toxicology and Industrial Health*, *24*(6), 263–398. https://doi.org/10.1177/0748233708090910

You, D. W., Seon, Y. S., Jang, Y., Bang, J., Oh, J. S., & Jung, K. W. (2020). A portable gas chromatograph for real-time monitoring of aromatic volatile organic compounds in air samples. *Journal of Chromatography A*, *1625*, 461267. https://doi.org/10.1016/j.chroma.2020.461267

Young, C. R., Menegazzo, N., Riley, A. E., Brons, C. H., DiSanzo, F. P., Givens, J. L., et al. (2011). Infrared Hollow Waveguide Sensors for Simultaneous Gas Phase Detection of Benzene, Toluene, and Xylenes in Field Environments. *Analytical Chemistry*, *83*(16), 6141–6147. https://doi.org/10.1021/ac1031034

Yuan, H., Li, N., Linghu, J., Dong, J., Wang, Y., Karmakar, A., et al. (2020). Chip-Level Integration of Covalent Organic Frameworks for Trace Benzene Sensing. *ACS Sensors*, *5*(5), 1474–1481. https://doi.org/10.1021/acssensors.0c00495

Zeng, P., Guo, H., Cheng, H., Wang, Z., Zeng, L., Lyu, X., et al. (2019). Aromatic Hydrocarbons in Urban and Suburban Atmospheres in Central China: Spatiotemporal Patterns, Source Implications, and Health Risk Assessment. *Atmosphere*, *10*(10), 565. https://doi.org/10.3390/atmos10100565

Chapter 5: Summary and recommendations for future work

5.1 Summary of this work

This dissertation characterizes and quantifies greenhouse gases, air pollutants, and air toxics from major sources in California by using novel atmospheric trace gas monitoring systems.

In Chapter 2, X_{CH4} observations from the EM27/SUN ground-based solar spectrometer were used to estimate CH_4 emissions from dairy farms across seasons by using a simple mass balance technique. The mass balance method previously used by Chen et al., 2016 with EM27/SUN observations was improved by including the area of the source. Seasonality in CH_4 emissions was observed from study of a 10x10 km^2 dairy farm cluster, with highest emissions observed in the summer and winter. I explored specific meteorological variables that could be driving the seasonal differences and find that day-to-day variability in measured X_{CH4} is influenced by both winds and temperature, but wind speeds drive the differences across seasons more than temperature. The SJV dairy livestock were found to emit ~5 times more CH_4 than Southern California dairy farms, primarily due to the differences in animal waste management. Dry manure management practiced in Southern California produces less CH_4 than the flushing of animal waste to manure lagoons, a wet manure management practiced heavily in the SJV. Nevertheless, the EM27 technique was not precise enough to quantify expected CH_4 emission reductions due to installation of anaerobic digesters. Hence, we conclude that EM27/SUN differential columns measurements can be useful for exploring emissions differences amongst seasons

and dairying regions, but are likely not ideal for verifying the effectiveness of CH_4 mitigation strategies

In Chapter 3, I collected 2 months of atmospheric column observations during the 2020 wildfire period to derive, for the first time, emission factors with respect to CO_2 and modified combustion efficiency. These variables are commonly used in fire research to characterize fuel properties and combustion phases of wildfires. We measured the highest X_{CO} ever recorded with the EM27/SUN from a large smoke plume that originated from the Sequoia Lightning Fire Complex. I used the solar spectra to derive the AOD and compared our AOD:CO based ratios to those measured from space of fires observed across the U.S. I also compared X_{CO} ground-based observations to those of TROPOMI satellite and found the best coincident criteria during high X_{CO} and aerosol burden. Additionally, using field-based emission ratios I found that significant amounts of CH_4 was emitted by Sierra Nevada wildfires during the 2020 wildfire season.

Finally, in Chapter 4, I presented a newly designed and optimized portable GC-PID with capability of detecting and speciating the BTEX air toxics. Three configurations were tested to determine the best selectivity and sensitivity. I demonstrated through several in lab and field tests that the compact design of this GC-PID is ideal for stationary and mobile field campaigns in a variety of environmental conditions. The detection range of the compact GC-PID is below 1 ppb for all BTEX compounds and up to 500 ppb. Compared to other commercial systems available and laboratory prototypes, the BTEX GC-PID performs remarkably well.

5.2 Recommendations and future work

In Chapter 2, the seasonal study from the dairy farm cluster was limited to measurements collected during the daytime hours and for 1-2 weeks at a time. Further studies need to focus on collecting a longer time series to better understand the day-to-day variability, seasonal effects, and transition of emissions across seasons. Lingering questions remain of whether daily variability is stronger than seasonal effects. Long-term monitoring stations with instrument enclosures at a safe location can help answer this and other research questions. Additionally, rapid changes are occurring at the dairy farms in the SJV from changing animal feeds to installing digesters. Each farm operates in slightly different fashion, thus documenting these changes at the farm level is important as well as understanding how each change reflects in the emitted amounts of CH_4.

The 10 x10 km^2 cluster was a relatively small area to model that limited us to utilizing the mass balance technique instead of a transport model. Although real time wind measurements are better to use than modeled winds, the nature of the atmospheric column measurement is better described by mesoscale wind products that includes winds conditions in the upper atmosphere. We attempted to use the STILT model driven by wind products like the Weather Research and Forecasting (WRF) and High-Resolution Rapid Refresh (HRRR) model, however, these wind products added a lot of uncertainties for modeling a small area. Until improvements are made on these mesoscale wind products, versions like WRF-4dVar that use data assimilation to nudge results closer to reality can improve the modeling as well as creating our own wind fields over the small area and making assumptions that the winds are heterogenous during ideal conditions.

Possible research questions are posed below:

- Is daily variability in CH_4 from dairy farms due to changing wind speeds stronger than seasonal effects?
- Can the impact of management in feed or waste on CH_4 emissions across a dairy farm cluster be observed within the atmospheric column?
- What spatial scale is the EM27/SUN technique better to capture changes in CH_4 emissions (ex. 10's vs 100's km)?

In Chapter 3, the wildfire study was conducted during the COVID-19 shutdown that limited measurements to a single location. Future studies can focus on "chasing" wildfire plumes by following predictions of smoke transport based on NOAA's HRRR smoke product. This will increase the number of fire plumes measurements for determining a more accurate and representative emission factor of the temperate conifer forests in the Sierra Nevada or other vegetation types in the globe. Because the EM27/SUN measures at the scale of satellites, satellite derived emission factors can be validated with the EM27/SUN observations. This could enable spatial emission factors that inform how fuel properties and combustion phases are changing across space as a wildfire burns. Our emission factors were calculated for CH_4 and CO, but there is a lot of interest for emission factors for $PM_{2.5}$. Future studies can convert the FTIR-derived AOD to $PM_{2.5}$ to provide those emission factors (Handschuh et al., 2022). Further verification of the FTIR-derived AOD product can involve side-by-side measurements at an AERONET location. Also, a clean atmosphere is recommended for determining a more reliable ln(Vo) variable, thus future SJV measurements can dedicate 1-2 days of measurements in a pristine atmosphere

like the mountains in the Sierra Nevada. Current work is being done to improve CH_4 retrievals from the TROPOMI satellite. During high aerosol loading TROPOMI CH_4 has low data quality and limits the spatial observations of CH_4 from wildfires, thus future analysis can focus on comparisons between EM27/SUN and TROPOMI CH_4 during wildfires.

Possible future research questions are posed below:

- Does the vertically integrated emission factor represent the fuel properties of mixed vegetation?
- Can emission factors of $PM_{2.5}$ be calculated from the FTIR-derived AOD?
- How do satellite emission factors compare to emission factors derived with the EM27/SUN?

In Chapter 4, the GC-PID was extensively tested in the laboratory, but more field-based testing is required to determine the ideal conditions for sampling in a moving vehicle and the self-calibration method when in a long-term stationary site. Due to a 2-minute sampling time, if vehicle speed is not consistent across measurements sources cannot be compared directly to each other due to oversampling in slow speeds and diluting the source at higher speeds. The calibration method that was proposed in Chapter 4 utilized a time-varying method of standard concentration in Tedlar bags but requires personnel to refill the bags and change them out. When sampling for long periods of time in remote locations a self-calibration system would be ideal to conserve data quality. Future studies can monitor BTEX along with other trace gases like CH_4, CO_2, and CO. Recent studies have

shown elevated BTEX levels observed in CH_4 emission hotspots (Marrero et al., 2016), which are much easier to detect using techniques such as mobile and airborne surveys.

Possible research questions are posed below:

- Are CH_4 hotspots an appropriate proxy for BTEX sources?
- What are the fine-scale spatial and temporal patterns of BTEX and CH_4 at the neighborhood level?
- What are appropriate sampling strategies for mobile surveys and long-term stationary sampling of BTEX?

Appendix A1: Appendix to Solar column based CH_4 emission estimates of dairy farms at local scales in the San Joaquin Valley

A2.1 Tables

Table A Error! No text of specified style in document..**1** Summary of emissions rates calculated using a mass balance approach. Standard error of the mean is shown for gradients and mean emission rates.

Season	Date	Npts	ΔXCH_4 (ppb)	Mean E (Gg CH_4/yr)	BU E_{CH4} (Gg CH4/yr)	Scaling Factor	Downwind Configuration
Spring	3/25/19	41	10.1 ± 0.6	28.5 ± 2.4	15.5 ± 5.5	1.8 ± 0.2	B
	3/29/19	32	6.6 ± 0.9	27.7 ± 4.3	14.4 ± 5.1	1.9 ± 0.3	B
Summer	6/21/19	41	8.5 ± 1.5	37.7 ± 6	12.8 ± 4.6	2.9 ± 0.5	B
	6/22/19	60	5.9 ± 0.5	18.3 ± 1.6	12 ± 4.2	1.5 ± 0.1	A
	6/24/19	37	7.05 ± 3.1	49.8 ± 21.25	9.7 ± 3.4	5.5 ± 2.2	A
	6/26/19	69	12.1 ± 1.3	66.5 ± 6.6	11.5 ± 4.1	5.7 ± 0.6	A
	6/27/19	64	10.3 ± 0.6	68.2 ± 4.2	23 ± 8.2	3 ± 0.2	C
Fall	9/10/19	14	10.2 ± 1	38.4 ± 4.4	15 ± 5.3	2.5 ± 0.3	C
	9/11/19	59	7.1 ± 0.5	41 ± 2.8	22 ± 7.8	1.9 ± 0.1	C
	9/17/19	82	2.1 ± 0.3	13.4 ± 2.2	12.7 ± 4.5	1.1 ± 0.2	A
	9/19/19	59	2.7 ± 0.5	11.8 ± 2.0	12.3 ± 4.4	0.9 ± 0.2	A
Winter	1/23/20	33	21.4 ± 2.4	43.8 ± 6.8	12.5 ± 4.4	3.5 ± 0.5	A
	1/23/20	33	23.7 ± 3.1	52.3 ± 7.3	16.6 ± 5.7	3.2 ± 0.4	B
	1/28/20	30	8.7 ± 1	30.8 ± 4.2	9 ± 3.2	3.4 ± 0.5	A
	1/28/20	30	15.6 ± 0.9	43.9 ± 5.0	16.1 ± 5.7	2.7 ± 0.3	B
	1/31/20	10	5.9 ± 2.6	4.6 ± 2	8.8 ± 3.1	0.5 ± 0.2	A
	1/31/20	10	8.9 ± 2.4	7.0 ± 1.9	6 ± 2.1	1.1 ± 0.3	B
	2/2/20	38	15.9 ± 4.6	62.3 ± 20.6	16.4 ± 5.8	3.8 ± 1.3	B

A2.1 Figures

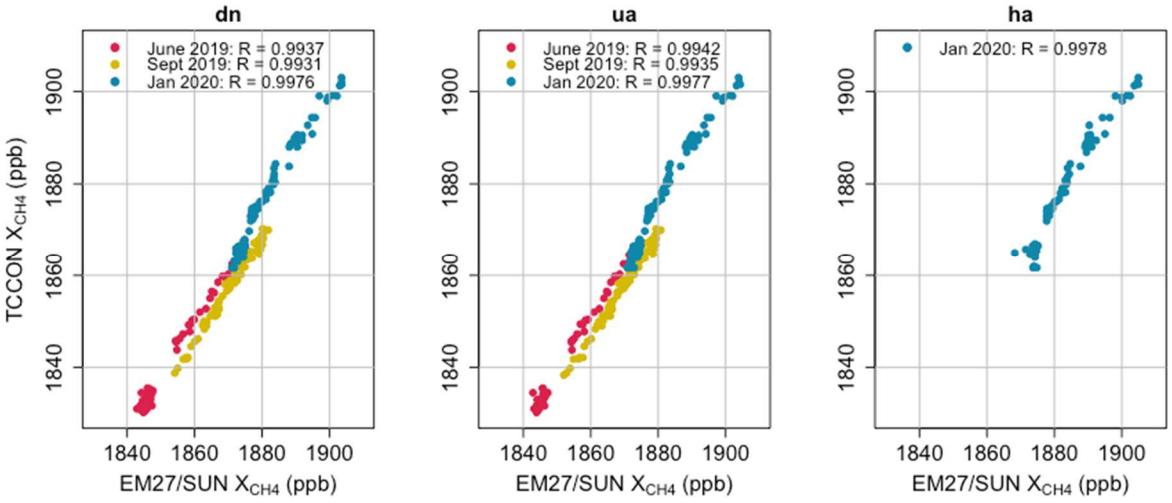

Figure A1.1 The EM27/SUN solar spectrometers dn, ua and ha were co-located with the higher spectral resolution TCCON instrument to ensure system stability before and after each field campaign and to tie our measurements to the WMO scale. The correction factor (R) is shown for each instrument and season. The averaging kernel was considered when comparing these two instruments.

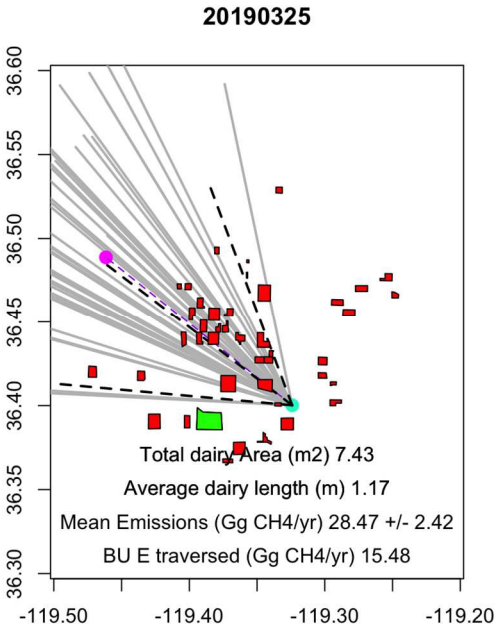

Figure Error! No text of specified style in document.**1.2** Example of mass balance technique. Locations of EM27 in magenta and cyan colors and 5-minute average wind directions in grey on March 25th, 2019. Schematic of wind vectors (grey) intersecting dairy farms (red) with dashed black lines representing

95% confidence interval of wind direction during measurement period. A mean emission of 28.5 ± 2.4 (SEM) was calculated.

March 29th, 2019

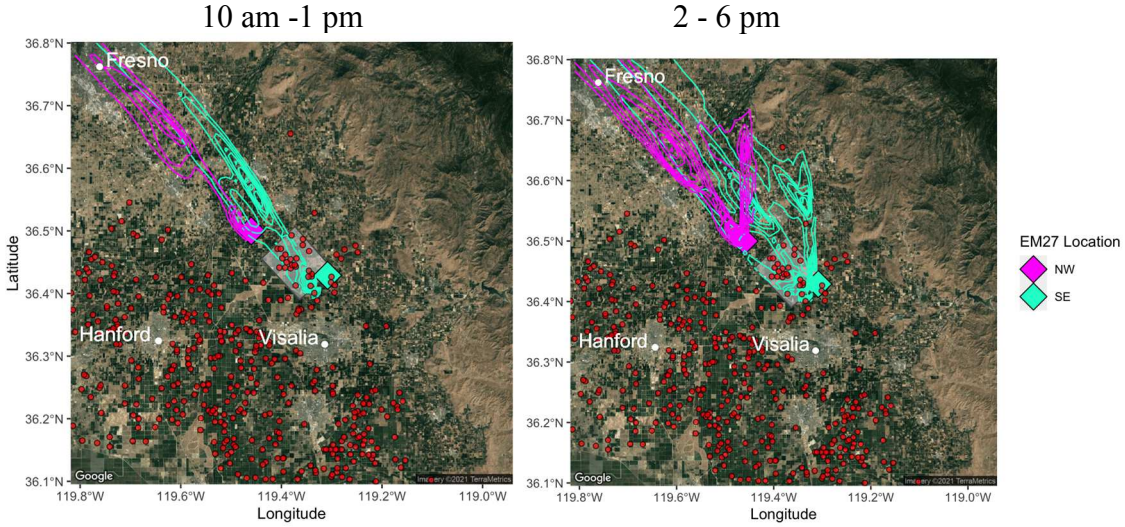

March 30th, 2019

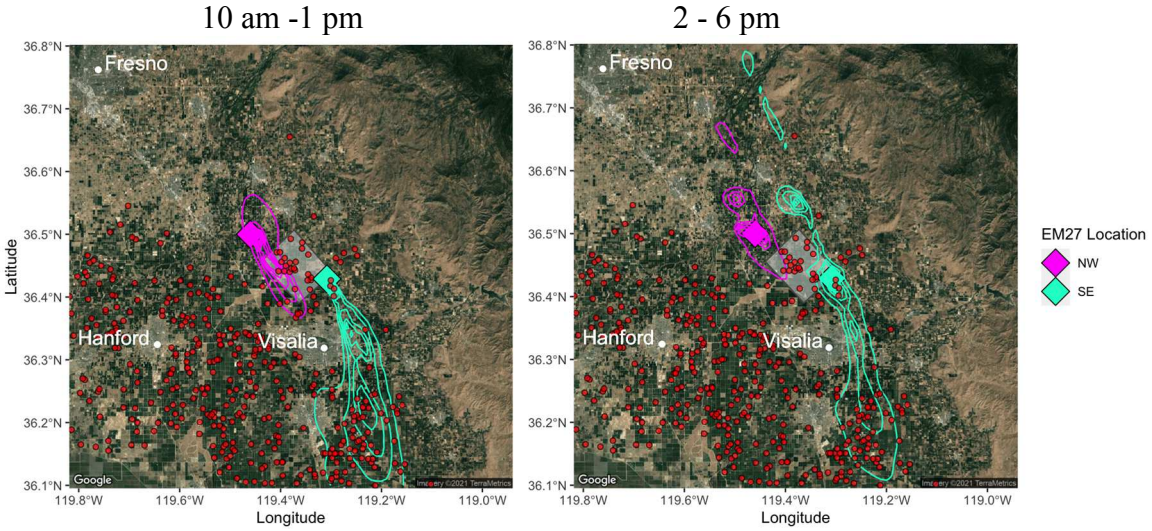

Figure A1.3 March 29th and 30th, 2019, WRF-STILT footprints as contour plots for 10-1 pm and 2-6 pm showing the Greater SJV dairy influence on March 30th. Winds were consistently NW on March 29th. Red circles are dairy farms.

Appendix A2: Appendix to Ground solar absorption observations of total column CO, CO_2, CH_4, and aerosol optical depth from California's Sequoia Lightning Complex Fire: Emission factors and modified combustion efficiency at large scales

A2.1 Text

A2.1.1 EM27/SUN Sensitivity

The EM27/SUN has different instrument sensitivities defined by the averaging kernels (AK) for each species measured shown below in Figure C1. The difference in sensitivity for the trace gases may introduce a bias in calculated ERs and MCE. Most of the difference is expected to be at the height of the plume where the smoke is concentrated at 4.1 km (~600 hPa). Following the methods of Hedelius et al. (2018), we divide the enhancements of ΔX_{CO2} and ΔX_{CO} by the averaging kernel at that smoke plume height:

$$MCE_{AK\ corrected}\ (SZA) = \frac{\Delta CO2/AK(SZA)_{CO2,600\ hPa}}{\Delta CO2/AK(SZA)_{CO2,600\ hPa} + \Delta CO/AK(SZA)_{CO,600\ hPa}}$$

(Eq. C1)

where $AK_{600\ hPa}$ is the averaging kernel sensitivity for CO or CO_2. The mean relative difference of the correction for the Sept. 12 plume event is -1.1%, thus not applying this correction would overestimate the MCE by 1.1%

Similarly for the ERs, we correct the enhancements prior to fitting the points with a linear regression for the Sept. 12 plume event:

$$ER_{X,AK\ corrected} = \frac{\Delta X/AK(SZA)_{X,600\ hPa}}{\Delta X_{CO2}/AK(SZA)_{X,600\ hPa}}$$

(Eq. C2)

Without applying this correction, E_{CH4} would be underestimated by 9.5% and E_{CO} by 14.2% due to the difference in sensitivity.

A2.1.2 Description of EM27/SUN measurements in the San Joaquin Valley during September 2018 and 2019

September 2018 and 2019 measurements in the San Joaquin Valley took place over 5 to 6 days in each year. Total column averages of CO, CO_2, and CH_4 were measured continuously between 9 am and 6 pm at northwest (NW) and southwest (SE) locations with the Los Alamos National Laboratory (LANL) and NASA Jet Propulsion Laboratory (NASA-JPL) EM27/SUNs. The NW and SE observational sites were chosen to target dairy farms in the area north of Visalia, CA. The NW location was consistent between measurement days, while the SE location varied per day dependent on forecasted winds to maximize sensitivity to dairies of interest (Figure A2.6).

A2.2 Tables

Table A Error! No text of specified style in document.**.1** Summary of correction factors from co-located EM27 measurements with TCCON at Caltech. The EM27/SUN was co-located with the CIT TCCON for 2-3 days before (Sept. 2 and 3, 2020) and after (Oct. 30, 31 and Nov. 31, 2020) the field measurements. A summary of the correction factors is shown in Table A1. An averaging kernel correction has been applied to the EM27/SUN observations prior to comparison following Hedelius et al. (2016). Due to a camera misalignment on Sept. 2 and 3, X_{CO} correction factors for those dates are not reported.

X_{gas}	Sept 2 & 3	Oct 30, 31 & Nov 1
X_{CH4}	0.9986 (0.0002)	0.9976 (0.0001)
X_{CO2}	1.0042 (0.0001)	1.0036 (0.0001)
X_{CO}	-	0.9737 (0.0028)
X_{H2O}	1.0044 (0.0005)	1.0101 (0.0005)

Table A Error! No text of specified style in document.**.2** Mean values of ln(Vo) from September 14, 19, and 24, 2020 used for deriving AOD.

Window	Mean ln(Vo)	sd	n
1020.9	15.17	0.11	3
1238.25	16.01	0.09	3
1558.25	16.34	0.08	3
1636	16.35	0.08	3

Table A Error! No text of specified style in document.**.3** Emissions of the top 20 of 2020 wildfires. Emission ratios for Sierra Nevada fires (Creek, Castle and North Complex) were derived from EFs compiled in this study. The rest of the ER are derived from literature (Prichard et al., 2020; Xu et al., 2022).

Fire Name	General Vegetation	Wildfire Area Burned (acres)	CO_2 (Tg)	ER_{CH4}	CH4 (Gg)
August Complex	Temperate evergreen	1,032,700	27.7	0.0055 ± 0.0044	55.4 ± 44.3
SCU Complex	Grasslands and savanna	396,399	4.6	0.0043 ± 0.0028	7.2 ± 4.7
Creek	**Temperate evergreen**	**379,882**	**13.8**	**0.0084 ± 0.0022**	**42.2 ± 11**
North Complex	Temperate evergreen	318,777	10.9	0.0084 ± 0.0022	33.3 ± 8.7
Hennessey	Shrublands	305,352	3.5	0.0033 ± 0.0021	4.2 ± 2.7
Castle	**Temperate evergreen**	**170,648**	**6.4**	**0.0084 ± 0.0022**	**19.5 ± 5.1**
Slater	Temperate evergreen	157,430	6.7	0.0055 ± 0.0044	13.4 ± 10.7
Red Salmon Complex	Temperate evergreen	143,836	4.6	0.0055 ± 0.0044	9.2 ± 7.4
Dolan	Shrublands	124,527	2.1	0.0033 ± 0.0021	2.5 ± 1.6
Bobcat	Shrublands	115,998	2.5	0.0033 ± 0.0021	3.0 ± 1.9
CZU Complex	Temperate evergreen	86,553	5.4	0.0055 ± 0.0044	10.8 ± 8.6
W-5 Cold Springs	Grasslands and savanna	84,817	0.7	0.0043 ± 0.0028	1.1 ± 0.7
Caldwell	Grasslands and savanna	81,224	0.4	0.0043 ± 0.0028	0.6 ± 0.4
Glass	Shrublands	67,484	1.9	0.0033 ± 0.0021	2.3 ± 1.4
Zogg	Shrublands	56,338	0.7	0.0033 ± 0.0021	0.8 ± 0.5
Wallbridge	Shrublands	55,209	4.1	0.0033 ± 0.0021	4.9 ± 3.1
River	Shrublands	50,214	0.9	0.0033 ± 0.0021	1.1 ± 0.7
Loyalton	Grasslands and savanna	46,721	0.7	0.0043 ± 0.0028	1.1 ± 0.7
Dome	Shrublands	44,211	0.1	0.0033 ± 0.0021	0.1 ± 0.1
Apple	Shrublands	33,209	0.8	0.0033 ± 0.0021	1.0 ± 0.6
Total					**213.7 ± 49.8**

A2.3 Figures

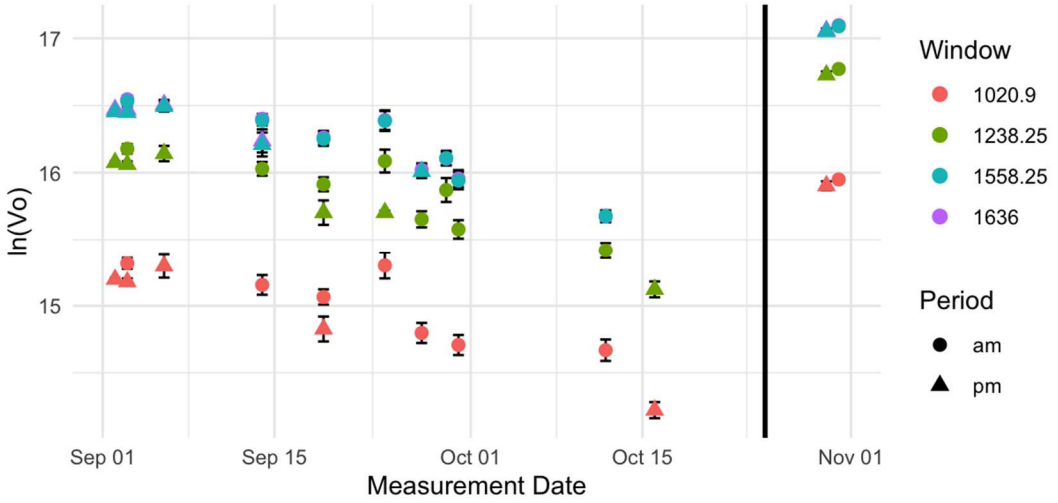

Figure A Error! No text of specified style in document.**.1** Absolute calibration for Langley exponential analysis of the EM27/SUN solar spectra over time from September to November 2020. Mirrors became significantly dirtier and dustier over the course of the measurement period. The ln(Vo) increased considerably after instrument mirrors were cleaned after the field campaign ended (black line).

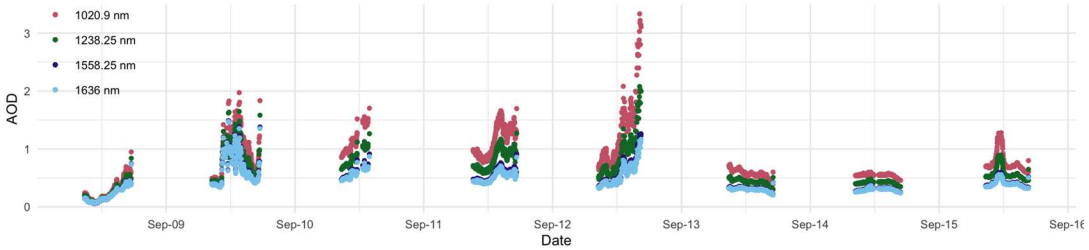

Figure A Error! No text of specified style in document.**.2** Timeseries of AOD for the four micro windows from September 8 to September 15, 2020.

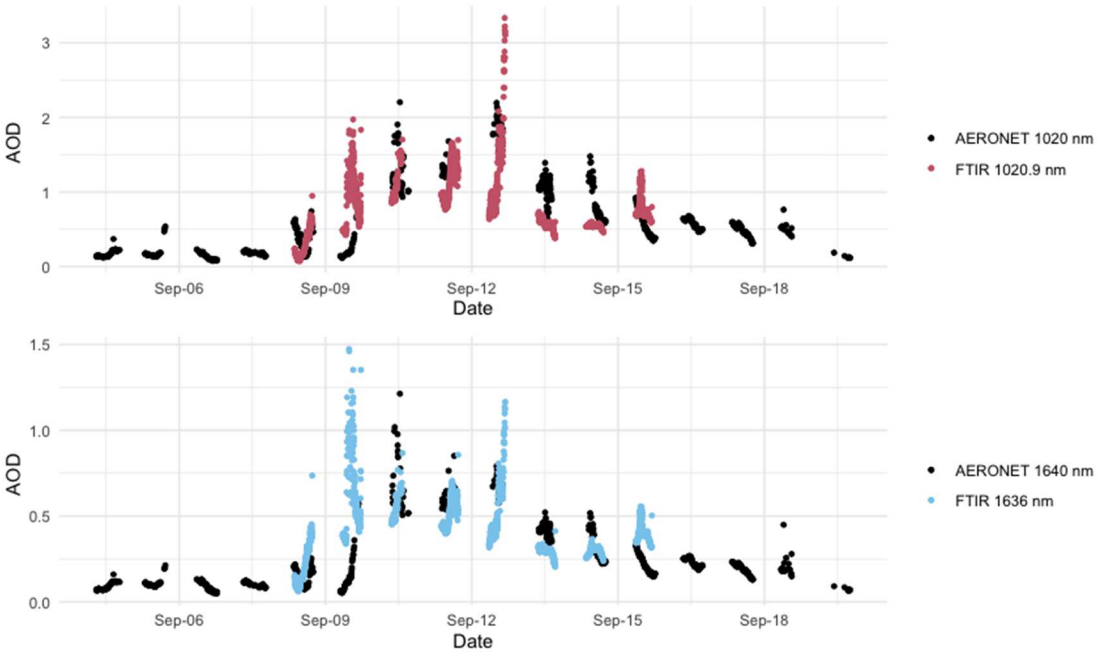

Figure A Error! No text of specified style in document.**.3** Timeseries of AOD from FTIR for the 1020.9 (red) and 1636 (blue) nm windows and AERONET (black) located in Fresno, CA ~90 km north of measurement site.

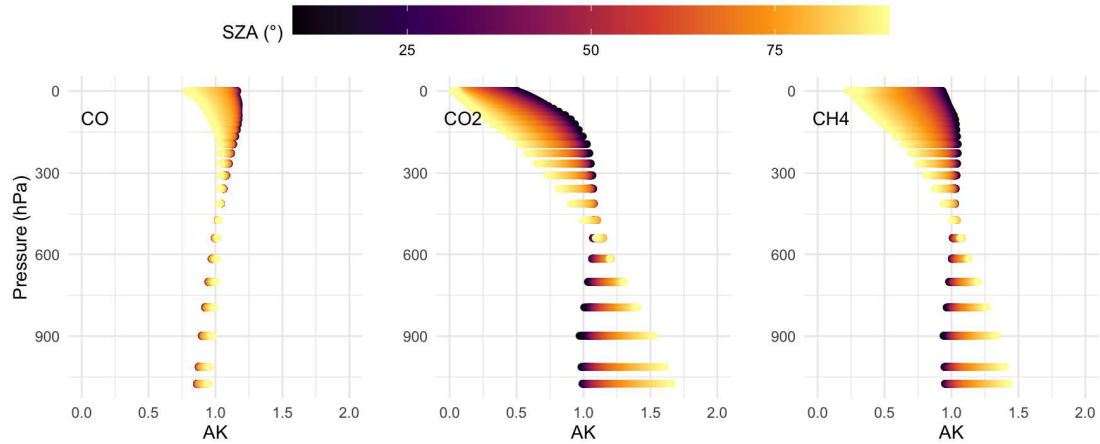

Figure A Error! No text of specified style in document.**.4** Averaging kernel (AK) of EM27/SUN of X_{CO} and X_{CO2} colored by solar zenith angle (SZA).

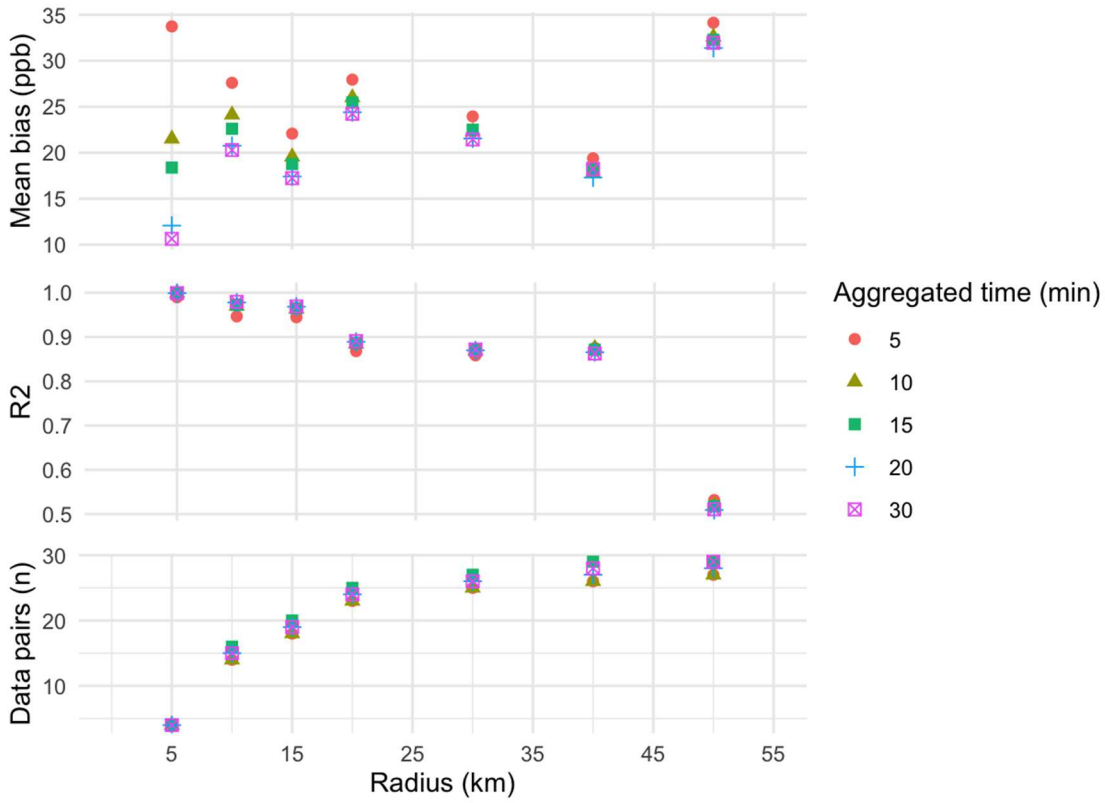

Figure A Error! No text of specified style in document.**.5** Results from sensitivity analysis with varying radius away from measurement site for selecting CO enhancements from TROPOMI pixels and varying aggregated times.

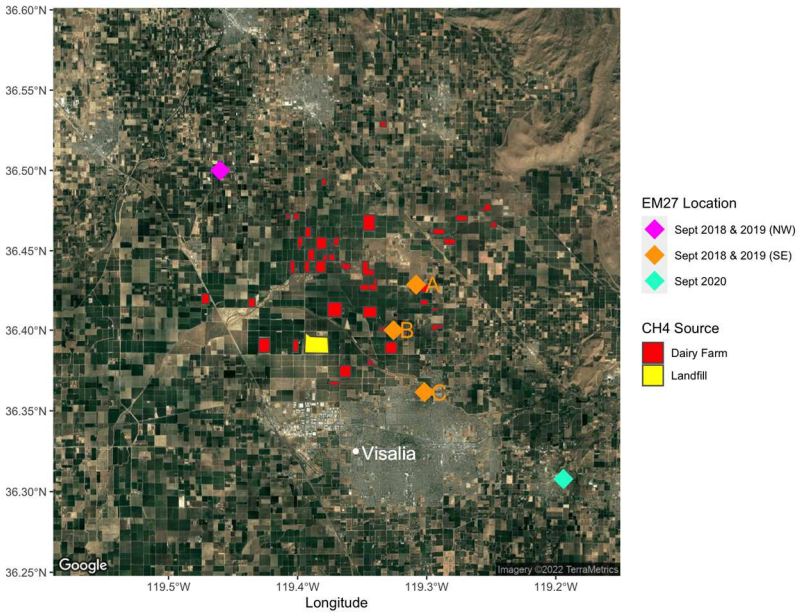

Figure A2.6. EM27/SUN observational sites at NW and SE and targeted dairy farms (red). Sources of methane in this area include dairy farms and a landfill.